ILLINOIS CENTER FOR TRANSPORTATION

Report No. FHWA-ICT-25-009

Evaluation of Unbonded Jointed Concrete Overlays

Jesús Castro Pérez
Richa Bhardwaj
Jeffery Roesler

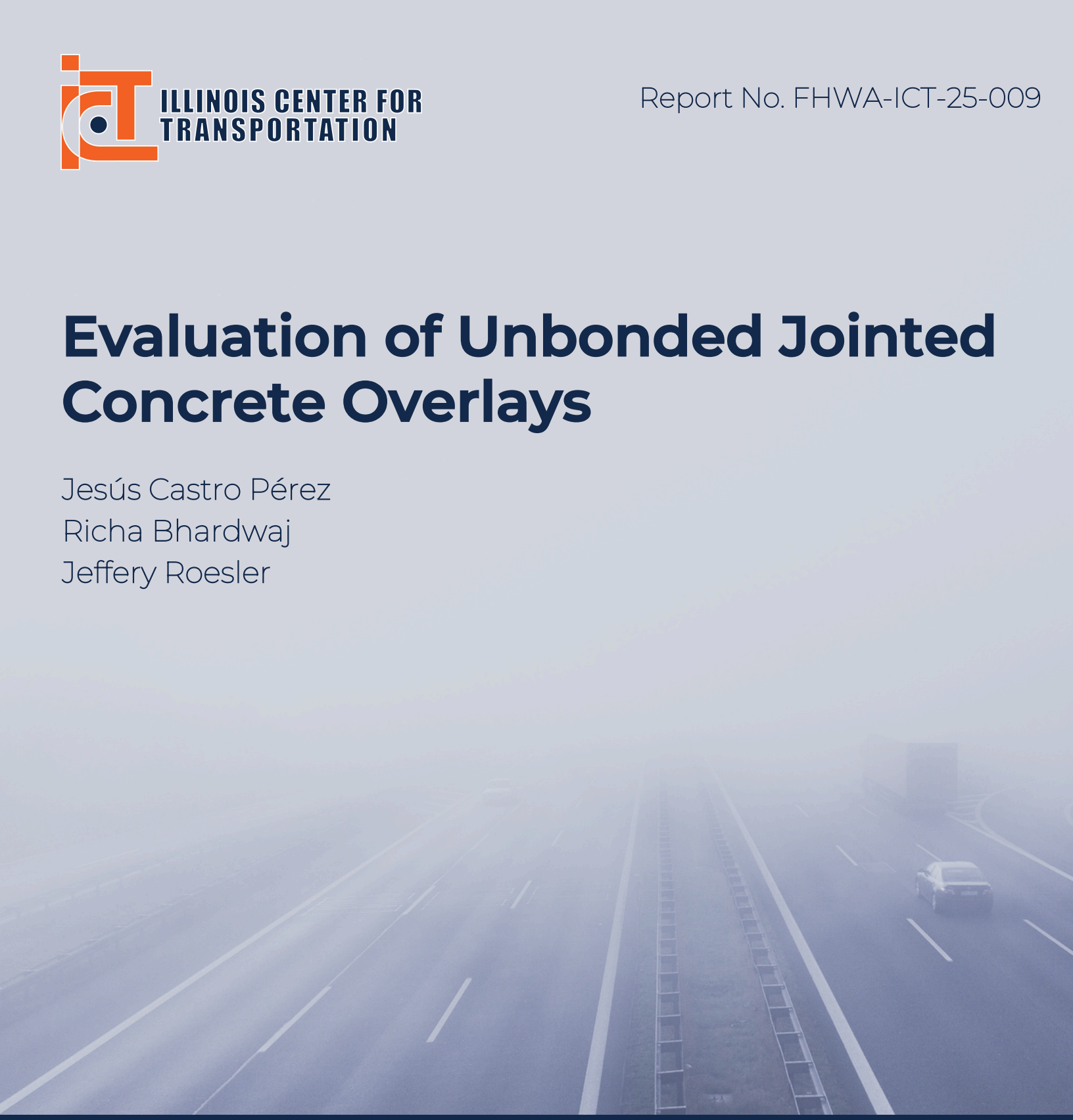

ICT Project R27-SP74

September 2025

ISSN: 0197-9191
ICT Series Report No. 25-009
https://doi.org/10.36501/0197-9191/25-009

TECHNICAL REPORT DOCUMENTATION PAGE

1. Report No.	2. Government Accession No.	3. Recipient's Catalog No.
FHWA-ICT-25-009	N/A	N/A

4. Title and Subtitle	5. Report Date
Evaluation of Unbonded Jointed Concrete Overlays	September 2025
	6. Performing Organization Code N/A

7. Authors	8. Performing Organization Report No.
Jesús Castro Pérez, Richa Bhardwaj, Jeffery Roesler (https://orcid.org/0000-0001-6194-269X)	ICT-25-009 UILU-2025-2009

9. Performing Organization Name and Address	10. Work Unit No.
Illinois Center for Transportation Department of Civil and Environmental Engineering University of Illinois Urbana-Champaign 205 North Mathews Avenue, MC-250 Urbana, IL 61801	N/A
	11. Contract or Grant No. R27-SP74

12. Sponsoring Agency Name and Address	13. Type of Report and Period Covered
Illinois Department of Transportation (SPR) Bureau of Research 126 East Ash Street Springfield, IL 62704	Final Report 11/16/24–9/30/25
	14. Sponsoring Agency Code

15. Supplementary Notes

Conducted in cooperation with the U.S. Department of Transportation, Federal Highway Administration.

https://doi.org/10.36501/0197-9191/25-009

16. Abstract

Concrete overlays for existing concrete and asphalt roads have been shown to be a viable rehabilitation or replacement option. This research project evaluated three unbonded concrete overlay (UBOL) projects in Illinois with high, medium, and very low truck volumes. The project's goal was to assess each overlay's performance including the influence of the interlayer. The project scope included distress surveys, evaluations of interlayer contact conditions through shear wave ultrasound tomography, assessments of structural response through falling weight deflectometer testing, profilometer testing, and core extractions. The findings from the UBOL performance study showed that nonwoven geotextile fabric (NWGF) can be an effective interlayer for concrete overlays under certain conditions. For thin UBOLs, even with macrofibers, steel tie bars should be used across the lane-shoulder joint to maintain shear transfer across a contraction joint or to limit construction joint opening. UBOLs with hot-mix asphalt (HMA) interlayers have historically provided good performance, which was seen in all three projects. For thinner UBOLs, slab geometry, interlayer type and transverse profile, and drainage must be considered in the overlay design. The I-72 eastbound section exhibited 3.8% longitudinal cracks (low severity) at transverse joints in the driving lane after 10 years, which has been linked to a combination of water in the joints, repeated truck loading, and debonding and low severity stripping of the HMA interlayer. For overlays with very few trucks (East Grand Road), the 6-inch slab and 11 feet by 12 feet slab size and the exclusion of dowel across transverse joints did not adversely impact UBOL performance.

17. Key Words	18. Distribution Statement
Concrete Overlay, Pavement, Fibers, Interlayer, Geotextile, Falling Weight Deflectometer, International Roughness Index, Nondestructive Testing, Performance	No restrictions. This document is available through the National Technical Information Service, Springfield, VA 22161.

19. Security Classif. (of this report)	20. Security Classif. (of this page)	21. No. of Pages	22. Price
Unclassified	Unclassified	67 + appendices	N/A

Form DOT F 1700.7 (8-72) **Reproduction of completed page authorized**

ACKNOWLEDGMENT, DISCLAIMER, MANUFACTURERS' NAMES

This publication is based on the results of **ICT-R27-SP74: Evaluation of Unbonded Jointed Concrete Overlays**. ICT-R27-SP74 was conducted in cooperation with the Illinois Center for Transportation; the Illinois Department of Transportation; and the U.S. Department of Transportation, Federal Highway Administration.

Members of the Technical Review Panel (TRP) were the following:

- Charles Wienrank, TRP Chair, Illinois Department of Transportation
- David Adedokun, Federal Highway Administration
- Greg Heckel, Illinois Department of Transportation
- Laura Heckel, Illinois Department of Transportation
- Marshall Metcalf, Illinois Department of Transportation
- Robert Rescot, Illinois Concrete Pavement Association
- John Senger, Illinois Department of Transportation
- Glenn Starke, Illinois Department of Transportation
- Charles Stein, TWM (Illinois Department of Transportation District 9 Consultant)
- Nathan Taylor, Illinois Department of Transportation

The authors also acknowledge Illinois Department of Transportation District 6 operations staff, drill crew, and lab employees for assisting in the findings of this report, including traffic control and coring operations.

EXECUTIVE SUMMARY

The use of concrete overlays as a rehabilitation or replacement option for existing concrete and asphalt roads has continued to expand. This research project evaluated three separate unbonded concrete overlay (UBOL) projects in Illinois with high, medium, and very low truck volume. The project's goal was to assess each overlay's performance including the influence of the interlayer. The project scope included distress surveys, evaluations of interlayer contact conditions through shear wave ultrasound tomography (MIRA), assessments of structural response through falling weight deflectometer (FWD) testing, profilometer testing, and core extractions.

The first project was a 6 in. UBOL on I-72 near Riverton, Illinois, with 6 ft × 6 ft panels with medium truck volume. A 100% distress survey, MIRA testing, FWD testing, and core analysis were completed on this section. The eastbound (EB) direction had a dense-graded hot-mix asphalt (HMA) interlayer system, while the westbound (WB) direction used a nonwoven geotextile fabric (NWGF) as the interlayer. The second project was a 6 in. UBOL on East Grand Road in Crainville, Illinois, with 11 ft by 12 ft slab panels, very few trucks per day, and an HMA interlayer. A 100% distress survey and MIRA testing were conducted at this project site. The third project was a jointed plain concrete pavement (JPCP) UBOL of 9.75 in. on I-57, near Anna, Illinois, with an HMA interlayer, 15 ft by 12 ft slab geometry, and heavy truck volume. A limited visual survey and MIRA testing were conducted on the I-57 UBOL section due to ongoing construction of another JPCP overlay section on I-57 northbound.

Overall, the experimental UBOL on I-72 is performing well with high probability of reaching its design life of 15 years. The I-72 EB section exhibited 3.8% longitudinal cracking in the wheel path of the driving lane slabs and approximately 0.25 in. of lane-shoulder joint faulting. In I-72 WB, corner spalling was the most common distress in 1.1% of the slab panels in the driving lane without any longitudinal cracking, but 0.25 in. of lane-shoulder joint faulting was also present. The HMA interlayer in the EB direction had a significantly lower IRI at 53 in./mi compared to 67 in./mi for the NWGF interlayer in the WB direction and a high driving lane IRI of 79 in./mi. The FWD results had lower average deflections and higher load transfer efficiency across all joint types in the EB direction relative to WB. The EB MIRA results suggested that an adhesive bond exists between the concrete overlay and HMA interlayer, while the HMA-CRCP (continuously reinforced concrete pavement) interface has a kissing bond (unbonded) at most test locations. In the WB direction, the NWGF is acting effectively as a UBOL separation layer between the overlay and CRCP. These interface conditions were confirmed with the extracted cores obtained in both directions. Additionally, the cores showed some deterioration in the HMA interlayer and bottom of the concrete overlay for areas where the joint was activated full depth, had sufficient joint width, and repeated loading. This mechanism led to significant HMA erosion/stripping at the lane-shoulder joint and subsequent faulting, whereas this condition at the transverse joints has led to HMA interlayer debonding and low severity erosion.

For East Grand Road, only 1.75% of the slab panels displayed a surface distress after nine years. The distresses were a combination of joint raveling and cracking from inadequate sawcut timing with some of the distresses reported within the first year after construction. The MIRA results suggested

that there were sections with adhesive bonding between the concrete overlay-HMA interlayer and others with just a kissing bond.

The 9.75 in. UBOL on I-57 did not show any notable surface distresses in the areas that were surveyed. The limited MIRA testing on I-57 showed no indication of HMA interlayer degradation.

The findings from the UBOL performance study have shown that NWGF can also be an effective interlayer solution under certain conditions for new concrete overlay designs. For thin UBOLs even with macrofibers, steel tie bars should be used across the lane-shoulder joint to maintain a tight contraction or construction joint opening that should limit differential deflection and reduction of load transfer efficiency (LTE) over time. UBOLs with HMA interlayers have historically provided good performance, which was seen in the three projects. For thinner UBOL, slab sizes and joint layout, interlayer transverse profile, and drainage issues must be considered in design to minimize the initiation of longitudinal cracks at the transverse joints or lane-shoulder joint faulting, as seen in the I-72 EB section. For the lower truck volume overlays, the larger slab geometry did not appear to impact the UBOL performance even without dowels in the transverse joints.

TABLE OF CONTENTS

LIST OF FIGURES

LIST OF TABLES

CHAPTER 1: INTRODUCTION

Unbonded concrete overlays (UBOLs) are viable options for existing concrete pavements that have reached the end of their service life. UBOLs consist of either a new conventional concrete (PCC) or fiber-reinforced concrete (FRC) layer separated from the existing concrete pavement by an interlayer, such as a dense-graded hot-mix asphalt (HMA) layer or a nonwoven geotextile fabric (NWGF). This separation layer prevents adhesive bonding between the two concrete layers and provides separation of the distressed existing pavement areas from the new concrete overlay. UBOLs have demonstrated good performance in many states (Fick et al., 2021). Over the years, IDOT has designed and constructed multiple UBOLs using jointed plain concrete pavement (JPCP) and continuously reinforced concrete pavements (CRCP) over existing JRCP or CRCP (DeSantis & Roesler, 2022a; Heckel & Wienrank, 2018; Sakulneya et al., 2024). More recently, UBOLs have experimented with thinner slabs and shorter panel sizes relative to traditional thicknesses and joint spacings (Khazanovich et al., 2020; Sen & Khazanovich, 2025).

As more UBOLs are constructed, more performance data become available that can assist in improving the existing design and materials specifications (Covarrubias et al., 2023; DeSantis & Roesler, 2022a). One premature distress that has been observed on a few UBOL projects with short joint spacings (Alland et al., 2016; Souder et al., 2020) is longitudinal cracking in the wheel path (Figure 1), as seen on I-72 eastbound near Riverton, Illinois (DeSantis & Roesler, 2022a). These cracks have developed in both the outside and inside wheel path of the driving lane and can initiate on both the leave and approach side of the transverse joint. Several researchers have proposed longitudinal distress originates in short panel sizes from damage to the HMA interlayer from a combination of repeated loading, localized stripping of asphalt, and/or permanent deformation of the HMA interlayer (Alland et al., 2016; DeSantis & Roesler, 2022a, 2022b). A previous study by DeSantis and Roesler (2022a) on I-72 hypothesized that premature longitudinal distress in the driving lane (Figure 1) was caused by repeated loading at the transverse joints and subsequent erosion/stripping of the asphalt interlayer from water present in the joint. There was additional evidence through coring at the lane-shoulder joint that stripping of the asphalt interlayer was occurring that was leading to lane-shoulder joint faulting but without crack development.

(A) 2020 (B) 2025

Figure 1. Photo. Longitudinal cracking in the wheel path of the driving lane on I-72 EB (left: August 5, 2020, right: February 25, 2025).

UNBONDED CONCRETE OVERLAY INTERLAYER TYPES

Different interlayer types for concrete overlays have advantages and limitations, but all interlayers must be durable and stable over time to meet the design life target. Several interlayers employed for UBOLs are dense-graded HMA, open-graded HMA, and NWGF. Dense-graded HMA has been the most common interlayer and is typically 1 to 2 in. thick. The HMA interlayer must be designed to avoid stripping in the presence of water and repeated loading. HMA layer stripping can lead to faulting at the transverse and longitudinal joints from erosion of the HMA interlayer and loss of stability. DeSantis and Roesler (2022b) showed the dense-graded HMA interlayer on I-72 EB passed the Hamburg wheel-tracking device standard but still has resulted in the development of longitudinal distress at the transverse joints in some locations (Figure 1).

Open-graded (or drainable) HMA is another asphalt interlayer option, which facilitates water conveyance between the existing and new concrete layer because of the permeability of the HMA interlayer. The open-graded HMA interlayer has similar thicknesses to the dense-graded HMA. A main concern for drainable interlayers is susceptibility of HMA to erosion/stripping and, subsequently loss in stability over time, leading to large deformations or collapse of the interlayer. Therefore, the drainable HMA interlayer needs to transmit water laterally out of the pavement structure and be stable over time to avoid premature cracking or faulting in the concrete overlay. IDOT's *Standard Specifications for Road and Bridge Construction Manual* (2022) documents the appropriate construction practices for HMA interlayers (e.g., mix parameters and design, field compaction levels, etc.).

NWGF interlayers are a semi-drainable interlayer solution. NWGF products come in different weight classifications that are related to fabric thickness, strength, and drainage capabilities. The interlayer selection of the NWGF weight can be chosen based on the existing pavement distress. A denser NWGF is recommended for more severely distressed pavements (Harrington & Fick, 2014). Additionally, different pigments are available to reduce solar absorption and heat storage in the NWGF prior to placing the concrete overlay. A white pigment option is available for higher temperature regions or during construction in high-temperature conditions. When placing the NWGF, a glue adhesive, tack coat, or nail and washer system is commonly used to secure it to the existing pavement. To maintain the permeability of the NWGF, the amount of adhesive or tack coat should not excessively impregnate the NWGF. Cement paste from the concrete overlay will also partially penetrate the surface of the NWGF and will likely impact the permeability of the NWGF depending on its weight. A 10-year experimental review of NWGFs for concrete overlays showed that NWGFs were erosion resistant (Cackler, 2017).

I-72 UBOL EXPERIMENTAL SECTION (RIVERTON, ILLINOIS)

The I-72 UBOL experimental section is in IDOT District 6, just east of Springfield, near Riverton, Illinois. This UBOL project is a 3.24-mile segment constructed in 2015 with two interlayer types: dense-graded HMA in the eastbound (EB) direction and NWGF in the westbound (WB) direction. The FRC overlay is 6 in. thick with 5 lb/yd^3 synthetic macrofibers and a 6 ft × 6 ft joint spacing.

The FRC overlay was paved over the top of two existing 12 ft lanes and the 10 ft outer shoulder and 6 ft inner shoulder. The driving lane and outer shoulder were paved in one stage, followed by the passing lane and inner shoulder. The original interstate was constructed in 1976 as an 8 in. continuously reinforced concrete pavements (CRCP) with bituminous shoulders. Prior to the 2015 UBOL placement, the existing HMA overlay, placed in 1998, was milled off. The inner shoulders were removed and replaced full depth to accommodate staged traffic, and the outside shoulders were partially removed and replaced. Minor repairs were also made to the CRCP surface in some areas. The 2015 concrete overlay did not contain dowel bars or joint sealant at transverse joints, and only the longitudinal construction joint at the roadway centerline included tie bars and hot-poured sealant.

The primary difference between the two directions is the interlayer, with the EB direction having a 1.25 in. (32 mm) dense-grade HMA interlayer, while the WB direction contains a 0.125 in. (3.2 mm) NWGF, as illustrated in Figure 2. The initial binder design for the HMA interlayer in the EB direction was PG 64-22; however, the fractionated reclaimed asphalt pavement (FRAP) asphalt binder replacement (ABR) exceeded 20%, which required the new binder grade to be lowered to a PG 58-28 (IDOT, 2025a, 2025c).

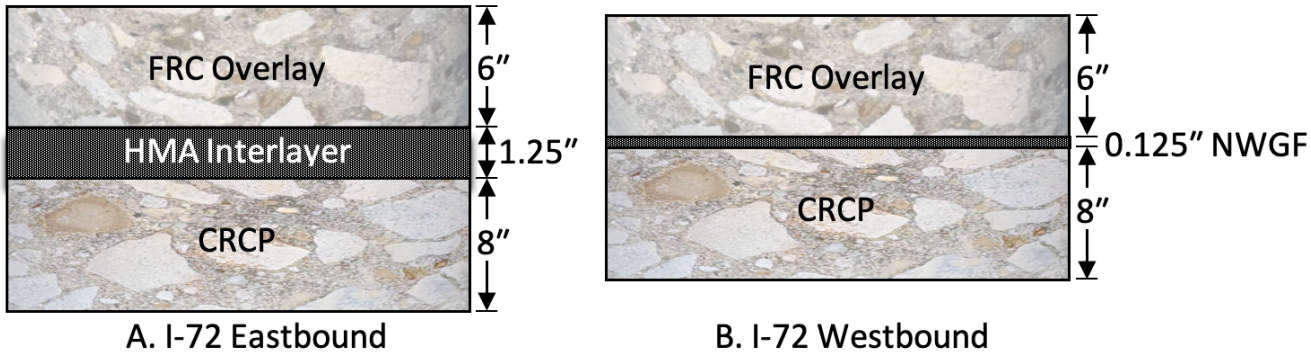

Figure 2. Illustration. Cross-section of the overlay on I-72 in the EB and WB directions.

As of 2023, the average annual daily traffic (AADT) volumes were 14,500 with 17.6% of multiple-unit (MU) and 2.8% single-unit (SU) trucks, as shown in Figure 3. The condition rating survey (CRS) or pavement condition trends for this section over the past 20 years are shown in Figure 4. Prior to the overlay placement in 2015, CRS scores had steadily declined, which triggered the rehabilitation with the experimental concrete overlay sections.

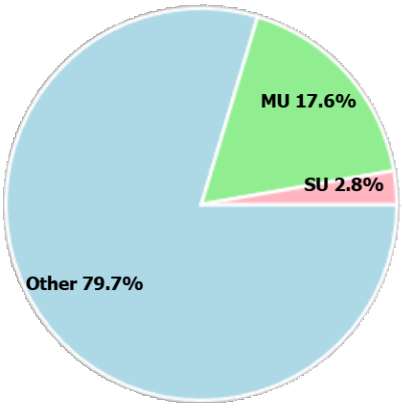

Figure 3. Chart. 2023 traffic distribution of multi-unit and single-unit trucks.

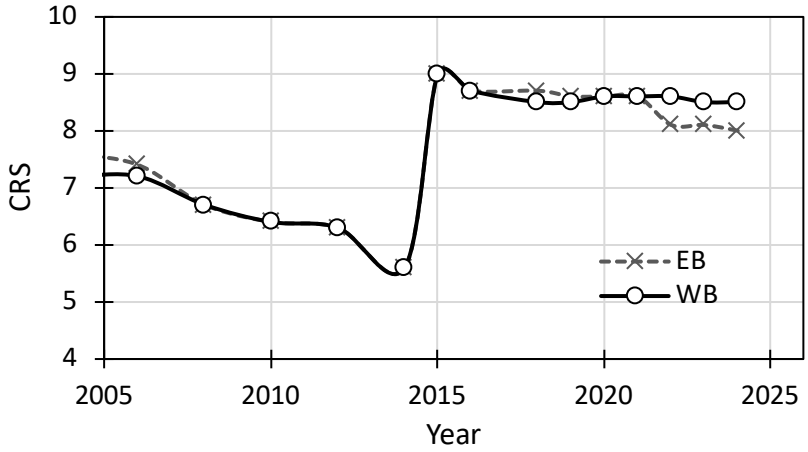

Figure 4. Graph. CRS for I-72 EB and WB from 2005 to 2025.

A detailed distress survey performed in August 2020 showed the predominant distress in the EB direction was low severity longitudinal cracking in the wheel path (inner and outer) of the driving lane. Moreover, distress surveys conducted as early as 2016 showed signs of this same longitudinal distress just starting to develop from a limited number of transverse joints. The observed longitudinal cracking had not occurred in the WB lanes (NWGF) based on the last survey by DeSantis and Roesler (2022a). However, their survey noted faulting was observed across the longitudinal lane-shoulder joint (between the driving lane and the shoulder) in both directions. One important objective of this study was to document the development of distresses in this I-72 experimental concrete overlay since the 2020 observations.

EAST GRAND ROAD EXPERIMENTAL SECTION (CRAINVILLE, ILLINOIS)

The East Grand Road concrete overlay section is located in IDOT District 9 in the city of Crainville, between Hafer Road and Hurricane Road, with a total project length of 2,745 ft. The existing pavement structure was a 6 in. JPCP overlaid with 4 in. to 6 in. of HMA layer. In 2020, an unbonded JPCP overlay was constructed with a 6 in. concrete surface layer in two lanes, each with 11 ft wide

slabs and 12 ft sawed transverse joints (see Figure 5). The overlay also included widening and a tied curb and gutter with #5 tie bars at 30 in. centers and 9 in. embedment. The project was originally designed as an HMA overlay but was changed to PCC at no additional cost after a value engineering proposal. According to 2021 traffic data, the AADT was 3,250 without MU truck percentage reported, but mostly limited to school buses and garbage trucks. A full distress survey of this concrete overlay section was another objective of this study, which had not been previously completed.

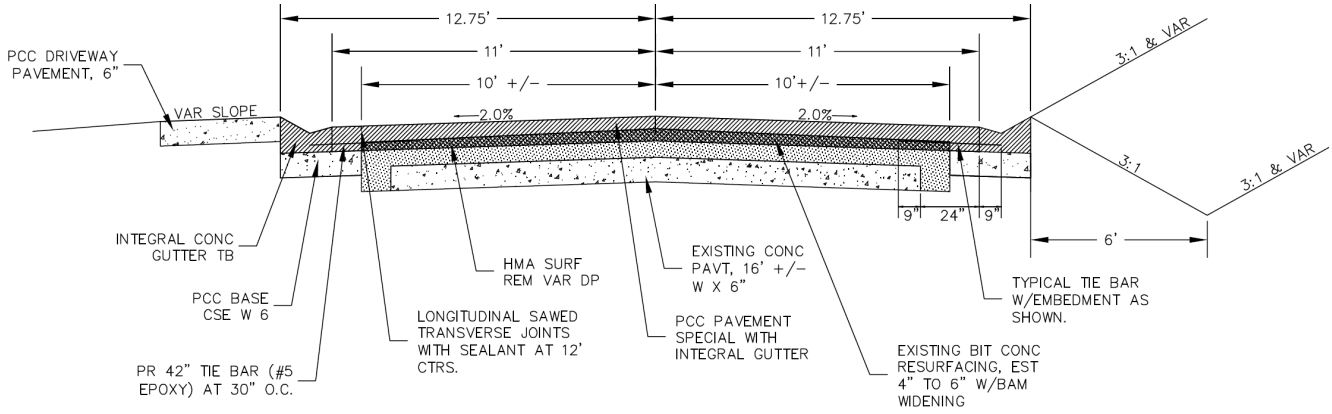

Figure 5. Illustration. Typical JPCP overlay section for East Grand Road in Crainville, Illinois.

I-57 EXPERIMENTAL SECTION (ANNA, ILLINOIS)

The I-57 concrete overlay section is in IDOT District 9 near Anna, Illinois. The original pavement structure, constructed in 1960–61, consisted of a 10 in. JRCP. In 2016, this section was rehabilitated with a 9.75 in. unbonded JPCP overlay with a 3.25 in. HMA interlayer. The existing HMA overlay was partially milled to a depth of 1.25 in. and replaced with new HMA. The overlay was constructed like a new JPCP with 15 ft joint spacing and dowel bars placed by insertion. Figure 6 summarizes the 2023 traffic composition for this section near Anna with AADT of 13,200 including 7,700 MU and 425 SU truck traffic for a total of 8,125 heavy commercial vehicles (HCV). This corresponds to 61.6% truck traffic in this corridor. The CRS trend for this section is shown in Figure 7. Prior to the overlay (in 2016), CRS values were below 5. After the JPCP overlay, the CRS rose to approximately 8.5 and is currently 8.3.

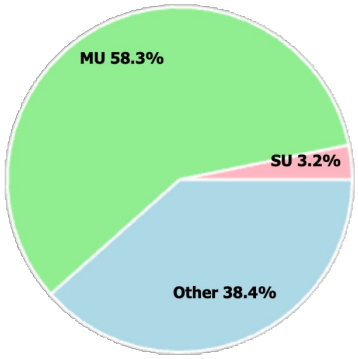

Figure 6. Chart. 2023 traffic distribution of multiple-unit (MU), single-unit trucks (SU), and other vehicles on I-57 near Anna, Illinois.

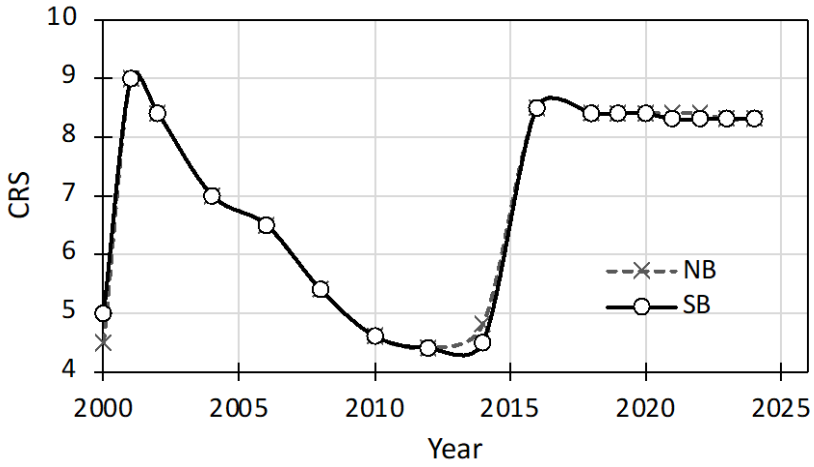

Figure 7. Graph. CRS history from 2000 to 2024 for the I-57 overlay section near Anna, Illinois.

In 2024, IRI values were measured at 79 in./mi in the northbound direction and 85 in./mi in the southbound direction. Faulting was not reported in the 2024 assessment (IDOT, 2025b). However, a faulting of 0.03 in. (0.76 mm) in both directions was reported in 2023. Table 1 summarizes the road condition (IRI and faulting) for this section over the past decade.

Table 1. IRI and Faulting Data from IROADS in I-57 Section Before and After (2016) Concrete Overlay

Year	IRI NB	IRI SB	Faulting NB	Faulting SB
2024	79	85	–	–
2023	74	78	0.03	0.03
2022	72	75	0.02	0.03
2021	72	77	0.02	0.03
2020	73	77	0.02	0.02
2019	77	80	0.02	0.02
2018	71	79	0.02	0.02
2016	72	76	–	–
2014	130	113	N/A	N/A

CHAPTER 2: RESEARCH OBJECTIVES AND SCOPE

The objectives of this project are to conduct field evaluations of current distress, structural and functional performance, and interlayer condition of three UBOL projects in Illinois. The purpose of the field evaluations is to determine the current overlay performance in Illinois, investigate potential mechanisms of interlayer-related distress, and generate recommendations for future improvements to UBOL design and construction practices for Illinois applications. These goals will be met through visual distress surveys, falling weight deflectometer (FWD) testing, shear wave tomography scans, and high-speed profilometer measurements as well as field core extraction. The detailed scope of work for each project section is summarized next.

1. **I-72 UBOL section near Riverton, Illinois (District 6)**: The following will be evaluated for this 6 in. FRC overlay with a small panel size and two distinct interlayer systems (dense-graded HMA in the EB and NWGF in the WB):
    - 100% visual distress survey to document existing surface distresses, particularly cracking, spalling, and faulting.
    - Interface contact condition between the slab and interlayer using ultrasound tomography and shear wave reflection method.
    - Structural response testing using FWD.
    - Profile measurements for the international roughness index (IRI).
    - Pavement core sampling to investigate longitudinal cracking and interlayer condition as well as potential degradation mechanisms (e.g., erosion, debonding, and stripping).
2. **East Grand Road UBOL section in Crainville, Illinois (District 9)**: The following will be evaluated for this 6 in. JPCP overlay with 11 ft wide by 12 ft long slabs on an existing HMA layer over an existing concrete pavement:
    - 100% visual survey to document existing distresses.
    - Interface contact between the slab and interlayer using shear wave method.
3. **I-57 UBOL section near Anna, Illinois (District 9)**: The following will be evaluated for this 9.75 in. (248 mm) JPCP overlay on a 3.25 in. HMA interlayer on an existing 10 in. JRCP:
    - Visual survey with existing video van data from IROADS.
    - Site visit with limited visual survey.
    - Periodic shear wave tomography testing (MIRA device) to evaluate the interface contact condition between the slab and HMA interlayer system.

CHAPTER 3: REVIEW OF RECENT PERFORMANCE STUDIES OF CONCRETE OVERLAYS

Although UBOLs have performed very well in many states over the past 40 years (Fick et al., 2021; Harrington et al., 2007), the use of smaller panels for UBOLs with an interlayer is a relatively new concept. The primary failure mode reported for these short slabs has been longitudinal cracking in the wheel path (Alland et al., 2016; Khazanovich et al., 2020; Souder et al., 2020), which has been investigated in previous studies by the principal investigator (DeSantis & Roesler, 2022a, 2024). The initiation and development of this type of structural cracking is still being understood, but the previous study (DeSantis & Roesler, 2022a) hypothesized that the cracks developed as bottom-up and initiate as a result of interlayer erosion and loss of interlayer stability, as seen in Figure 8.

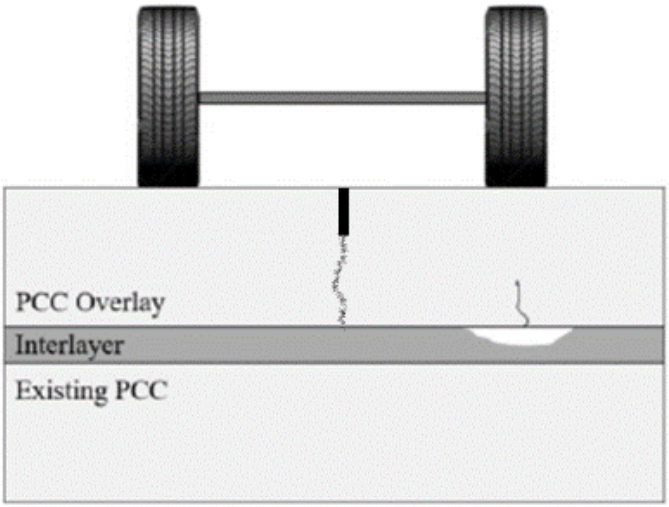

Figure 8. Illustration. Erosion or shearing of HMA interlayer leading to bottom-up longitudinal cracking.

Source: Souder et al. (2020)

LITERATURE REVIEW

Crack Initiation and Mechanisms

Other studies have observed that longitudinal cracking initiates at the transverse joint and propagates from localized damage within the HMA interlayer from repeated loading and concurrently stripping, erosion, and/or consolidation (Alland et al., 2016; Khazanovich et al., 2020). This repeated load damage can result in a localized void in the interlayer system in the wheel path, which increases the deformations and results in higher tensile stresses at the bottom of the concrete slabs. This leads to bottom-up cracking if the flexural strength of the concrete is exceeded. Bonded concrete overlays on asphalt (BCOA) with 6 × 6 ft panels experience a similar distress mechanism as the interfacial bond deteriorates and longitudinal cracking initiates at the transverse joint (Li & Vandenbossche, 2013). This cracking mechanism is less likely to occur when a NWGT interlayer is used as the interlayer unless the concrete layer approaches its fatigue life (DeSantis & Roesler, 2022a).

Performance of Concrete Overlay Projects

DeSantis and Roesler (2022a, 2022b) conducted an extensive review on the performance of short-jointed UBOLs across various regions with their respective environmental and traffic conditions, including several U.S. states, Canada (Ontario), and Uruguay. Their investigation collected overlay performance data directly from state DOTs and from reviewing existing tools like Google Earth, Maps, and the American Concrete Pavement Association Overlay Explorer webtool. They primarily examined overlays with thicknesses up to 6 in. (152 mm), most of which were constructed without dowels. Dense-graded HMA interlayers were common in most evaluated sections, while the overlays in Michigan and Missouri employed NWGF interlayers. DeSantis and Roesler (2022a, 2022b) particularly looked to identify similarities in longitudinal cracking patterns to those observed in the experimental sections on I-72, which had an HMA and NWGF interlayer in the EB and WB directions, respectively.

Findings by DeSantis and Roesler (2022a, 2022b) indicated that longitudinal cracking was not consistent on all evaluated sections, but when present, the cracking could be attributed to mechanisms such as repeated loading (fatigue), localized stripping, or erosion and interlayer consolidation in the case of HMA interlayers. Additionally, overlays extending wider than existing support pavements had higher likelihoods of longitudinal reflective cracking. For thinner overlays (less than 4 in. or 102 mm), observed cracking was more likely because of fatigue rather than interlayer deterioration. Table 2 and Table 3 show a summary of the relevant technical details of each analyzed section.

Table 2. Concrete Overlays Examined from Google Earth & Maps (after DeSantis & Roesler, 2022a)

State / Province	Section ID	Location	Year Constructed	Joint Spacing, ft	Overlay Thickness, in.	Longitudinal Cracking Present (Yes/No)
Colorado	I-70	Grand Junction	2012	6 × 6	6	Yes
	SH 121 (Wadsworth Blvd)	Denver	2001	6 × 6	6	Yes
	SH 13	Craig	2016	6 × 6	6	No
Iowa	IA 3	Plymouth Co. to east of Cleghorn	2015	6 × 5.5	6	Yes
	US 65	Wayne Co. Line to US 34	2013	5	5.5	No
	US 18	Fredericksburg	2011	4.5 × 4.5	4.5	Yes
	IA 13	Strawberry Point	2008	4.5 × 4.5	3.5–4.5	Yes
	IA 9	Oche Edan	2015	5 × 5	5.5	Yes
	IA 14	Parkersburg	2013	5 × 5	4.5	Yes
	IA 175	Arthur	2013	7 × 7	4.5	Yes
Kansas	I-70	Wilson	2012	6 × 6	6	No
Michigan	South Boulevard E.	Pontiac	2009	6 × 6	4	Yes
	Hall Road	Woodhaven	2008	6 × 6	4	Yes
	Gratiot Avenue	Detroit Metro Area	2004–2005	6 × 6	4	No
	Little Mack Av	St Clair Shores	2011	6 × 6	4	Yes
Minnesota	TH 53	Duluth	2008	6 × 6	5	Yes
Missouri	Route D	Kansas City	2008	6 × 6	5	No
	Route 24 / Business 63 Intersection	Moberly	2010	6 × 6	5.5	Yes
Ohio	Sprague Road	North Royalton	2014	6.5 × 6.5	7	No
Oklahoma	US 69 N	Kiowa	2007	6 × 6	5	Yes
Ontario	Bloor St W. at Aukland Rd	Toronto	2003	5 × 5	6	No
Pennsylvania	SR-50	Bridgeville	2016	6 × 6	6	No
Uruguay	Ruta 24	Guyunusa	2011–2012	6 × 6	5.5	No
Wyoming	US 30	Cokeville	2012	6 × 6	6	Yes

Table 3. Additional Information on Concrete Overlays Examined from Google Earth & Maps (after DeSantis & Roesler, 2022a)

State / Province	Section ID	Structure Type	Interlayer Type	Interlayer thickness, in.
Colorado	I-70	BCOA	Existing HMA	Unknown
	SH 121 (Wadsworth Blvd)	BCOA	Existing HMA	Unknown
	SH 13	BCOA	Existing HMA	Unknown
Iowa	IA 3	UBOL	Dense HMA	1.5
	US 65	UBOL	Dense HMA	1
	US 18	UBOL	Milled Dense HMA	5–8
	IA 13	UBOL	Milled Dense HMA	3
	IA 9	UBOL	Milled Dense HMA	3
	IA 14	UBOL	New Dense HMA	1
	IA 175	UBOL	Milled Dense HMA	3.5
Kansas	I-70	BCOA	Existing HMA	14
Michigan	South Boulevard E.	UBOL	Dense HMA	1
	Hall Road	UBOL	Dense HMA	1
	Gratiot Avenue	UBOL	Dense (NB) / Open HMA (SB)	1–2
	Little Mack Av	UBOL	NWGF	NA
Minnesota	TH 53	UBOL	Dense HMA	1
Missouri	Route D	UBOL	NWGF	16.2 oz
	Route 24 / Business 63 Intersection	UBOL	NWGF	NA
Ohio	Sprague Road	UBOL	Dense HMA	1
Oklahoma	US 69 N	UBOL	Dense HMA	1
Ontario	Bloor St W. at Aukland Rd	UBOL	Dense HMA	1
Pennsylvania	SR-50	UBOL	Dense HMA	1
Uruguay	Ruta 24	BCOA	Existing HMA	10
Wyoming	US 30	BCOA	Existing HMA	3+

Erosion Potential and Stabilized Layers

Caicedo and Caro (2023) experimentally investigated the erosion susceptibility of base materials under rigid pavements, highlighting erosion as a significant contributor to pavement deterioration. Similarly, DeSantis and Roesler (2024) employed the Hamburg wheel-tracking device to assess the erosion potential of asphalt- and cement-stabilized support layers, establishing recommended erosion depth thresholds for both types of stabilization based on expected traffic conditions. This type of testing is likely helpful in assessing the performance of interlayers for UBOLs and/or an existing HMA layer that will receive a concrete overlay.

Overlay Performance and Design Practices

Hanson (2023) reviewed decades of concrete overlay performance in Iowa's primary highway system, identifying the best practices associated with long-term success. Overlays that are 4 in. or thicker with sealed joints and no widening performed best, with several test sections remaining in good condition nearly 30 years after construction. The use of matching overlay widths with existing pavement reduced edge stress and cracking, especially when shoulders were left untied.

King and Akakin (2023) analyzed nine concrete overlays constructed on full-depth reclamation (FDR) bases. Concrete overlays on stabilized (FDR) bases performed reliably (minimal faulting and adequate LTE) across various climates and traffic levels under specific thickness, slab sizes, and separation interlayer systems. Longitudinal cracking was documented in some projects, often extending across multiple slabs; however, most of these cracks were sealed with no observations of significant spalling or faulting.

King and Taylor (2023) conducted a survival analysis of concrete overlays in Iowa. They found that concrete overlays have 30 years of service life with an 85% probability of survival (before rehabilitation) and more specifically, a median of 23 to 27 years for exceeding the target performance limits (i.e., Pavement Condition Index [PCI] < 60 and IRI > 170 in./mi) for low-volume roads with concrete on concrete unbonded overlays (COC-U). Service life was more often limited by PCI deterioration than increased roughness (IRI).

Bonded Overlay Performance and Design

Pierce et al. (2022) summarized performance data from 19 bonded concrete overlay projects on asphalt (BCOAs), resulting in performance prediction curves. The best-performing overlays had 6 ft × 6 ft slabs with thicknesses between 5 and 6 in. and were placed on asphalt with minimal surface preparation. Their findings emphasized that slab size and overlay thickness were key performance indicators, while the inclusion of fibers and joint sealing had negligible effects. Intersections were more faulted and rougher than non-intersection areas. Moreover, total cracking did not show significant differences in intersections and non-intersection areas.

UBOL Critical Stress Prediction, Design, and Construction

Khazanovich et al. (2020) introduced a mechanistic-empirical design guide for UBOLs that specifically addresses longitudinal cracking, accommodating both short (6 ft or 1.8 m) and conventional slab sizes (> 12 ft) as well as various interlayer types (e.g., asphalt and geotextile). Building upon this framework, Khazanovich et al. (2023) recently refined these procedures, providing an improved method for calculating critical transverse stresses in UBOLs, which considers potential interlayer erosion damage and void formation. The design method can be found at the following link: https://pavements.pitt.edu/Products/UNOL.aspx.

Sheffield et al. (2023) surveyed concrete paving contractors to identify barriers to concrete overlay implementation, revealing critical factors such as lack of project bidding opportunities, concerns over traffic control, and the availability of skilled construction personnel. Their insights indicated potential areas of opportunity to increase the adoption of concrete overlays by addressing industry-specific concerns.

CHAPTER 4: FIELD DISTRESS SURVEY

Distress surveys were conducted for two out of three project sites (I-72 and East Grand Road). A complete walking survey was conducted on I-72 EB/WB, which is approximately 3 miles in one direction, to determine if there are more distresses developing that are not easily seen by IROADS or driving in a vehicle. The East Grand Road UBOL section in Crainville also received a 100% walking survey. The I-57 UBOL section was not walked because of the volume of traffic and counterflow traffic in the southbound lanes from ongoing construction work on the northbound lanes.

I-72 EB AND WB

A detailed distress survey was conducted on April 16, 2025, from station 0+00 to 171+00 and 171+00 to 0+00 (EB and WB directions), to quantify the distresses that developed since the last surveys in May 2021. The station 0+00 was located near the I-72 exit in Riverton, Illinois. The distresses were classified and quantified for the full section survey; however, the detailed distress survey (i.e., distress mapping) focused on three sample units in each direction. The three sample units consisted of 1,000 ft long segments located near the start, middle, and end of the UBOL section. For the EB direction, these segments were at stations 10+00 to 20+00, 74+15 to 84+15, and 142+50 to 152+50, and for the WB direction stations 152+50 to 142+50, 112+50 to 102+50, and 20+00 to 10+00. These same segments were surveyed by DeSantis and Roesler in 2020 and Heckel and Wienrank in 2016, which would be used for comparison to the 2025 distress survey results.

I-72 EB

In the I-72 EB section with the HMA interlayer, the most common distress was longitudinal cracking in the wheel path initiating at the transverse joints. In the three 1,000 ft long sections, longitudinal cracks were observed in 7.0% of the driving lane slab panels. In a survey reported by DeSantis and Roesler (2022a), for the same three 1,000 ft long segments, 6.3% of the driving lane panels presented longitudinal cracks. Therefore, the percentage of slab panels in the driving lane with longitudinal cracks increased only slightly (from 6.3% to 7.0%) for the same segments over a five-year period. The number of longitudinal cracks from 2020 and 2025 for the 100% survey of the EB is summarized in Table 4. Among the three 1,000 ft sections surveyed in detail, the highest concentration of longitudinal cracks was observed in between stations 10+00 and 20+00 with 12.6% (i.e., percentage of slab panels with a longitudinal crack in the driving lane only), and the lowest between stations 74+15 and 84+15 with 1.5% slabs cracked. Moreover, in the entire EB section in 2025, the number of longitudinally cracked slabs was 3.8% of the driving lane.

Table 4. Longitudinal Cracks and Slab Cracking Percentage in 2020 and 2025 in the EB Driving Lane

Long. Cracks per Year (% Panels)	0+00–10+00	10+00–20+00	20+00–74+15	74+15–84+15	84+15–142+50	142+50–152+50	152+50–171+00
2025	2 (0.60)	42 (12.6)	85 (4.7)	5 (1.5)	55 (2.8)	23 (6.9)	5 (8.9)
2020	N/A	38 (11.4)	N/A	4 (1.2)	N/A	18 (5.4)	N/A

Other distress types like transverse cracks, corner breaks, corner spalling, joint spalling/raveling, and patch distresses were observed on I-72 EB, as shown in Table 5. The number of distresses other than longitudinal cracks are not as significant on the I-72 EB section. A higher amount of spalling and transverse cracks occurred near the start and end of the UBOL EB section, which can mostly be associated with the transition from the overlay to an HMA pavement section. The only distresses observed in the passing lane were a few longitudinal cracks in the EB direction.

Table 5. Type and Quantity of Distress for I-72 EB Driving Lane in 2025

Distress Type	0+00–10+00	10+00–20+00	20+00–74+15	74+15–84+15	84+15–142+50	142+50–152+50	152+50–~171+00
Long. Crack	2	42	85	5	55	23	5
Trans. Crack	3	0	1	0	0	0	6
Corner Breaks	1	0	0	0	2	0	0
Corner Spall	9	4	1	0	8	0	1
Others[1]	2	0	0	1	5	1	1

[1] Others include joint spalling/raveling and distressed patches.

The identification of longitudinal cracks was facilitated through the presence of moisture inside the crack. As seen in Figure 9-a, longitudinal cracks are observed in the wheel path emanating from the transverse joint. The length of longitudinal cracks typically varied from 2 ft to 4 ft from both approach and leave slabs. Only three corner breaks (see Figure 9-b) were observed in the I-72 EB section. The width of longitudinal cracks varied typically between just 0.01 in. to 0.05 in. (see example in Figure 9-c), likely due to the presence of synthetic macrofibers in the concrete mixture. Most longitudinal cracks present on both sides of the transverse joint are not continuous across the joint but have an offset between 2 in. and 6 in., as seen in Figure 9-d. Cracks do not tend to propagate for the entire slab length thus far.

Distress surveys conducted in 2016 by IDOT, and in 2020 by DeSantis and Roesler, indicated that partial length longitudinal cracks were present in I-72 EB just one year after construction. The initial hypothesis that the longitudinal cracks were a result of reflective cracking from the CRCP has been dismissed by DeSantis and Roesler in 2022. In addition to the distresses summarized in Table 5, longitudinal faulting across the lane-shoulder joint continues throughout the EB direction with varying magnitudes. The shoulder elevation was on average measured at 0.25 in. (6 mm) higher than the driving lane, as seen in Figure 10. The working hypothesis is water drainage out of the driving lane transverse joints might be partially blocked at the lane-shoulder joint, which may lead to pumping and erosion of the asphalt interlayer. This has been further confirmed with observations from the cores extracted at the lane-shoulder joint. The complete field survey map, including the station, distribution, and classification of distresses in sections 10+00 to 20+00, 74+15 to 84+15, and 142+50 to 152+50, can be found in Appendix A.

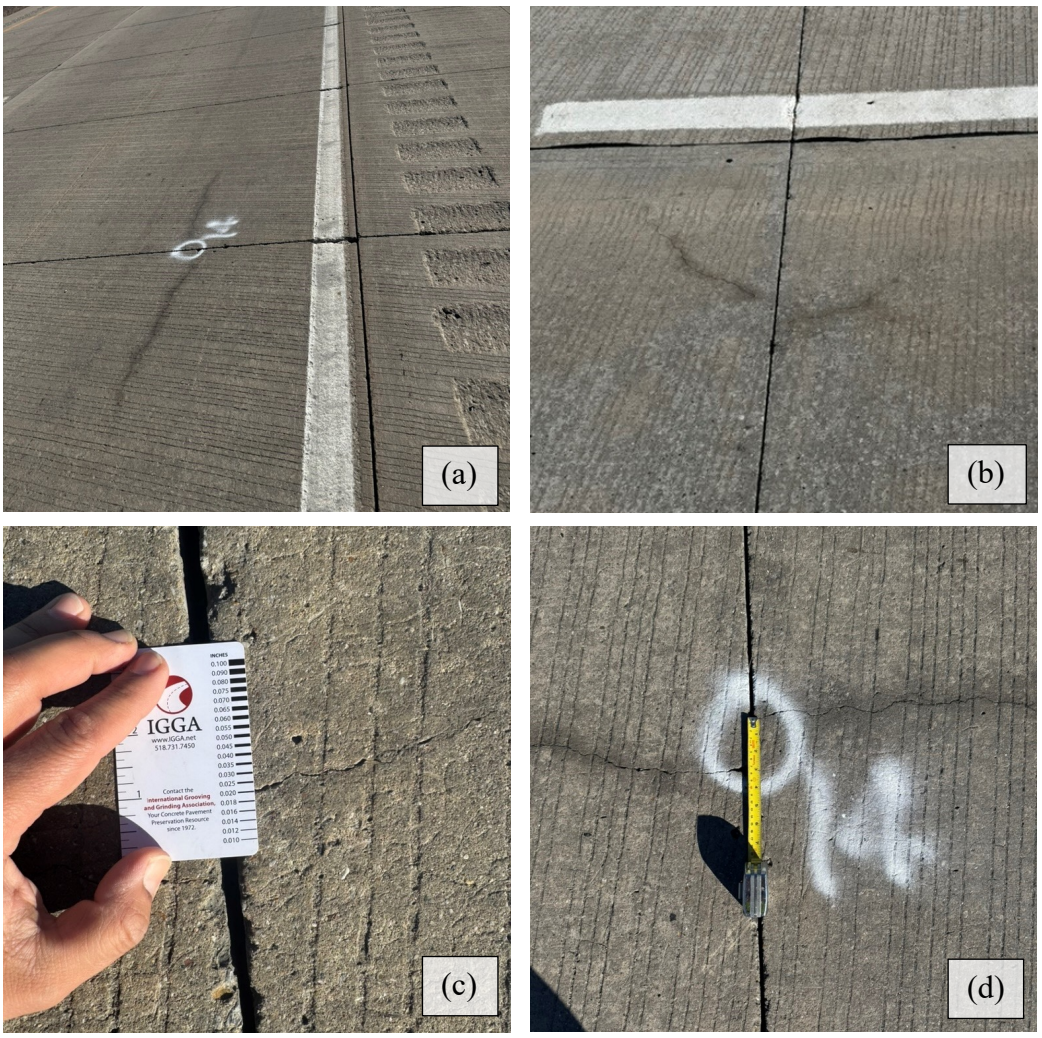

Figure 9. Photo. Types of distresses in driving lane: (a) longitudinal cracks in wheel paths, (b) corner break, (c) typical longitudinal crack width measurement, and (d) discontinuity of longitudinal cracks across a transverse joint.

Figure 10. Photo. Example of faulting along driving lane-shoulder joint of 0.25 in. (6 mm) on I-72 EB.

I-72 WB

The I-72 WB section had a significantly lower amount of cracking distresses than I-72 EB. In particular, the I-72 WB section did not show any of the longitudinal cracks observed in the EB one, and the predominant distress was a characteristic corner spall, specifically between stations 102+50 and 20+00. A summary of the distress survey from I-72 WB is shown in Table 6. Transverse cracks were observed near the start of the section where IRI was reported high. The only distresses observed in the WB passing lane were a few corner spalls.

Table 6. Distress Count by Type of Distress in I-72 WB

Distress Type	171+00–152+50	152+50–142+50	142+50–112+50	112+50–102+50	102+50–20+00	20+00–10+00	10+00–0+00
Long. Crack	0	0	0	0	0	0	0
Trans. Crack	5	0	0	0	0	0	2
Corner Breaks	0	0	0	1	3	0	0
Corner Spall	0	5	4	6	37	8	4
Others[1]	4	1	0	2	3	2	0

[1] Others include joint spalling/raveling and distressed patches.

The increase in distresses for the three 1,000 ft long segments over the past five years was minimal, with only four additional corner spalls, one corner crack, and one section with excessive raveling. For these three segments, the maximum distress increase was corner spalls in the driving lane from 1.1% in 2020 to 1.9% in 2025, as observed in Table 7. In 2025, the amount of slab panels with corner spall in the I-72 WB driving lane was 1.1%. For all the distress types, only 1.5% of the panels displayed some type of distress after 10 years.

Table 7. Driving Lane Corner Spalls in 2020 and 2025 for I-72 WB

Spalls per year (% panels)	171+00–152+50	152+50–142+50	142+50–112+50	112+50–102+50	102+50–20+00	20+00–10+00	10+00–0+00
2025	0 (0)	5 (1.5)	4 (0.4)	6 (1.8)	37 (1.3)	8 (2.4)	4 (1.2)
2020	N/A	3 (0.90)	N/A	4 (1.20)	N/A	8 (2.4)	N/A

Figure 11-a displays the typical corner spall observed in I-72 WB, and Figure 11-b shows one transverse crack that propagated across the slab panel. Corner spalls were observed in both lanes, but principally in the driving lane. The higher concentration of spalls in the corner at the transverse joint seems to be related to insufficient sawcut depth and full width of the panel. Transverse cracks were observed near the start and the end of the UBOL sections, which were adjacent to the transition to another pavement type (i.e., UBOL to HMA or HMA to UBOL). Faulting along the driving lane-shoulder joint on I-72 WB, as seen in Figure 12, had similar characteristics to the faulting observed in the I-72 EB section. The WB shoulder elevation at the joint was also about 0.25 in. (6 mm) above the driving lane edge, resulting in the measured faulting in Figure 12. The fact that a similar faulting in the lane-shoulder joint is occurring for two sections with different interlayer systems might reinforce the hypothesis that water movement and erosion mechanisms might be pushing the shoulder up with

either asphalt interlayer or debris entering the joints. This will be later discussed with observations from the extracted cores. The complete field survey map, including the station, distribution, and classification of distresses in segments 152+50 to 142+50, 112+50 to 102+50, and 20+00 to 10+00, are documented in Appendix A.

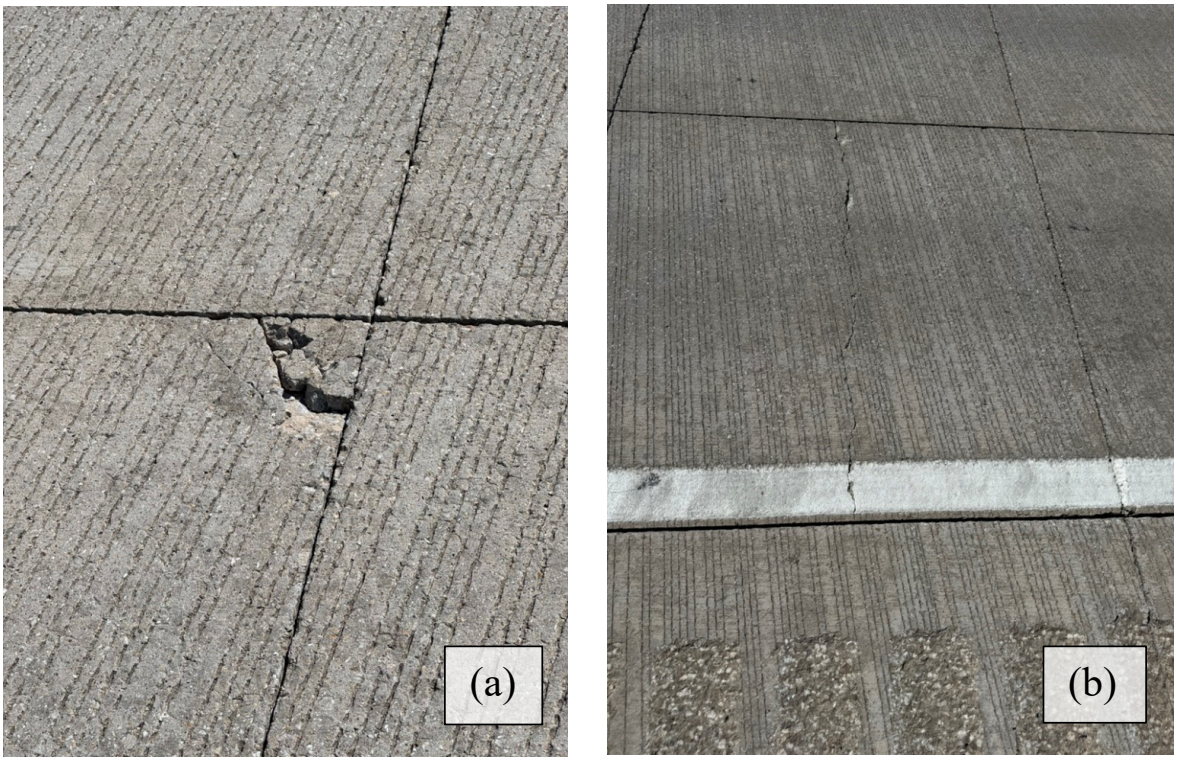

Figure 11. Photo. (a) Typical corner spall in I-72 WB and (b) transverse crack across full-width panel.

Figure 12. Photo. Faulting along driving lane-shoulder joint at approximately 0.25 in. (6 mm) on I-72 WB.

EAST GRAND ROAD, CRAINVILLE, ILLINOIS

A full walking survey was conducted on East Grand Road (Crainville, Illinois) on February 24, 2025. As seen in Figure 13, the UBOL section is 2,745 ft long and has 11 × 12 ft panel sizes. No previous 100% distress survey had been completed on this section. A total of eight distresses were observed on the full section survey, which consisted mostly of corner cracks (Figure 14-a) and cracks parallel to transverse joints (Figure 14-b). The cracks in Figure 14-a and Figure 14-b are likely because of insufficient sawcut notch depth or sawcutting the joint too late. Engineers from District 9 stated some of these distresses had appeared within a year after construction. Figure 14-c shows transverse joint raveling from sawcutting too early. Based on the observed cracks, approximately 1.75% of the concrete overlay panels have a crack after nine years. A detailed crack mapping of this UBOL section can be found in Appendix A.

Figure 13. Photo. Street view of UBOL section on East Grand Road (Crainville, Illinois).

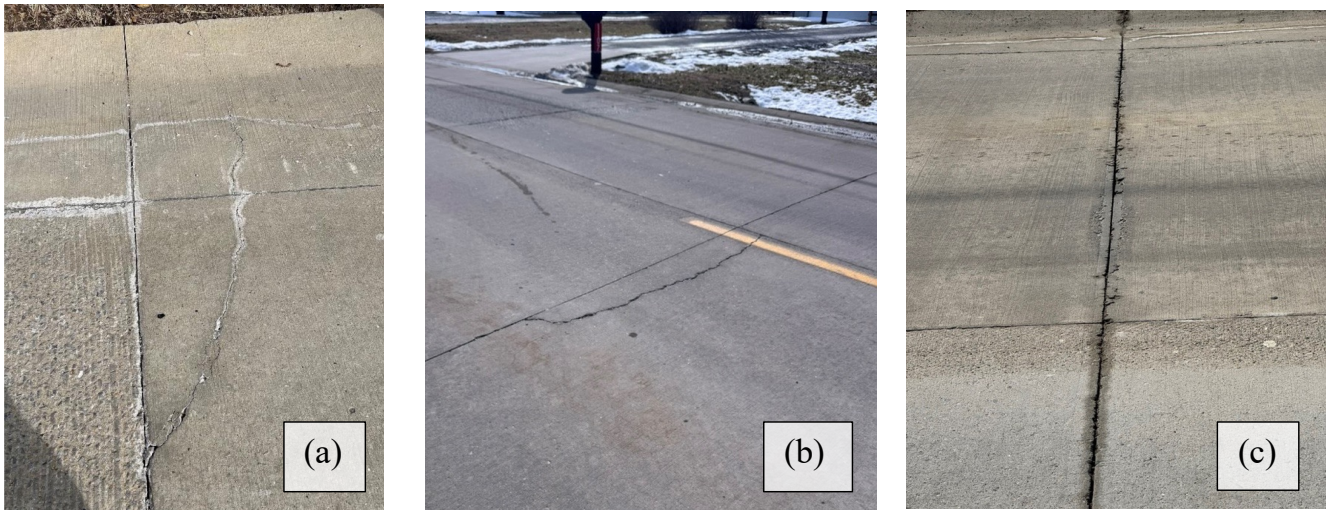

Figure 14. Photo. Types of distresses observed on East Grand Road: (a) corner cracks, (b) transverse crack parallel to transverse joint, and (c) raveling on transverse joint.

I-57 NEAR ANNA, ILLINOIS

A pavement distress assessment survey was conducted along a segment of northbound I-57 between stations 27+150 and 28+660 on February 24, 2025. Due to limited traffic control measures and active, high-volume traffic, a full walking survey was not performed. Observations were limited to visual inspection from the shoulder in randomly selected areas. No significant distresses were observed other than minor localized transverse joint raveling/spalling, as seen in Figure 15.

Figure 15. Photo. Transverse joint spalling/raveling in I-57 northbound between stations 27+150 and 28+660.

For the southbound JPCP overlay section that was under a counterflow traffic pattern, the distresses shown in Figure 16 (i.e., cracking and spalling near the transverse joint) were reported by an IDOT engineer, Ben Wills. However, the distress development appeared to be a result of the traffic phasing.

Figure 16. Photo. Distresses observed on I-57 southbound lane during head-to-head traffic phasing.

Source: Photos by Ben Wills (2025)

CHAPTER 5: NONDESTRUCTIVE TESTING AND CORING

Nondestructive testing (NDT) was performed to assess the structural, functional, and layer performance with FWD, profilometer, and shear wave (MIRA) testing, while coring was done on I-72 to determine the condition of the UBOL interlayers. FWD, profilometer, and MIRA testing with coring was only completed for the I-72 sections. In the Crainville section, only MIRA testing was completed. On the I-57 overlay, only periodic MIRA measurements were conducted between stations 27+150 and 28+660 in the northbound direction.

FALLING WEIGHT DEFLECTOMETER

I-72 EB and WB

FWD testing was completed on both I-72 EB and WB on October 15–16, 2024. The testing locations included the center of the slab (CS), slab corner (CN), middle of the transverse leave joint (TJ), and mid-slab position of the longitudinal lane-shoulder joint (LJ) in the outer slab panels of the driving lane. The FWD testing was divided into intensive and non-intensive areas, with the intensive portion loading the first 15 panels at all positions and the remaining panels being tested every 100 ft. Intensive testing was done in three segments in each direction, as seen in the gray areas in Figure 17. For non-intensive testing (white areas in Figure 17), panels were tested every 500 ft in each direction.

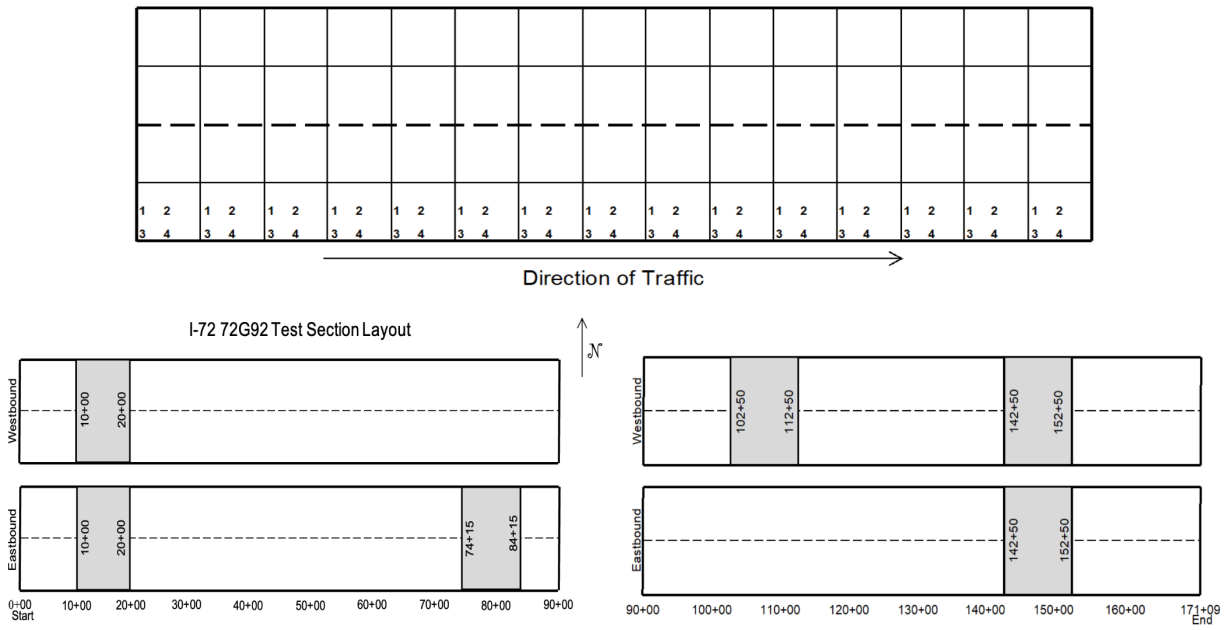

Figure 17. Illustration. FWD testing layout for intensive (gray areas) and non-intensive (white areas). Drop pattern for 15 panel intensive area drops are shown in the top schematic.

The first FWD test for this experimental concrete overlay was done in October 2016, which was followed up by intensive and non-intensive FWD tests in August 2020. The average air and surface temperatures for the different years are given in Table 8, with 2020 testing conducted at the highest air temperatures and the most recent FWD tests (2024) at the lowest air temperatures. Past FWD results have shown the WB direction with the NWGF interlayer having higher deflections than the HMA interlayer in the EB concrete overlay. This is somewhat unexpected since longitudinal cracking in the wheel paths was observed in the EB section and has been linked to localized erosion and stripping of the HMA interlayer. Both directions have longitudinal contraction joint faulting along the lane shoulder joints, with the concrete shoulder being at a higher elevation relative to the outer driving lane panels (DeSantis & Roesler, 2022a).

Table 8. Temperature Levels at Time of FWD Testing

	Oct. 2016	Aug. 2020	Oct. 2024
Average Air Temperature	67°F	85°F	54°F
Average Pavement Surface Temperature	68°F (at start only)	74°F	50°F
Average Pavement Temperature at 3" depth	70°F (at start only)	72°F	57°F

The 9 kip normalized deflections for the center slab drops have increased for both EB and WB directions with time, with the EB deflections showing a greater increase (47.5%) from 2016 to 2020 compared to later years from 2020 to 2024 (see Table 9). In the WB direction, deflections increased at a steadier rate (14% every four years). The normalized deflections in the WB section with the geotextile interlayer have been consistently higher than the EB section with an HMA interlayer. The coefficient of variation (COV) for the normalized deflections remained similar for the two directions. The elevated EB deflections observed in 2020 may be a result of the higher pavement temperatures during FWD testing, which can impact the behavior of the HMA interlayer.

Table 9. Normalized Deflections at Center Slab (2016, 2020, and 2024)

Center Slab (CS) Normalized 9 kip Deflection (mils)						
	EB: 2016	WB: 2016	EB: 2020	WB: 2020	EB: 2024	WB: 2024
Average	2.40	3.93	3.54	4.48	3.85	5.11
Std Dev.	0.28	0.48	0.58	0.53	0.55	0.77
COV	12%	12%	16%	12%	14%	15%
4-yr Change	n/a	n/a	47.5%	14.0%	8.8%	14.1%

Figure 18 and Figure 19 present the normalized center deflections for various stations in the EB and WB directions, respectively, for the years 2016, 2020, and 2024. Over the span of eight years, normalized deflections increased significantly in both the EB and WB directions, with average increases of 1.45 mil (60%) and 1.18 mil (30%), respectively.

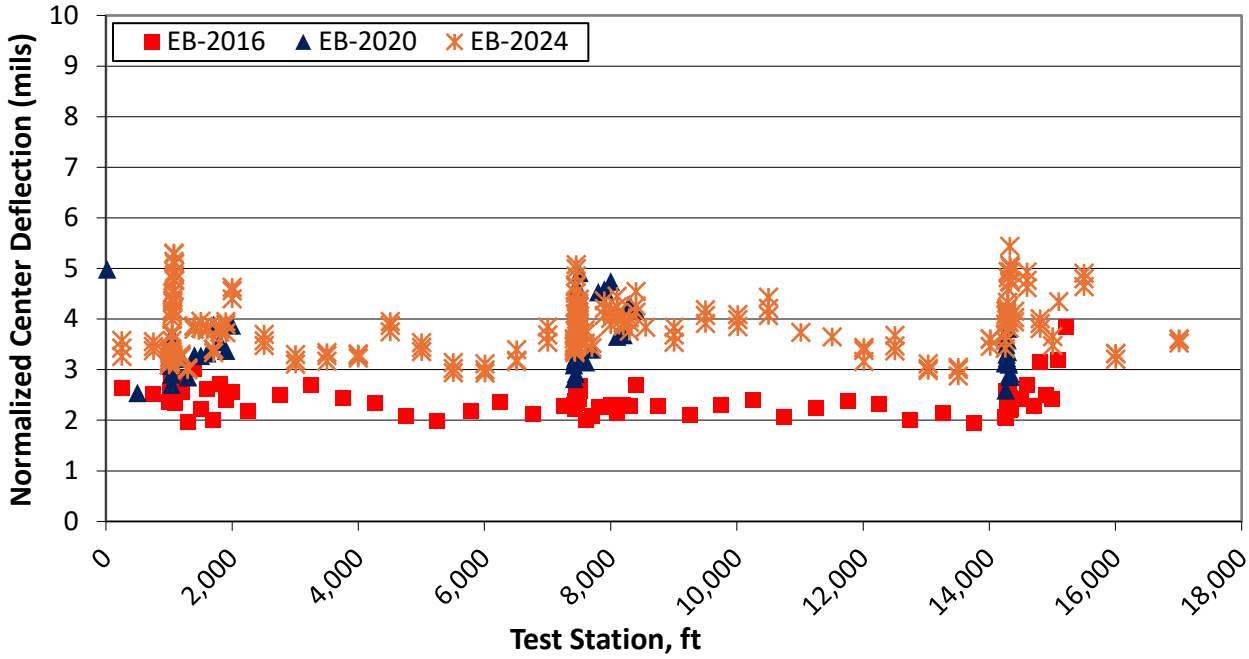

Figure 18. Graph. EB center slab normalized deflections in 2016, 2020, and 2024.

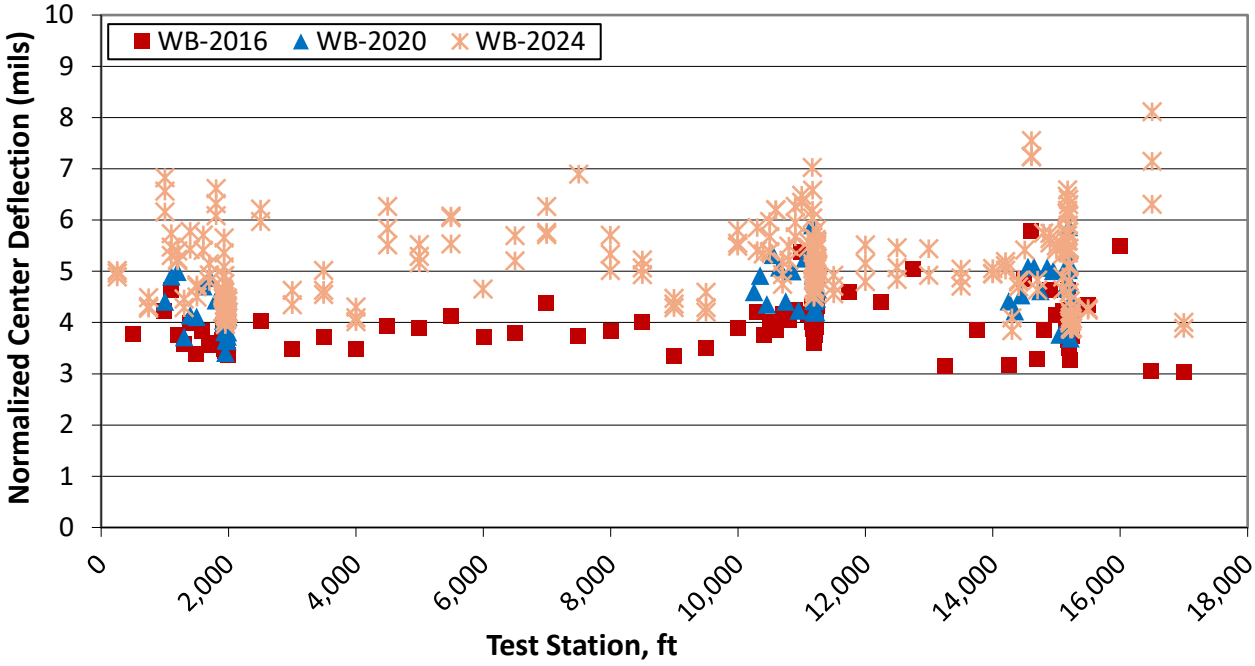

Figure 19. Graph. WB center slab normalized deflections in 2016, 2020, and 2024.

For the transverse leave joint, normalized deflection increased by 74% (1.87 mils) in the EB direction and 65% (3.18 mils) in the WB direction over the eight-year period (Table 10). Similarly, the load transfer efficiency (LTE) across the transverse leave joint dropped by 6.7% for the EB direction and a more substantial 26% for the WB direction (Table 11) over eight years.

Table 10. Normalized Deflections of Transverse Leave Joints (2016, 2020, and 2024)

Transverse Joint (TJ) Leave Edge Normalized 9 kip Deflection						
	EB: 2016	**WB: 2016**	**EB: 2020**	**WB: 2020**	**EB: 2024**	**WB: 2024**
Average	2.52	4.88	3.54	5.63	4.39	8.06
Std Dev.	0.44	1.27	0.62	1.38	1.36	1.88
COV	18%	26%	18%	25%	31%	23%
4-yr change	N/A	N/A	40.5%	15.4%	24.0%	43.2%

Table 11. Load Transfer Efficiency across Transverse Leave Joints (2016, 2020, and 2024)

Transverse Joint (TJ) Leave Edge Load Transfer Efficiency (LTE)						
	EB: 2016	**WB: 2016**	**EB: 2020**	**WB: 2020**	**EB: 2024**	**WB: 2024**
Average	90%	78%	88%	74%	84%	58%
Std Dev.	6%	14%	6%	15%	14%	11%
COV	6%	18%	7%	20%	17%	19%
4-yr change	N/A	N/A	−2.2%	−5.1%	−4.5%	−21.6%

The higher reduction of joint LTE in the WB direction can be connected to a combination of the compressibility of the NWGF layer, unbonded interface of the interlayer, and lower temperatures at testing. Figures 20–23 show the normalized deflections and LTEs of transverse leave joints in both directions. The intensive FWD testing section shows the expected variability in the pavement response for 15 consecutive slabs. It was originally hypothesized that the distribution of the intensive testing responses (e.g., normalized deflections) would be like the distribution of the responses in the periodic testing throughout the entire test section. This was not necessarily true in all years and response parameters (see Figure 18, 2024 EB tests) but was true, for example, for normalized deflections for WB tests in 2024 (Figure 19).

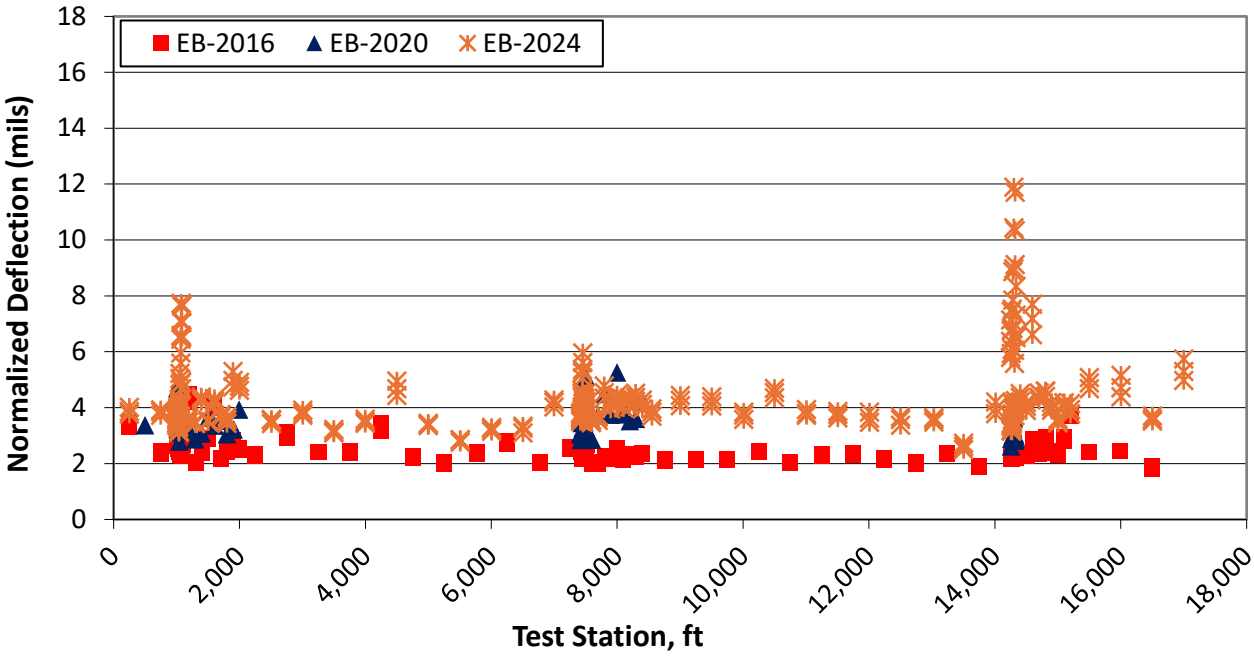

Figure 20. Graph. EB transverse leave joint normalized deflection in 2016, 2020, and 2024.

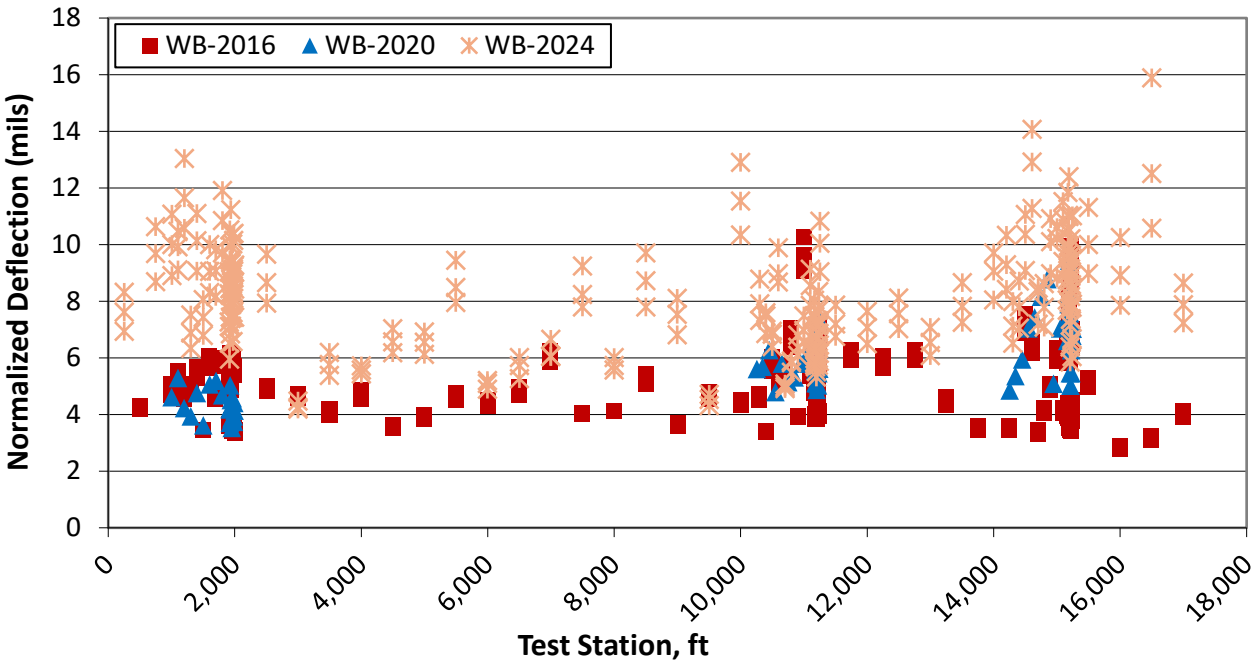

Figure 21. Graph. WB transverse leave joint normalized deflection in 2016, 2020, and 2024.

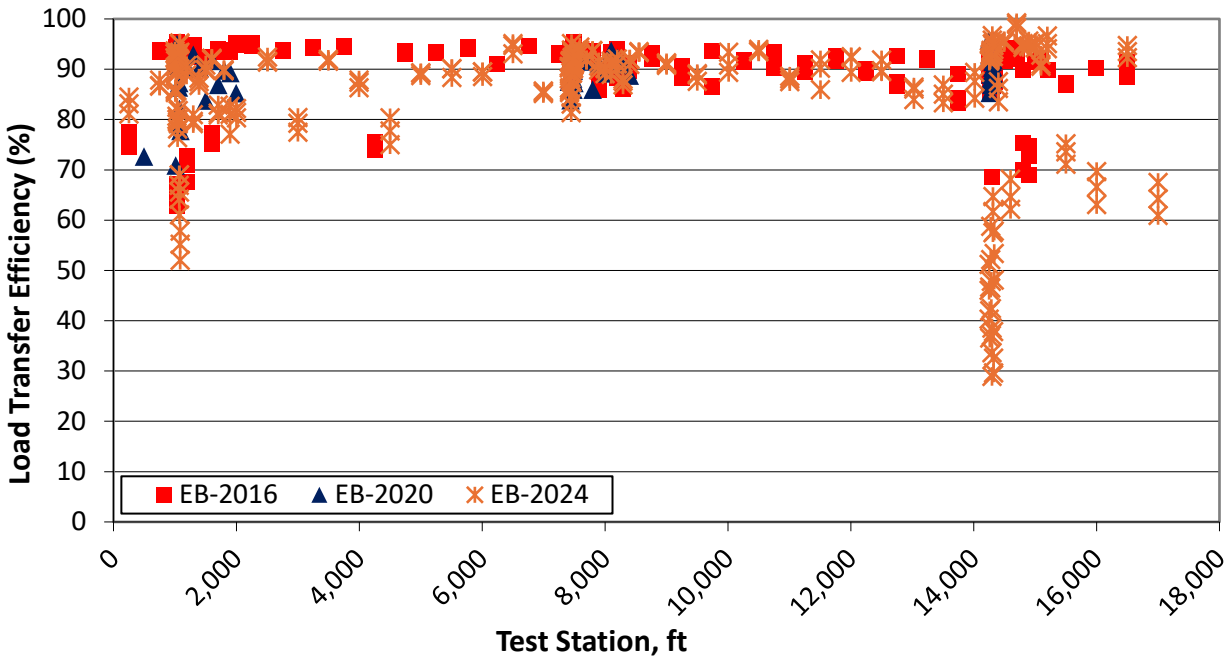

Figure 22. Graph. EB transverse joint (leave) load transfer efficiency (2016, 2020, and 2024).

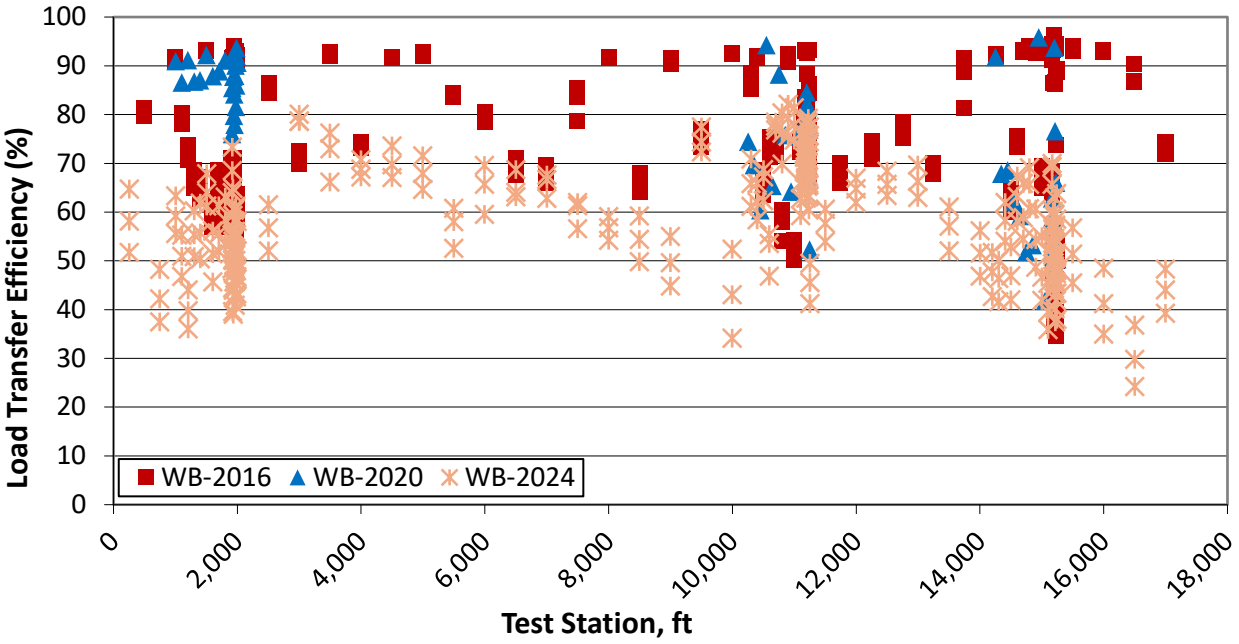

Figure 23. Graph. WB transverse joint (leave) load transfer efficiency (2016, 2020, and 2024).

Figure 24 and Figure 25 show the relationship between transverse joint LTE (%) and deflection difference for EB and WB directions in 2016, 2020, and 2024. While EB joints maintain a negative correlation, the 2024 data show greater spread with lower LTE at varying deflections. WB joints display increased scatter over time, with 2024 showing higher variability at greater deflections.

Overall, both directions indicate gradual joint deterioration, with LTE becoming less responsive to changes in deflection differences.

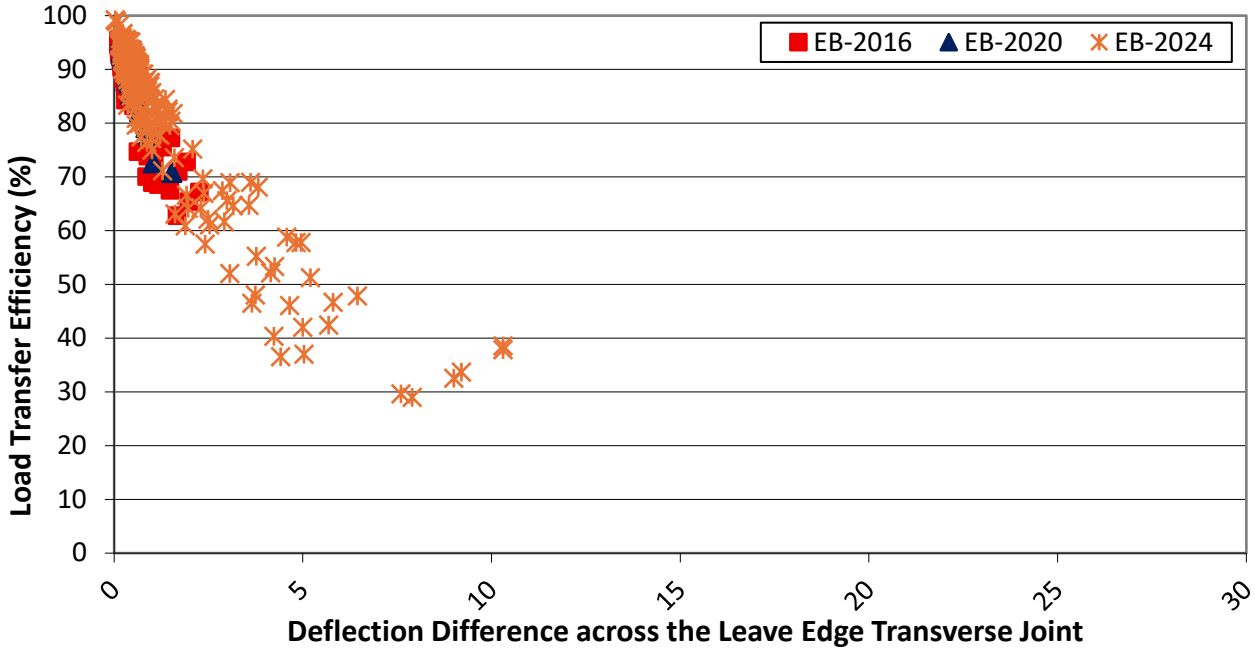

Figure 24. Graph. EB transverse joint load transfer efficiency vs deflection difference (2016, 2020, and 2024).

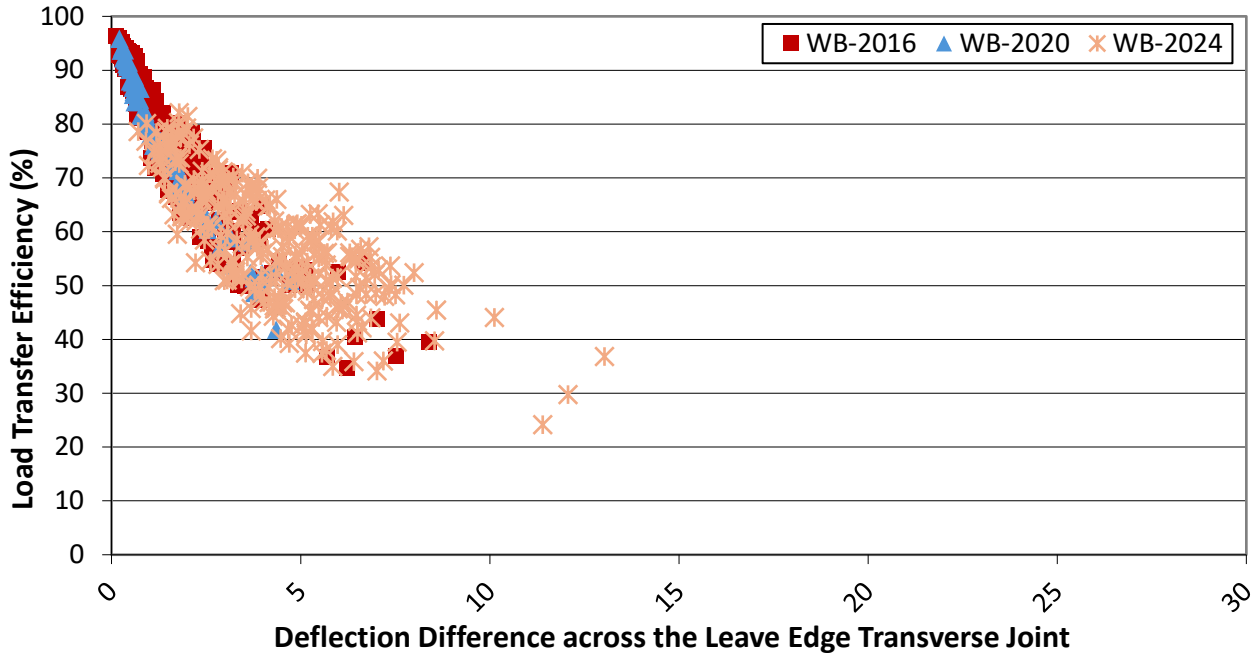

Figure 25. Graph. WB transverse joint load transfer efficiency vs deflection difference (2016, 2020, and 2024).

In the EB direction, normalized deflections along the longitudinal lane-shoulder joint peaked between stations 140+00 and 170+00, as seen in Figure 26, but were not always this high or variable. The WB direction showed greater magnitude and variability with deflections reaching up to 24 mils in 2024 (Figure 27). The driving lane-shoulder longitudinal joint exhibited nearly double the normalized deflections in 2024 compared to 2016, with increases of 95% in the EB direction and 84% in the WB direction (see Table 12). Although the percentage increase in deflection is greater for the EB direction, the average WB deflection is more than double the average EB deflection at the lane-shoulder joint. The lane-shoulder longitudinal joint LTE in both directions is shown in Figure 28 and Figure 29. The LTEs declined significantly over the eight-year period, reaching approximately 35% and 26%, respectively, in 2024 (Table 13).

Table 12. Normalized Deflections of Lane-Shoulder Longitudinal Joint (2016, 2020, and 2024)

Longitudinal Joint (LJ) Edge Normalized 9 kip Deflection						
	EB: 2016	**WB: 2016**	**EB: 2020**	**WB: 2020**	**EB: 2024**	**WB: 2024**
Average	3.40	7.20	4.49	7.51	6.51	13.27
Std Dev.	0.50	3.90	0.49	1.45	1.08	3.66
COV	15%	54%	11%	19%	17%	28%
4-yr change	N/A	N/A	32.1%	4.3%	45.0%	76.7%

Table 13. Load Transfer Efficiency of Lane-Shoulder Longitudinal Joint (2016, 2020, and 2024)

Right Longitudinal Joint (LJ) Edge Load Transfer Efficiency (LTE)						
	EB: 2016	**WB: 2016**	**EB: 2020**	**WB: 2020**	**EB: 2024**	**WB: 2024**
Average	93.82	52.02	76.45	53.14	35.49	26.47
Std Dev.	8.84	16.47	12.10	23.62	14.23	24.16
COV	9%	32%	16%	44%	40%	91%
4-yr change	N/A	N/A	−18.5%	−2.2%	−53.6%	−50.2%

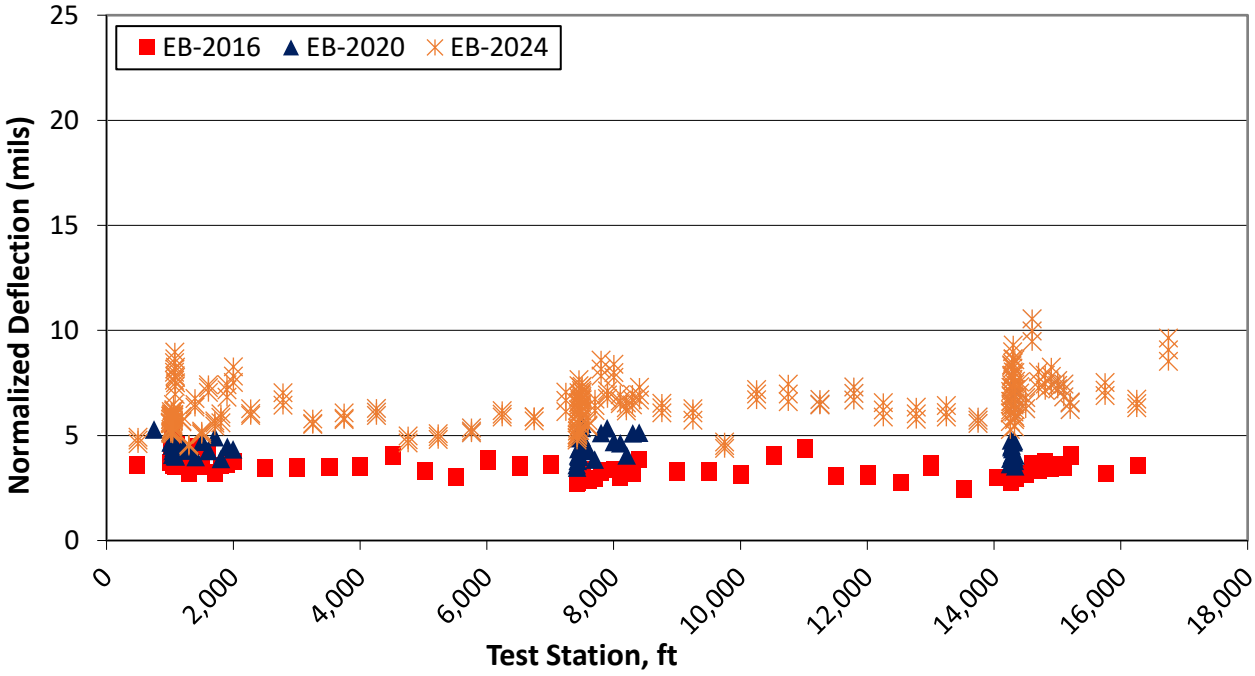

Figure 26. Graph. EB lane-shoulder longitudinal joint normalized deflection (2016, 2020, and 2024).

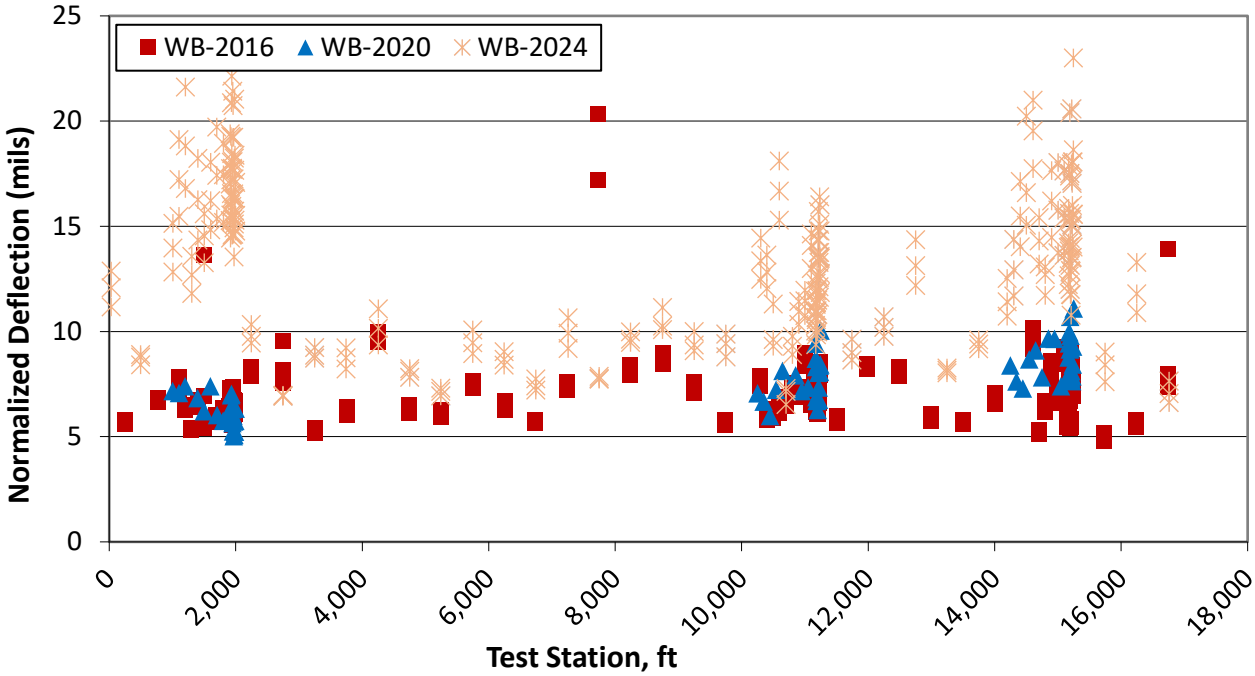

Figure 27. Graph. WB lane-shoulder longitudinal joint normalized deflection (2016, 2020, and 2024).

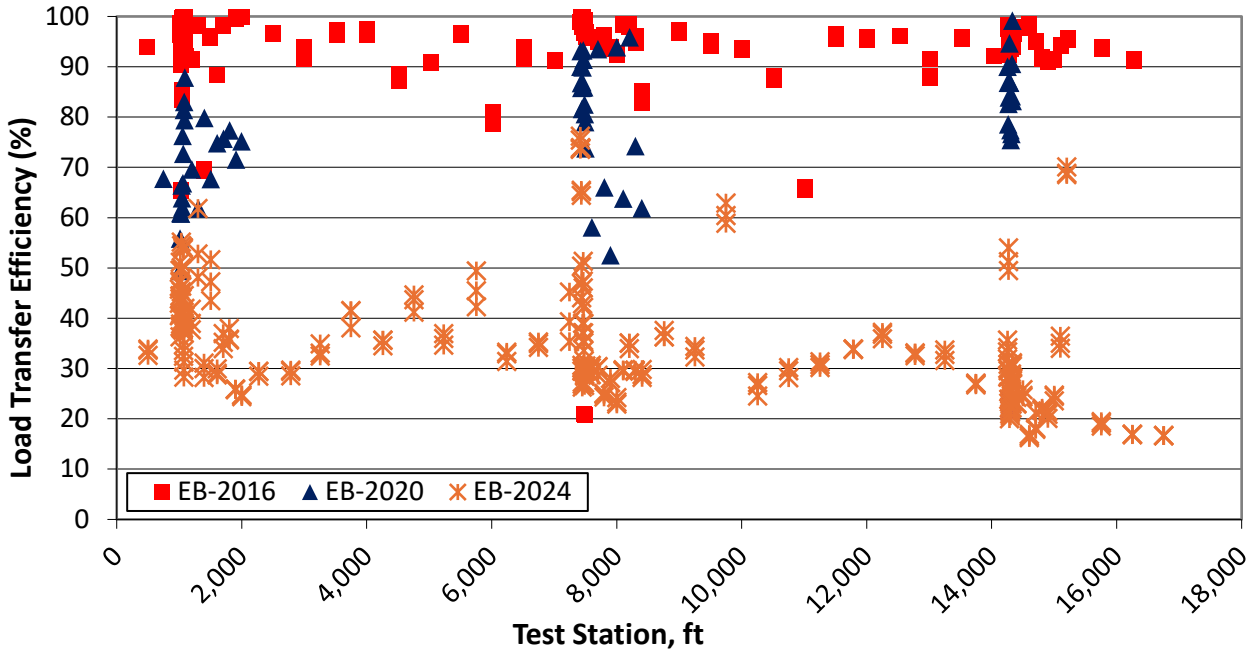

Figure 28. Graph. EB lane-shoulder longitudinal joint load transfer efficiency (2016, 2020, and 2024).

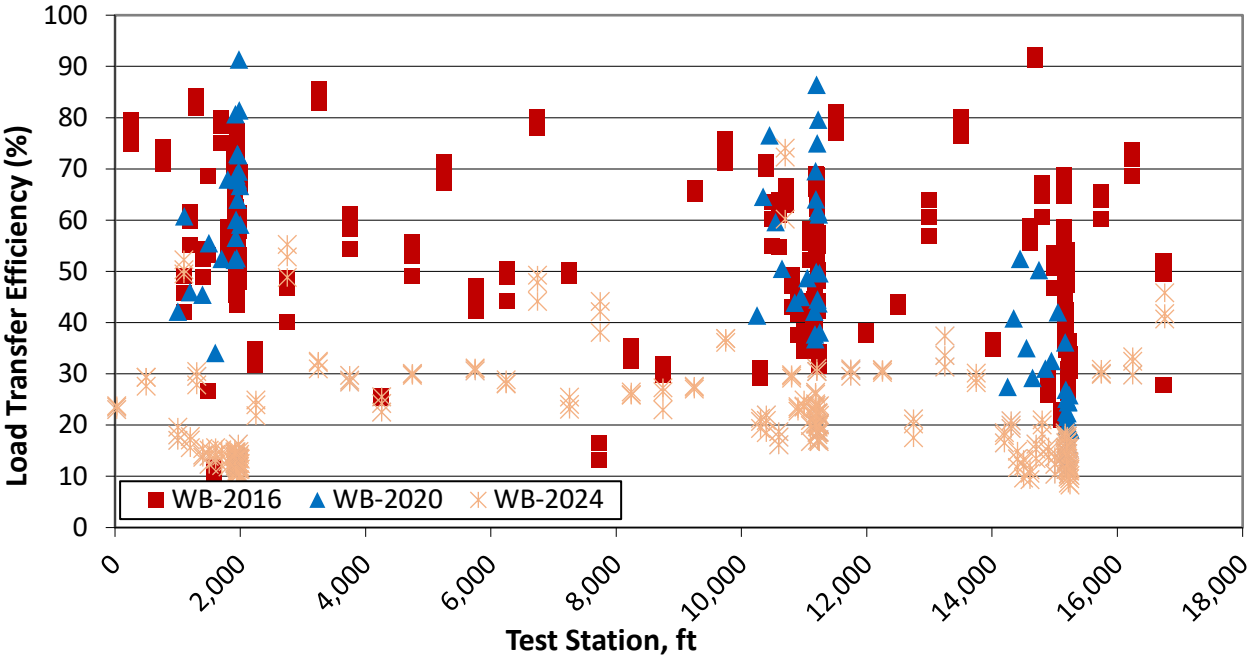

Figure 29. Graph. WB lane-shoulder longitudinal joint load transfer efficiency (2016, 2020, and 2024).

The significant increase in lane-shoulder joint deflection and reduction in the joint LTE in recent years may be indicative of material degradation and erosion occurring at the edge of the driving lane. Stripping and erosion of the HMA interlayer had been noted by DeSantis et al. (2022b) at the lane-shoulder joint while a definitive mechanism had not been determined for the WB lane-shoulder joint deflection increases. Figure 30 and Figure 31 illustrate the relationship between joint LTE and deflection difference across the longitudinal joints. Over time, the data have become increasingly scattered, with LTE showing less sensitivity to deflection differences, particularly at lower LTE values. This weakening correlation is more pronounced in the WB direction, indicating significant progressive deterioration along the longitudinal joints. Notably, this trend is more evident in longitudinal joints compared to transverse joints (Figure 24 and Figure 25), suggesting a greater loss of structural integrity along the longitudinal direction.

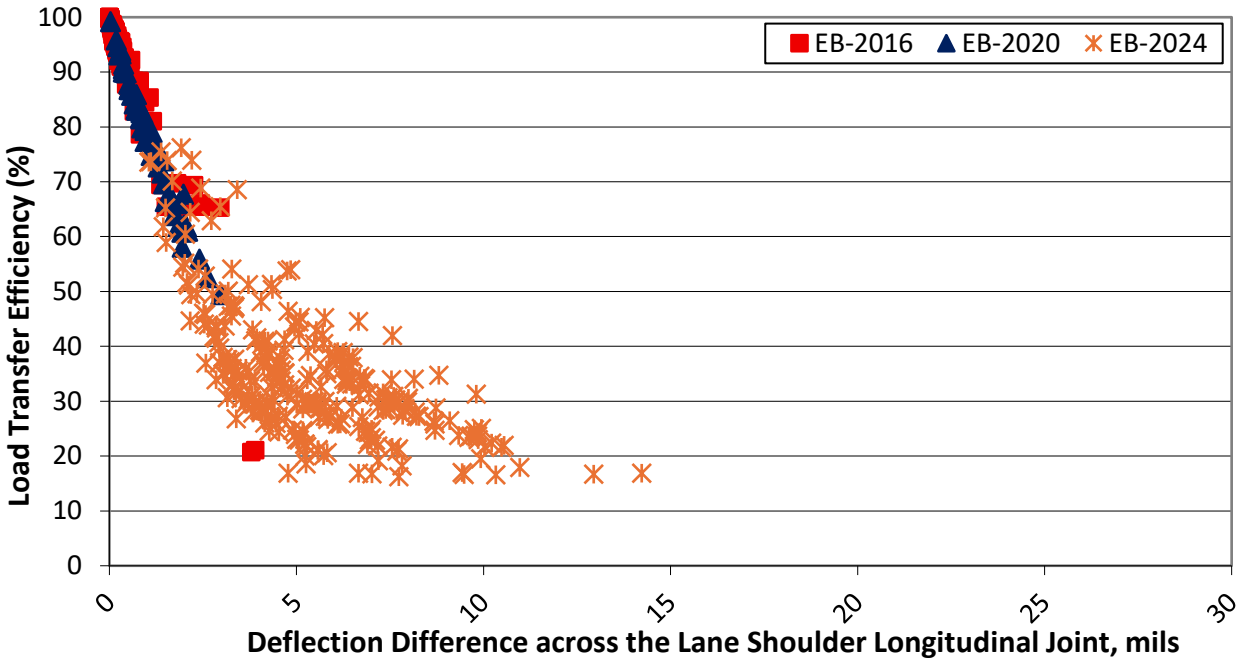

Figure 30. Graph. EB lane-shoulder longitudinal joint load transfer efficiency vs deflection difference (2016, 2020, and 2024).

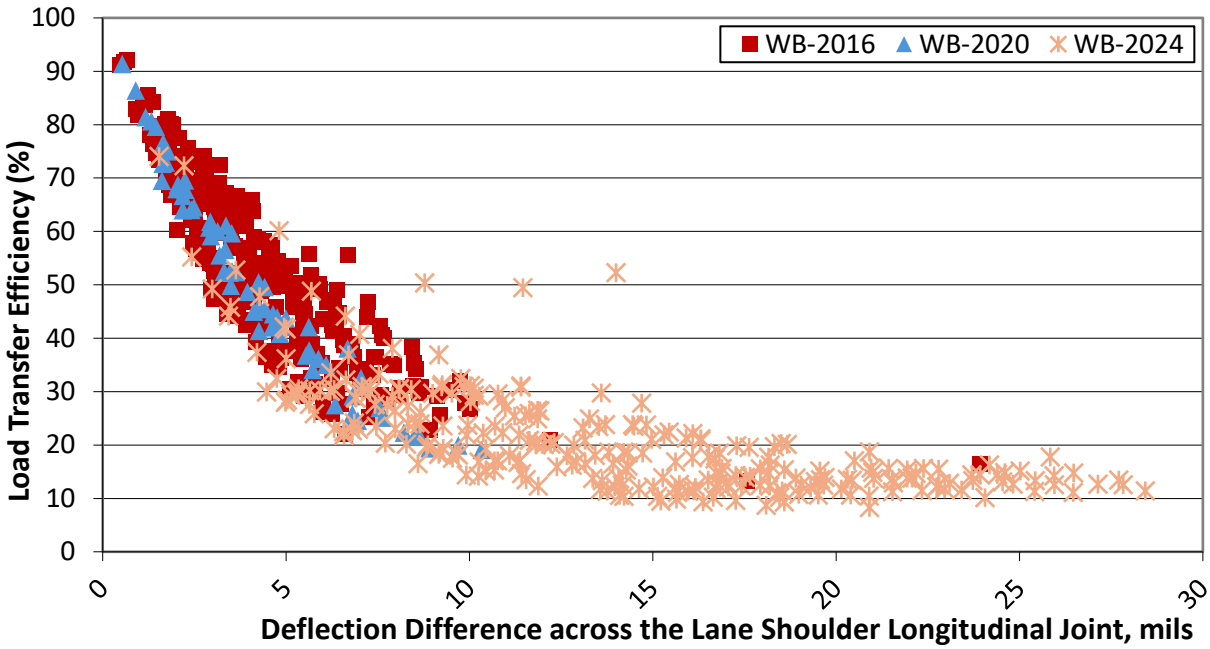

Figure 31. Graph. WB lane-shoulder longitudinal joint load transfer efficiency vs deflection difference (2016, 2020, and 2024).

The normalized deflections at the outer driving lane corner of the slabs (leave) increased by more than 100% in both the EB and WB directions between 2016 and 2024 (Table 14) but were still the highest in the WB direction. The LTE at the corner drop location in the outer driving lane had similar behavior to the transverse joint LTE and LTE across the lane-shoulder joint. Although a substantial decline in load transfer efficiency was observed in both transverse and longitudinal directions, the transverse joint still had a much higher LTE relative to the longitudinal joint LTE at the corner load location (see Table 15 and Table 16). Furthermore, the LTE across the transverse joint was higher in the EB than WB direction (79% vs. 53%), but more similar LTE (33% vs. 24%) was measured across the lane-shoulder joint.

In the EB direction, the slab corners showed the highest normalized deflections and lowest load transfer efficiencies across the transverse and longitudinal joints near the end of the section (i.e., 140+00 ft to 180+00 ft) (see Figure 32, Figure 34, and Figure 36). The WB section exhibited high variability in the deflection and LTE measurements, as seen by the calculated COV values in Tables 14–16, Figure 33, Figure 35, and Figure 37.

Table 14. Outer Driving Lane Normalized Leave Corner Deflections (2016, 2020, and 2024)

Outer Driving Lane Normalized Leave Corner (CN) 9 kip Deflection						
	EB: 2016	**WB: 2016**	**EB: 2020**	**WB: 2020**	**EB: 2024**	**WB: 2024**
Average	3.56	8.63	4.57	9.69	7.54	14.31
Std. Dev.	0.73	3.02	0.53	2.92	2.19	3.08
COV	20%	35%	12%	30%	29%	22%
4-yr change	N/A	N/A	28.4%	12.3%	65.0%	47.7%

Table 15. Outer Driving Lane Corner LTE across Transverse Joint (2016, 2020, and 2024)

Outer Driving Lane Corner (CN) LTE across Transverse Joints						
	EB: 2016	**WB: 2016**	**EB: 2020**	**WB: 2020**	**EB: 2024**	**WB: 2024**
Average	90.11	71.50	88.60	63.44	79.32	52.88
Std. Dev.	6.13	19.29	5.01	16.35	16.16	10.15
COV	7%	27%	6%	26%	20%	19%
4-yr change	N/A	N/A	−1.7%	−11.3%	−10.5%	−16.6%

Table 16. Outer Driving Lane Corner LTE across Lane-Shoulder Joint (2016, 2020, and 2024)

Corner (CN) LTE across Lane-Shoulder Joint						
	EB: 2016	**WB: 2016**	**EB: 2020**	**WB: 2020**	**EB: 2024**	**WB: 2024**
Average	94.21	45.63	74.94	44.25	33.41	24.44
Std Dev.	6.22	18.77	12.93	24.88	17.32	24.07
COV	7%	41%	17%	56%	52%	98%
4-yr change	N/A	N/A	−20.5%	−3.0%	−55.4%	−44.8%

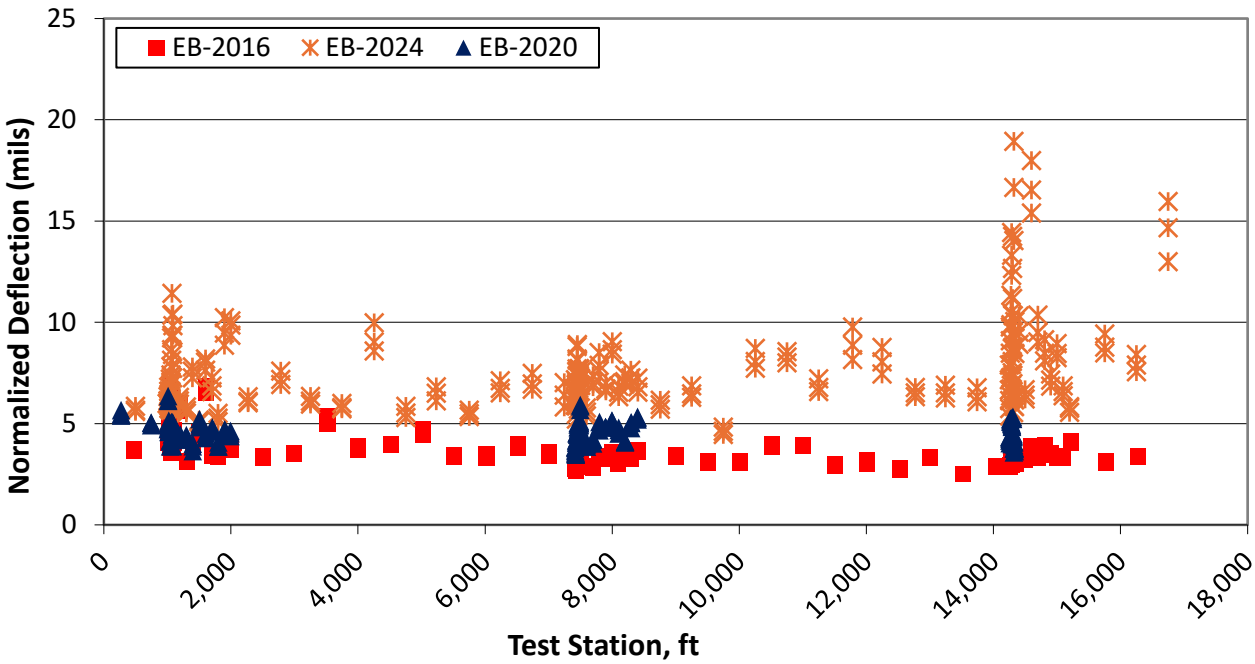

Figure 32. Graph. EB leave slab corner normalized deflection (2024, 2020, and 2016).

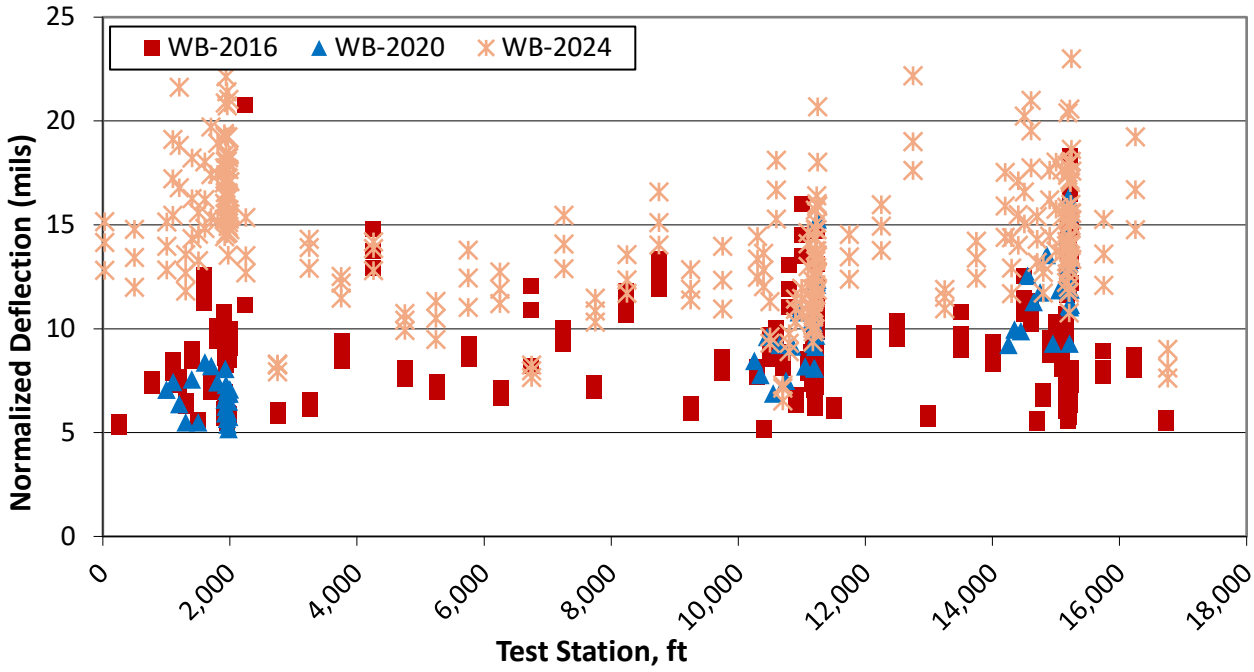

Figure 33. Graph. WB leave slab corner normalized deflection (2024, 2020, and 2016).

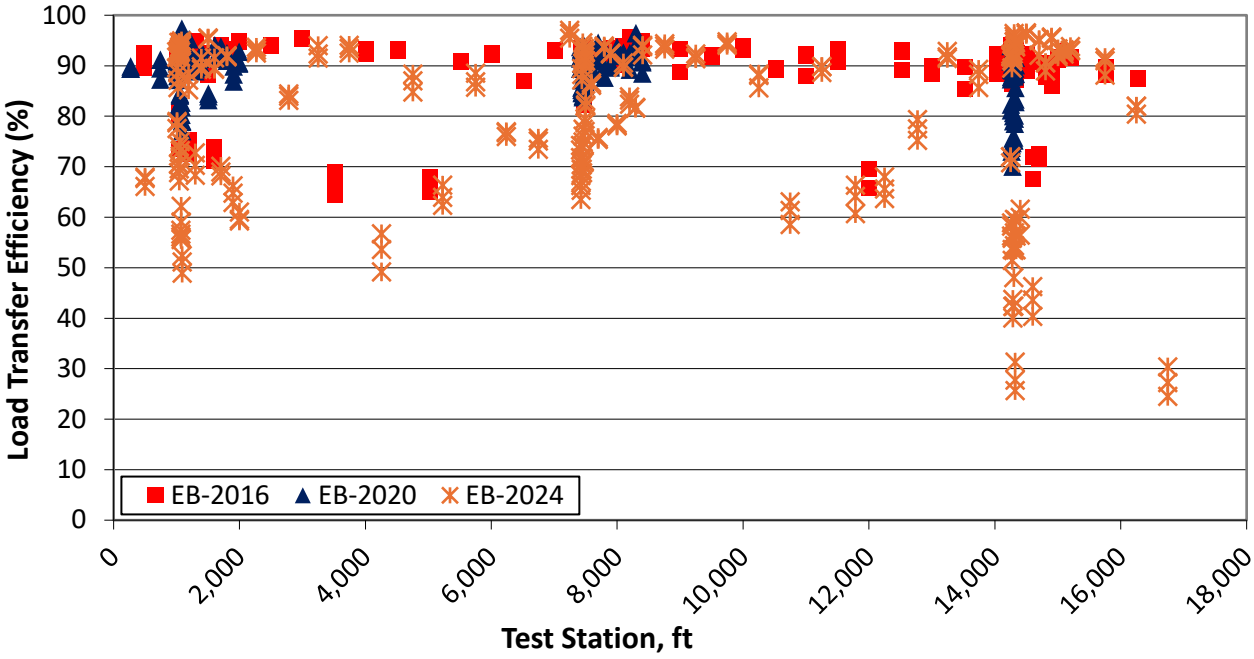

Figure 34. Graph. EB load transfer efficiency at slab corner across transverse joints (2016, 2020, and 2024).

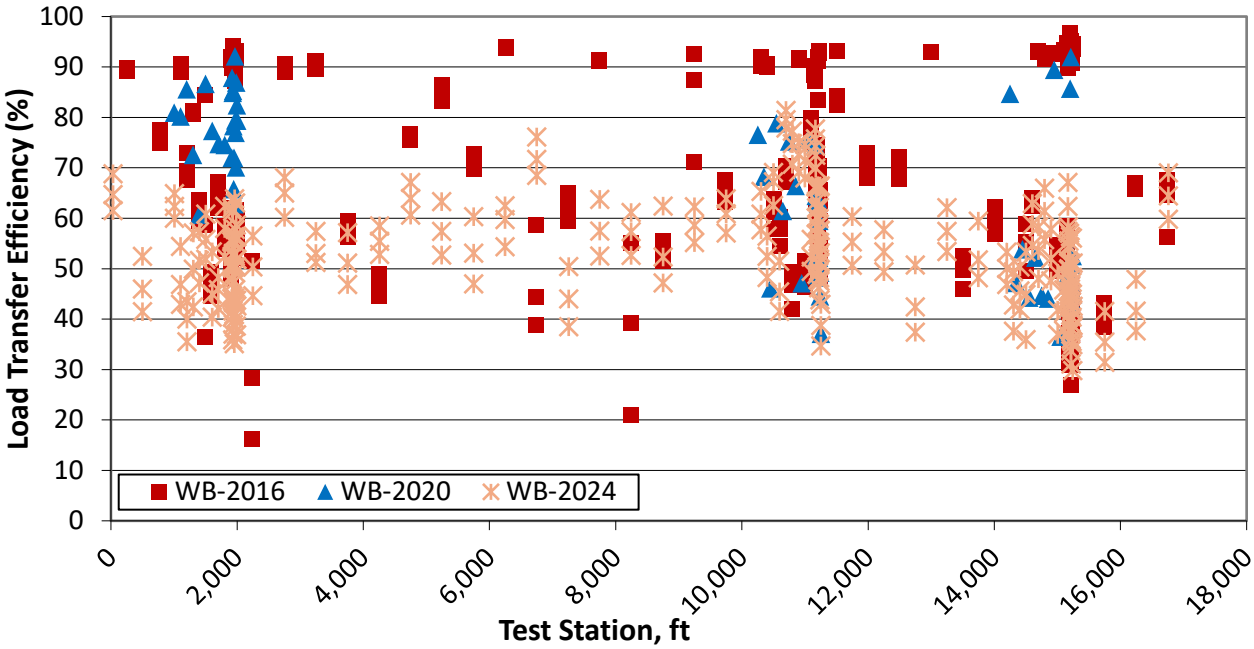

Figure 35. Graph. WB load transfer efficiency at slab corner across transverse joints (2016, 2020, and 2024).

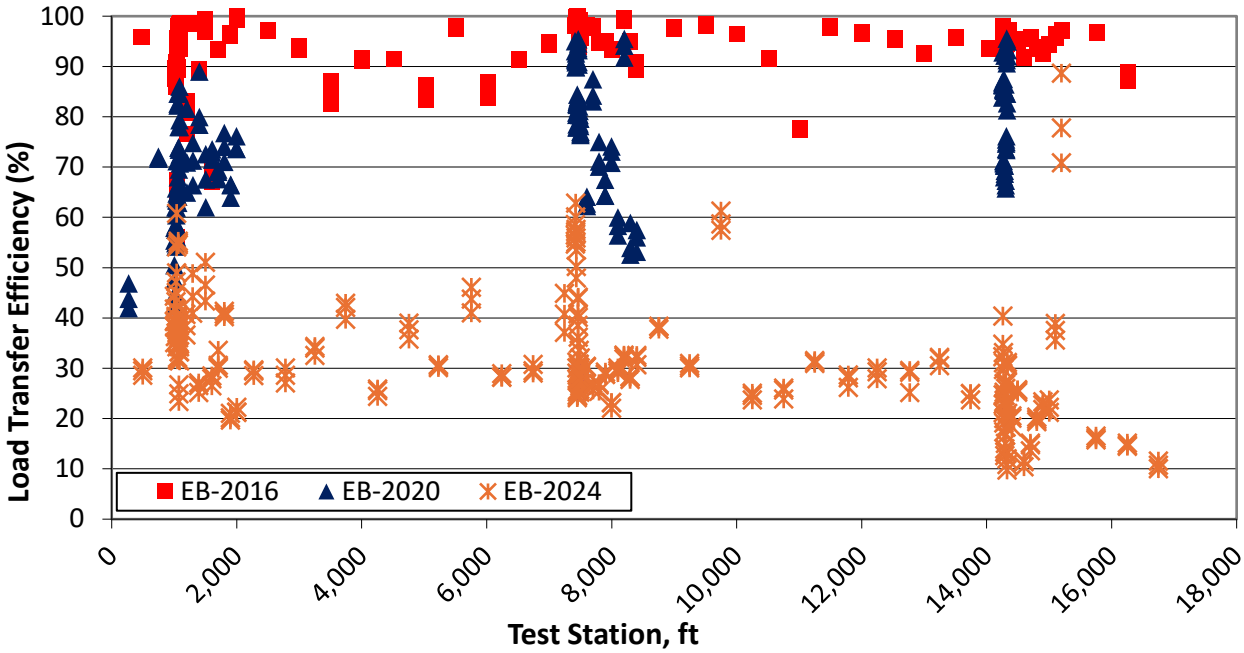

Figure 36. Graph. EB load transfer efficiency at slab corner across longitudinal joints (2016, 2020, and 2024).

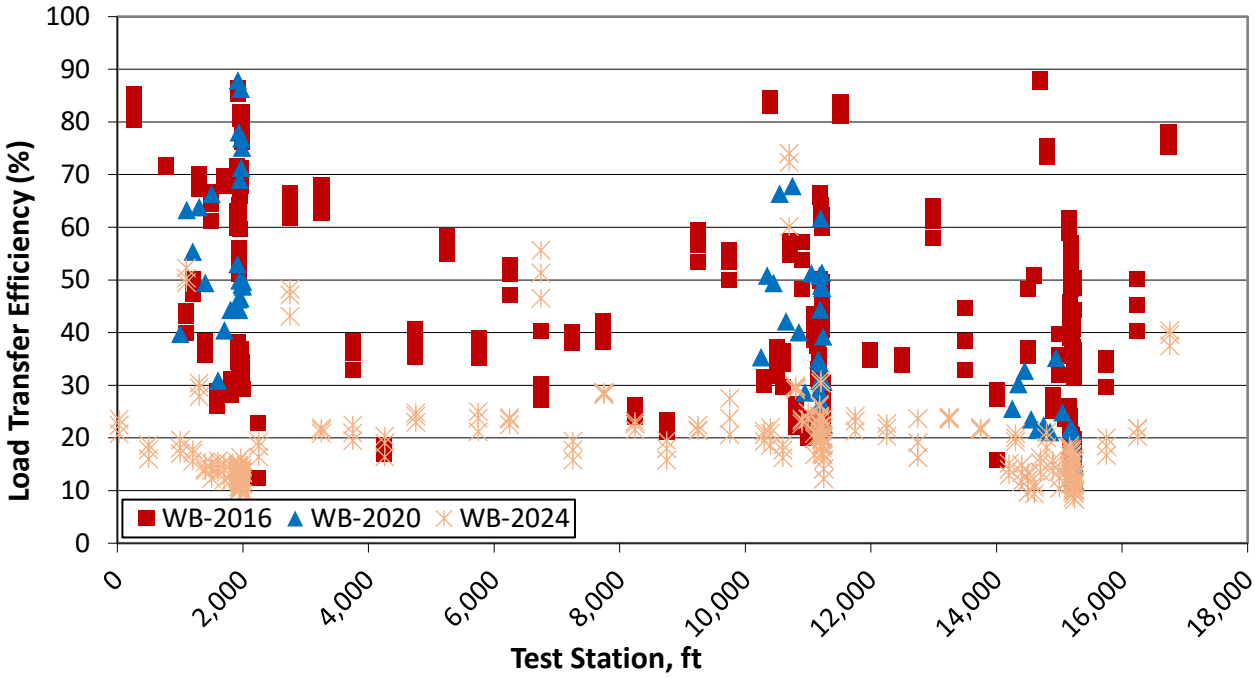

Figure 37. Graph. WB load transfer efficiency at slab corner across longitudinal joints (2016, 2020, and 2024).

The 2024 FWD testing showed that the EB section had lower deflection magnitudes and higher LTE, which typically suggests better structural and distress performance. Furthermore, the WB section had higher variability in deflection and joint LTE. However, the current visual performance of the sections showed that the EB section had significant longitudinal cracking (3.8%) relative to the WB one (none). The FWD test results confirmed the deterioration of the longitudinal (contraction) joint LTE in both directions over time, which did not have a steel tie bar. Both contraction joints had macrofibers, which did not effectively prevent the deterioration of the LTE (or reduce the joint opening) across the longitudinal joint.

FWD Back-Calculation for Modulus of Subgrade Reaction (k-value) and Effective Thickness (h_{eff})

To overcome the limitations of traditional rigid pavement back-calculation methods that assume an infinite slab over a spring foundation, this study adopted the approach proposed by King and Roesler (2014), which accounts for finite-size slab panels (4 to 6 ft) for bonded concrete overlays of asphalt with variable load transfer efficiency. The $AREA_{24}$ parameter, as defined by the equation in Figure 38, was introduced to characterize the FWD deflection basin of short panel sizes and relate to the radius of relative stiffness of the slab system (King & Roesler, 2014).

$$AREA_{24} = 6(1 + 2\frac{d_{12}}{d_0} + \frac{d_{24}}{d_0})$$

Figure 38. Equation. $AREA_{24}$ for characterizing the FWD deflection basin of short panel sizes and the radius of relative stiffness.

Source: King & Roesler (2014)

Where d_0, d_{12}, and d_{24} are normalized surface deflections at 0, 12, and 24 in. offset distance from the center of the load plate. Based on $AREA_{24}$, the radius of relative stiffness (l) and nondimensional interior deflection (W_{int}) are calculated from the published regression model coefficients for different average LTE values and for the test section's slab size (i.e., 6 × 6 ft). For this analysis, the average LTE was calculated as an average of LTE values in transverse (LTEy) and longitudinal direction (LTEx) along the section, as summarized for the EB and WB directions in Table 17.

Table 17. Average Load Transfer Efficiency (2016, 2020, and 2024)

	EB: 2016	WB: 2016	EB: 2020	WB: 2020	EB: 2024	WB: 2024
Average LTE	92.2	65.1	82.3	63.7	59.9	42.3

Assuming Poisson's ratio of 0.15 and a modulus of elasticity of 5,000,000 psi for a 6 × 6 ft slab, the modulus of subgrade reaction (k-value) and effective thickness (h_{eff}) was calculated for the EB and WB directions (Table 18 and Table 19). Here the effective thickness (h_{eff}) represents the total structural capacity of the existing CRCP slab, interlayer, and concrete overlay.

Table 18. Back-Calculated Modulus of Subgrade Reaction (2016, 2020, and 2024)

Back-Calculated Modulus of Subgrade Reaction (k-value)—psi/in						
	EB: 2016	**WB: 2016**	**EB: 2020**	**WB: 2020**	**EB: 2024**	**WB: 2024**
Average	427	283	441	341	376	306
Std. Dev.	58	94	61	71	89	65
COV	13%	33%	14%	21%	24%	21%

Table 19. Back-Calculated Effective Thickness Slab (2016, 2020, and 2024)

Back-Calculated Effective Thickness Slab (h_{eff})—inches						
	EB: 2016	**WB: 2016**	**EB: 2020**	**WB: 2020**	**EB: 2024**	**WB: 2024**
Average	13.1	11.1	10.0	9.7	9.6	9.3
Std Dev.	2.2	2.1	1.8	1.1	1.1	1.3
COV	17%	19%	18%	11%	12%	14%

As seen in Table 18 and Table 19, the section trends in k-value and h_{eff} follow expected values with the new concrete overlay showing the greatest k-value and h_{eff} in 2016. The WB NWGF section was also expected to have lower h_{eff} than the EB one, as seen in Table 19. The variation of h_{eff} for the EB section and directions are shown in Figure 39 and Figure 40 for all three FWD testing years. Over time, the EB h_{eff} has decreased by 27% and k-value decreased by 12%, while the WB section has seen a decrease in h_{eff} of 16% and a slight increase in k-value of 8%. The higher measured center slab deflections and lower LTE across the joints have resulted in a reduction in h_{eff} with time, which may indicate a reduction in the composite action of the pavement cross-section. However, the biggest change with time was the transverse and longitudinal LTE (average absolute reduction of 35%), which affects the deflections and the back-calculated h_{eff}. Furthermore, LTE was shown to vary along the sections and had different magnitudes for transverse and longitudinal joints, which was not accounted for during each FWD back-calculation but only the directional LTE values in either the longitudinal or transverse joints. Overall, the EB and WB directions are behaving as 9.6 to 9.3 in. effective concrete slabs, respectively, after nine years (2015 to 2024).

The back-calculated k-values for the EB and WB directions are shown in Figure 41 and Figure 42. At year nine of the test sections (2024), the support is good in each direction (376 vs. 306 psi/in.) as well as the variation within the section. Given most of the changes in the test section have come from loss in LTE and some evidence of HMA interlayer stripping, it is not expected to see significant long-term changes to the support k-value.

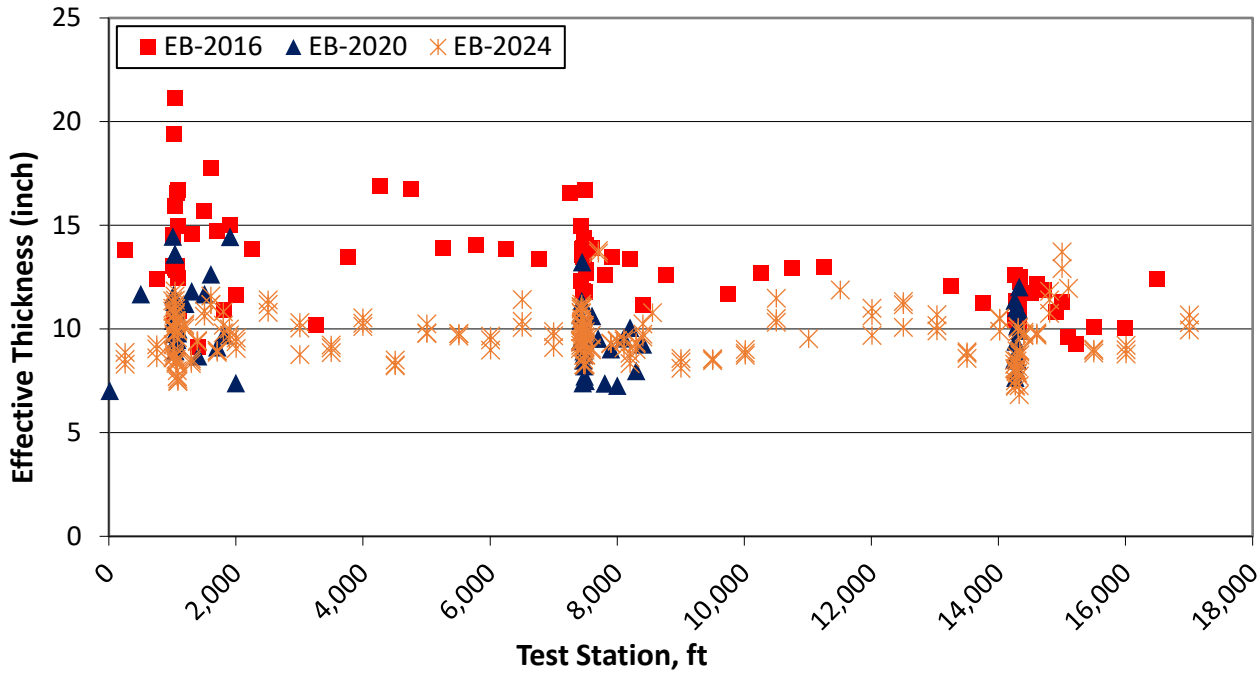

Figure 39. Graph. Effective slab thickness for EB direction (2016, 2020, and 2024).

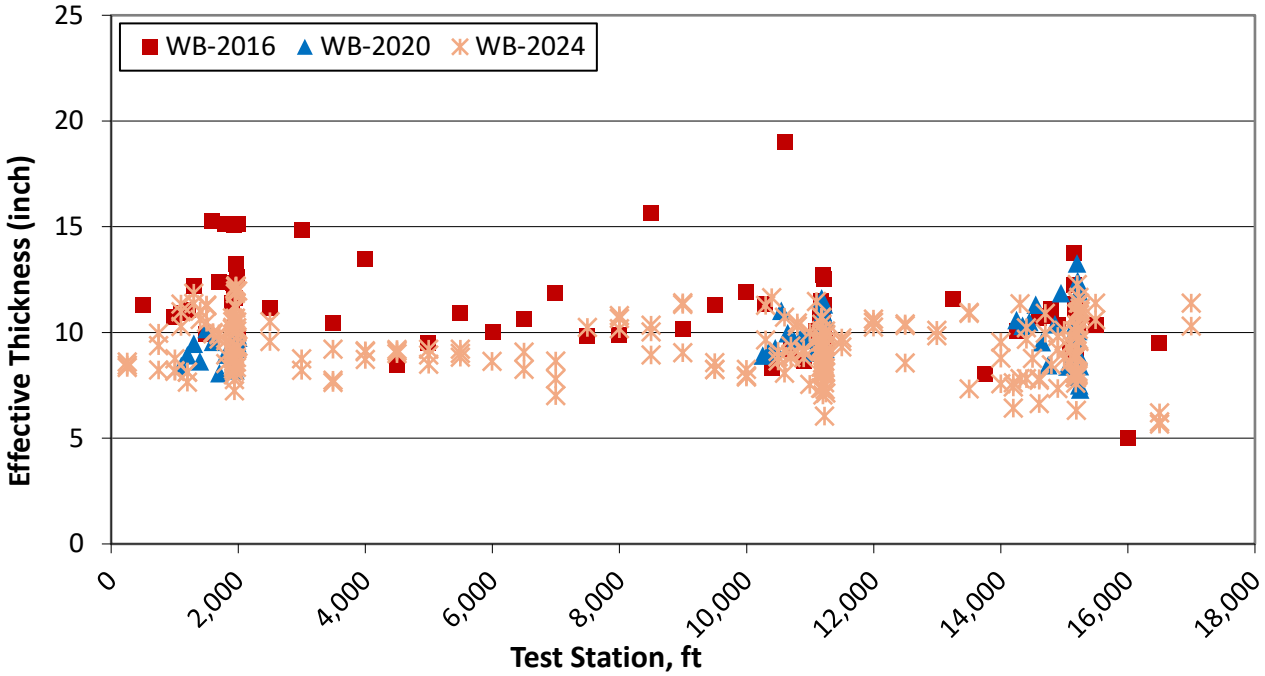

Figure 40. Graph. Effective slab thickness for WB direction (2016, 2020, and 2024).

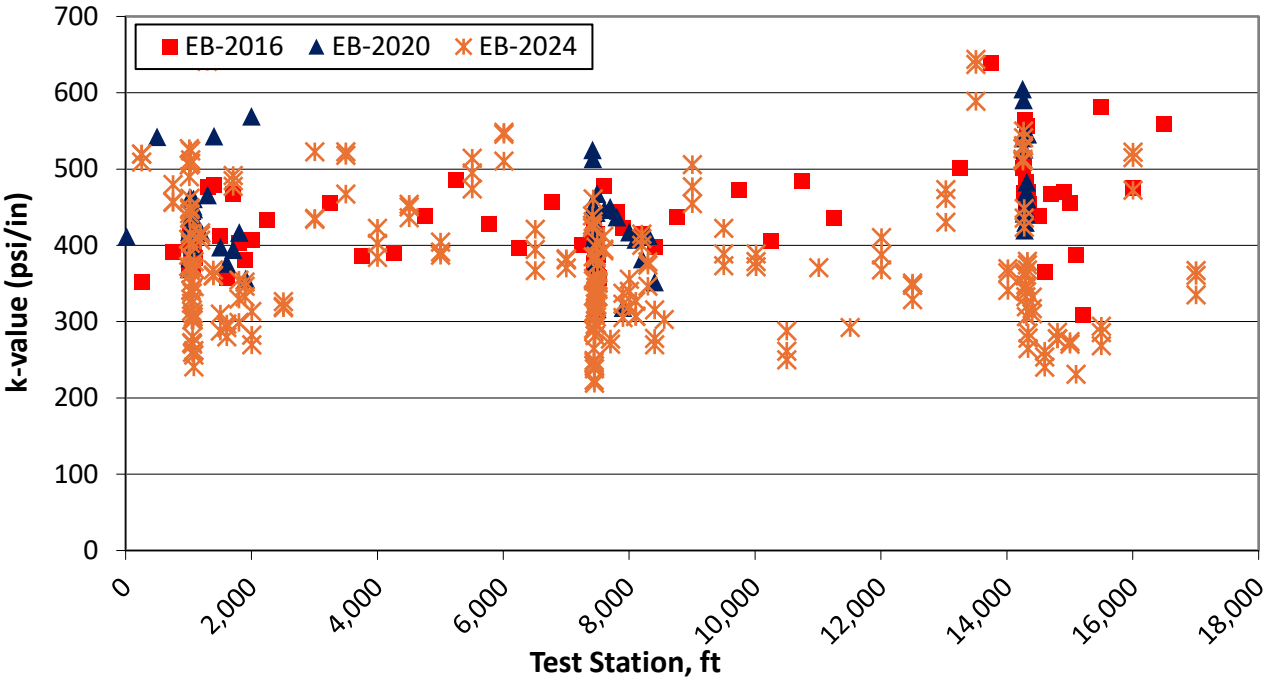

Figure 41. Graph. Back-calculated modulus of subgrade reaction for EB direction (2016, 2020, and 2024).

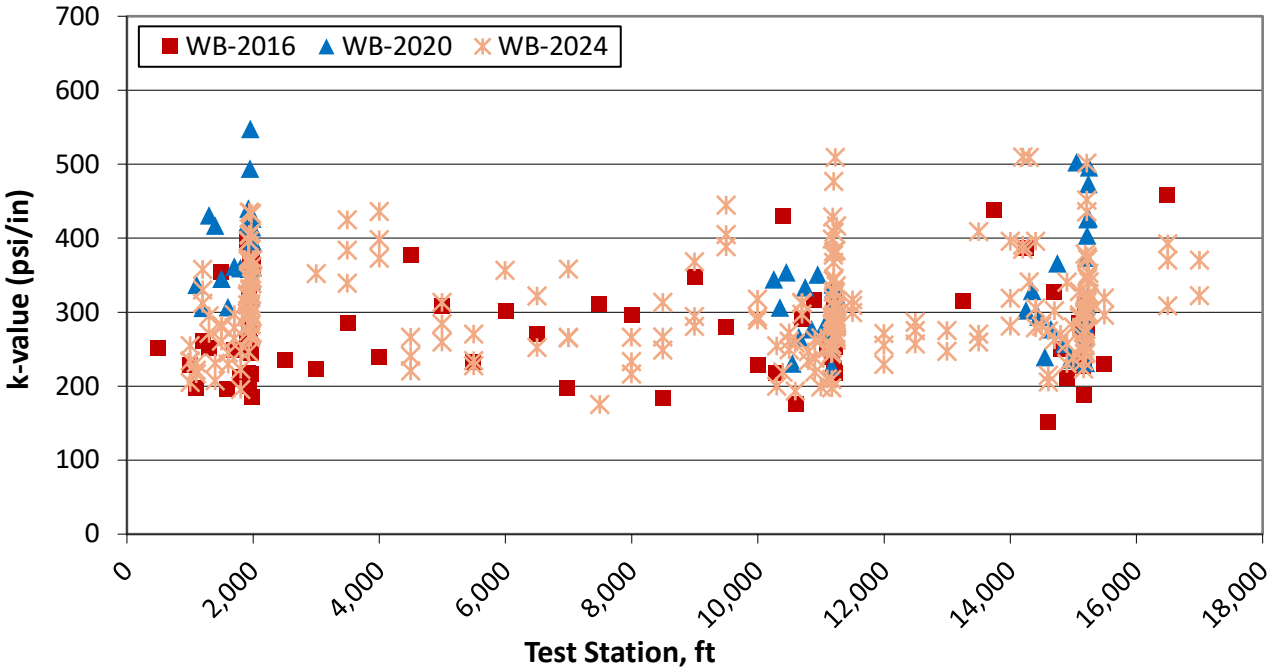

Figure 42. Graph. Back-calculated modulus of subgrade reaction for WB direction (2016, 2020, and 2024).

INTERNATIONAL ROUGHNESS INDEX

In 2016, the average international roughness index (IRI) values in the EB and WB directions were reported in IROADS as 48 and 62, respectively. The average IRI values in 2021 were 50 and 66 in./mi in the EB and WB directions, respectively (DeSantis & Roesler, 2022a). Additional profilometer testing was conducted on the I-72 experimental UBOL in fall 2024 (October 10, 2024) and spring 2025 (March 25, 2025). The pavement surface roughness was measured in the right wheel path (RWP) and left wheel path (LWP) of the driving and passing lanes. The IRI values versus station were compared with the corresponding FWD deflections to determine if IRI could be related to the transverse joint deflection variations. Table 20 and Table 21 summarize the most recent IRI values observed in fall 2024 and spring 2025.

Table 20. Average IRI and Leave Joint Deflection in EB Driving and Passing Lanes

	DL LWP IRI (in./mi)	DL RWP IRI (in./mi)	DL AVG IRI (in./mi)	PL LWP IRI (in./mi)	PL RWP IRI (in./mi)	PL AVG IRI (in./mi)	Leave Edge Deflection (mils)
2016	N/A	N/A	48	N/A	N/A	N/A	N/A
2021	N/A	N/A	50	N/A	N/A	N/A	N/A
Fall 2024	54.7	62.9	58.8	57.8	59.6	58.7	4.39
Spring 2025	51.5	56.9	54.2	49.8	53.7	51.7	N/A
N/A	N/A	N/A	N/A	N/A	**2025 AVG**	***53.0***	N/A

Driving and passing lanes are DL and PL, respectively.

Table 21. Average IRI and Leave Joint Deflection in WB Driving and Passing Lanes

	DL LWP IRI (in./mi)	DL RWP IRI (in./mi)	DL AVG IRI (in./mi)	PL LWP IRI (in./mi)	PL RWP IRI (in./mi)	PL AVG IRI (in./mi)	Leave Edge Deflection (mils)
2016	N/A	N/A	62	N/A	N/A	N/A	N/A
2021	N/A	N/A	66	N/A	N/A	N/A	N/A
Fall 2024	84.4	83.3	83.9	57.1	57.7	57.4	8.1
Spring 2025	79.0	79.6	79.3	53.5	54.6	54.1	N/A
N/A	N/A	N/A	N/A	N/A	**2025 AVG**	***66.7***	N/A

Driving and passing lanes are DL and PL, respectively.

Relative to the 2021 IRI values, the 2024/2025 values were higher in the EB and WB directions by 10% and 22%, respectively. Focusing just on the driving lane IRI (2025), an increase of 8% in the EB direction and 20% in the WB direction occurred from 2021 to 2025. The IRI values for EB driving and passing lanes were very similar, but the WB driving lane had significantly higher IRI than the WB passing lane (25 in./mi). The minor changes in IRI from fall 2024 to spring 2025 for all lanes and directions can be attributed to the seasonal (temperature) effects. While the RWP and LWP IRI values were similar for the WB direction, the difference between RWP and LWP IRI values in the EB driving lane was 8 in./mi in 2024.

According to FHWA pavement performance thresholds (IRI < 95 in./mi = Good, 95–170 = Fair, > 170 = Poor), all IRI values measured on the I-72 UBOL remain in the Good category. Even the highest recent values in the WB section in fall 2024 (~84 in./mi) are below the 95 in./mi threshold. Thus, despite seasonal increases noted in spring vs. fall measurements, ride quality is consistently rated as Good across both directions and lanes.

Moreover, IRI values are typically higher at the beginning and end of the section likely because of the beginning and ending of the paving day (Figure 43 and Figure 44). The WB driving lane has particularly high IRI values, reaching up to 120 in./mile (Figure 45 and Figure 46). The FWD deflection data did not strongly correlate to IRI values at individual stations. The higher IRI value for the WB driving lane was likely due to its original high value after construction, which may be related to not having an HMA interlayer to level up the existing CRCP prior to the concrete overlay.

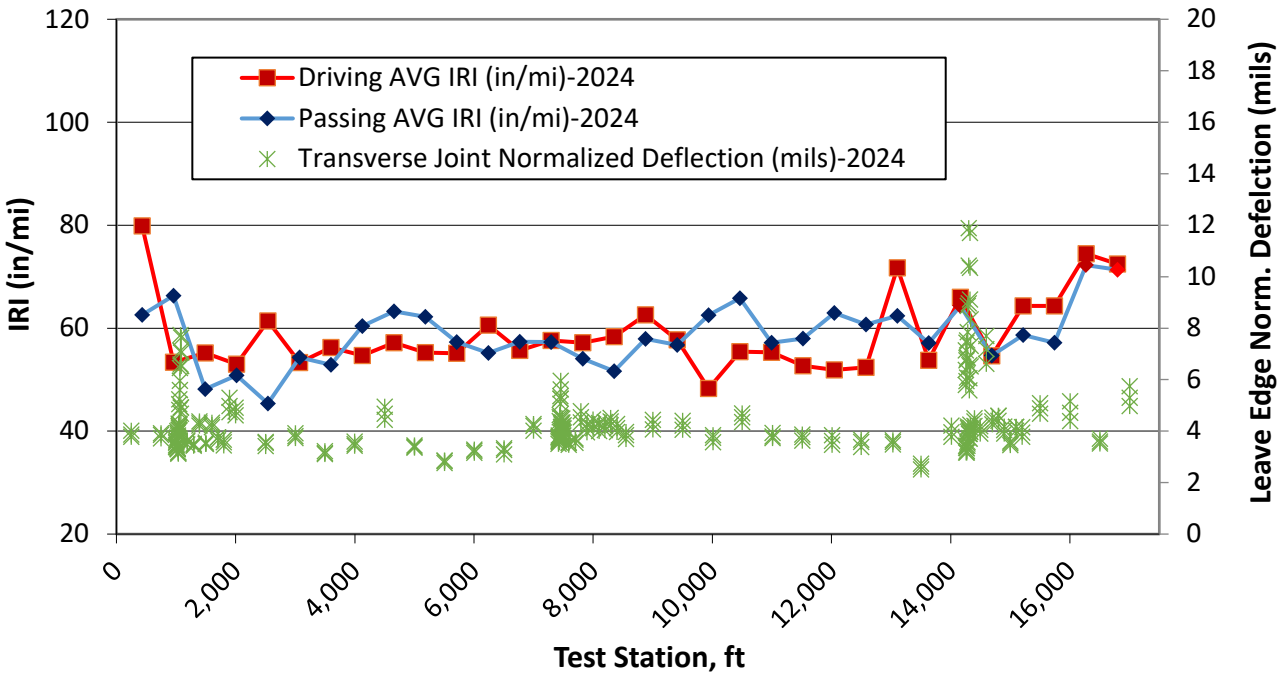

Figure 43. Graph. IRI and normalized transverse joint leave edge deflection along EB direction (fall 2024).

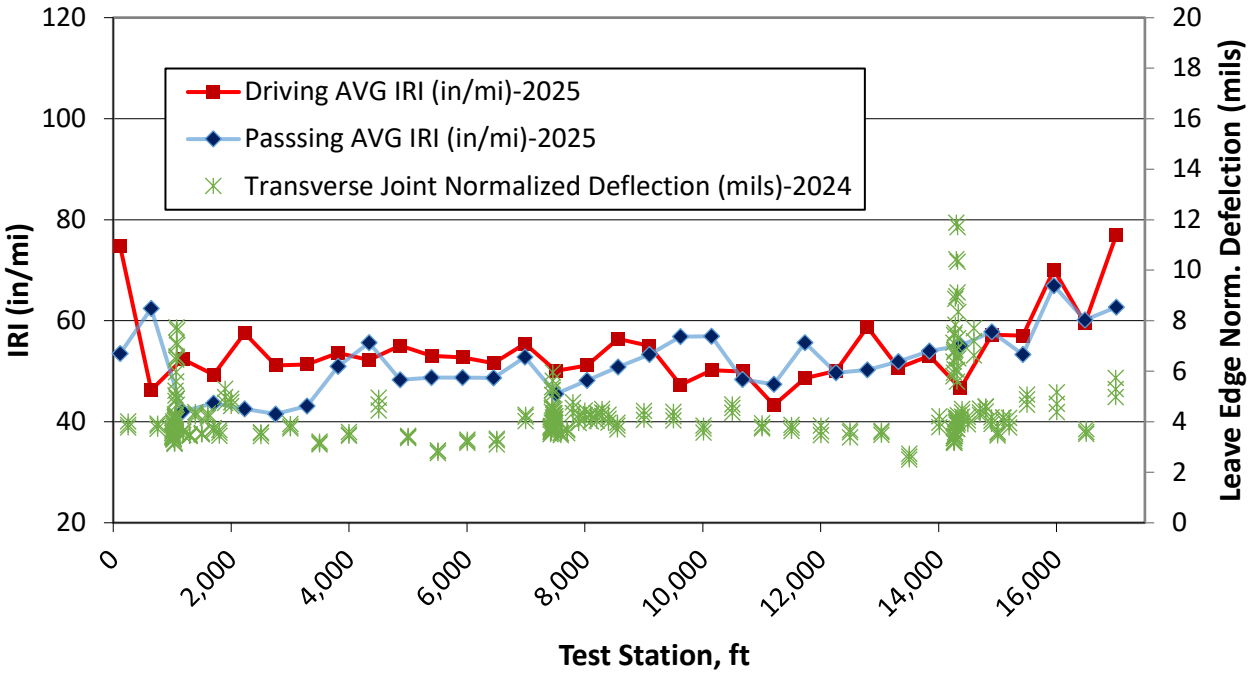

Figure 44. Graph. IRI and normalized transverse joint leave edge deflection along EB direction (spring 2025).

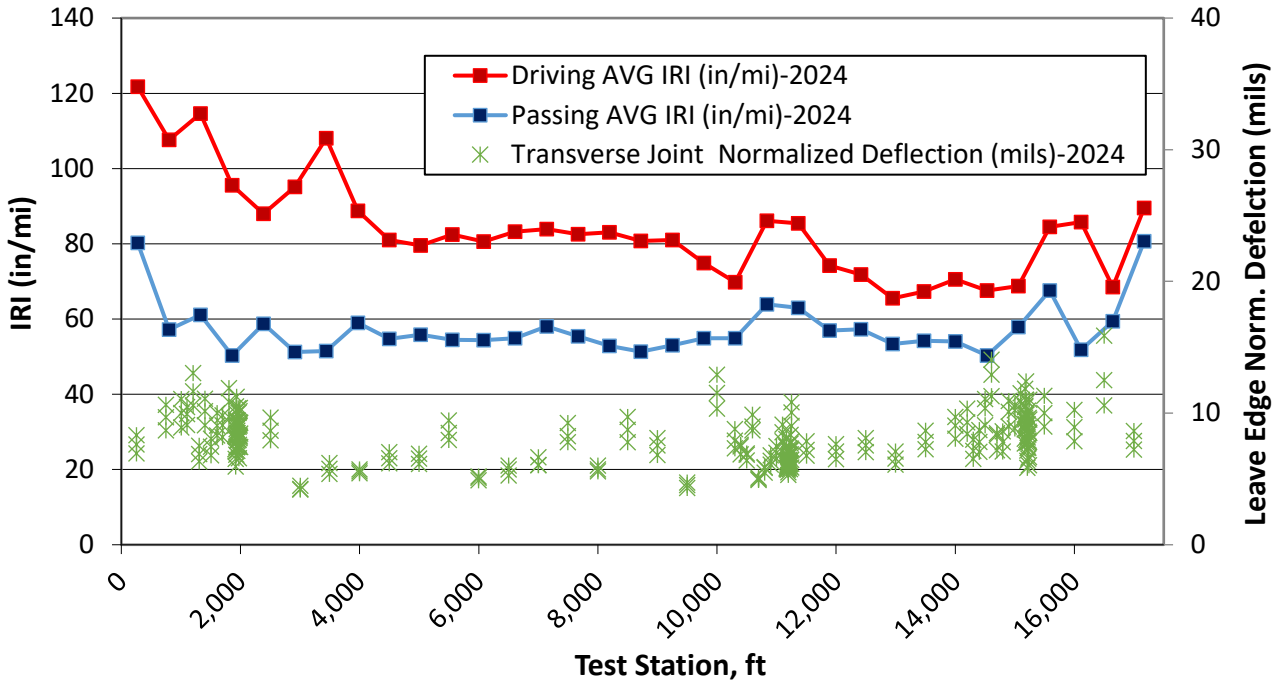

Figure 45. Graph. IRI and normalized transverse joint leave edge deflection along WB direction (fall 2024).

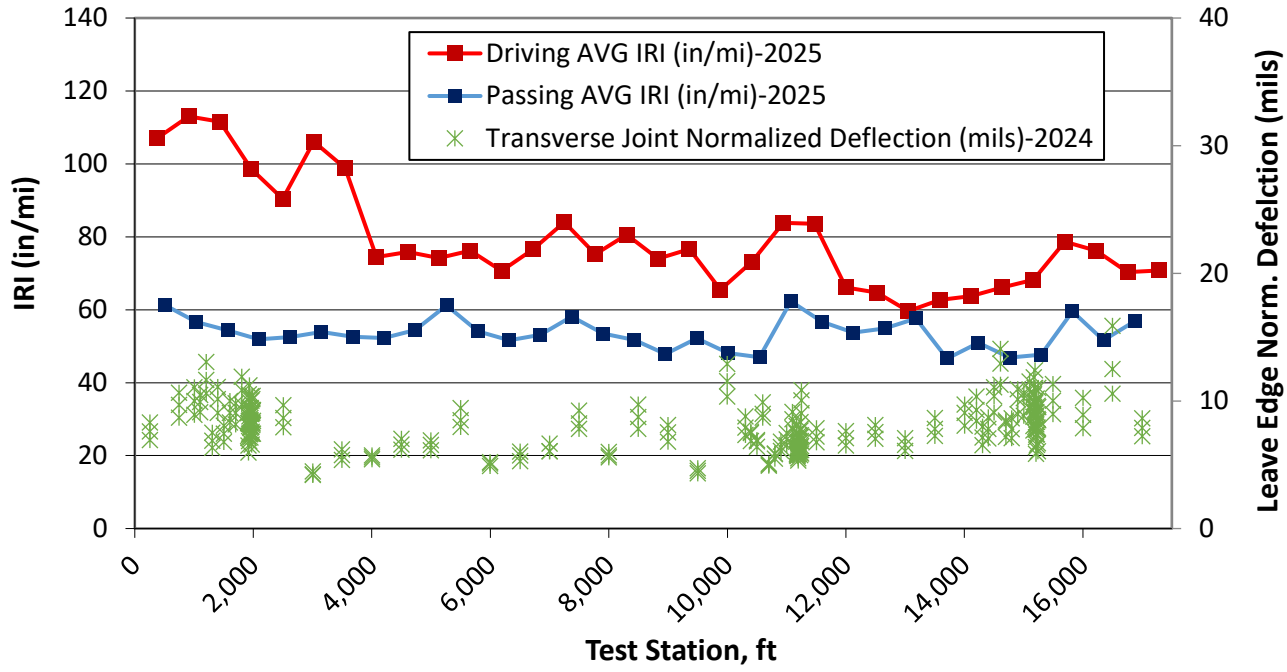

Figure 46. Graph. IRI and normalized transverse joint leave edge deflection along WB direction (spring 2025).

NONDESTRUCTIVE TESTING WITH SHEAR WAVE ULTRASOUND

Overview of Shear Wave Ultrasonic Testing

Shear wave ultrasound testing was conducted using a MIRA device to assess the interfacial contact condition between the concrete overlay and the underlying interlayer for the three projects. The MIRA device is based on low-frequency shear wave transmission and reflection, which enables imaging of internal slab features, including thickness, depth of reinforcement, and potential debonding or loss of contact at the slab-base interface. The MIRA device records shear wave signals from multiple emitting and receiving sensors that are uniformly spaced within the transducer array. This configuration enables the estimation of surface shear wave speed—an indicator of material uniformity—and the reconstruction of a cross-sectional image (B-scan) at the selected test position. For this study, attention was given to B-scans for identifying patterns that indicated either unbonded interfaces (kissing bond), adhesive bonding, partial bonding, or interlayer erosion. These features help evaluate the support condition by revealing discontinuities or weak contact zones between the overlay and its interlayer system. Poor interlayer support typically results in higher-amplitude reflections or echoes at the depth of the concrete overlay. Moreover, the interpretation of these results is influenced by the surface texture of the concrete overlay, which impacts the transducer-to-surface coupling. MIRA testing results are discussed in the subsequent section with the coring results. The following sections summarize MIRA outcomes for the overlay projects on I-72, East Grand Road, and I-57.

I-72 EB and WB

Table 22 and Table 23 list the MIRA test locations along I-72 EB and WB, respectively. These positions were selected as representative locations and locations near visual distresses. The positions were selected to evaluate potential differences in B-scan reconstructions for panels without cracks and the interlayer support condition of panels with longitudinal cracks near the approach transverse joint or faulting across the lane-shoulder joint.

Table 22. I-72 EB MIRA Test Locations

Test No.	Test ID	MIRA Name	Repetition Count	Section	Location Description	Station
1	1-(1)	I-72-EB-1-C-1-	6	1	Center	014+77
2	2-(3)	I72-EB-2-DL-3- I72-EB-2-SH-3-	DL—3 SH—3	1	Shoulder-lane	014+93
3	3-(4)	I72-EB-3-TJWC-4-	3	1	TJ with crack	015+04
4	4-(5)	I72-EB-4-TJWC10-5-	3	1	10” from TJ along crack	015+03
5	5-(7)	I72-EB-5-TJWNOC-7-	6	1	TJ without crack	015+16
6	1-(6)	I72-EB-2.1-DL-6- I72-EB-2.1-SH-6-	DL—1 SH—6	2	Shoulder-lane	082+61
7	2-(10)	I72-EB-2.2-TJWOC-10-	4	2	TJ without crack	082+66
8	1-(8)	I72-EB-3.1-SH-	SH—3	3	Shoulder-lane	144+43
9	2-(9)	I72-EB-3.2-SH- I72-EB-3.2-DL-	SH—3 DL—1	3	Shoulder-lane	144+55
10	3-(11)	I72-EB-3.3-TJWOC-	4	3	Approach TJ without crack	144+54
11	4-(2)	I72-EB-3.4-CEN-	4	3	Center	144+63
12	5-(14)	I72-EB-3.5-TJWC-	4	3	Approach TJ with crack	144+78
13	6-(12)	I72-EB-3.6-TJWC-	3	3	TJ with crack	144+72
14	7-(13)	I72-EB-3.7-10INTJWC-	3	3	10” from TJ along crack	144+71

DL = driving lane; SH = shoulder; TJ = transverse joint

Table 23. I-72 WB MIRA Test Locations

Test No.	Test ID	MIRA File Name	Repetition Count	Section	Location Description	Station
1	3.1	I72-WB-3.1-C-	4	3	Center	150+68
2	3.2	I72-WB-3.2-TJ-	4	3	TJ without crack	150+59
3	3.3	I72-WB-3.3-SH- I72-WB-3.3-DL-	SH—3 DL—3	3	Shoulder-lane	150+82
4	3.4	I72-WB-3.4-SH- I72-WB-3.4-DL-	SH—3 DL—5	3	Shoulder-lane	150+58
5	2.1	I72-WB-2.1-SH- I72-WB-2.1-DL-	SH—3 DL—3	2	Shoulder-lane	109+78
6	2.2	I72-WB-2.2-SH- I72-WB-2.2-DL-	SH—3 DL—3	2	Shoulder-lane	109+66
7	2.3	I72-WB-2.3-C-	4	2	Center	109+52
8	2.4	I72-WB-2.4-TJ-	5	2	TJ without crack	109+43

DL = driving lane; SH = shoulder; TJ = transverse joint

Figure 47 shows a representative layout of MIRA test points in a segment of I-72 EB that was selected to capture the interlayer conditions in a variety of slab locations and positions with different distresses. A total of 22 MIRA test locations were selected, 14 in the EB direction with an HMA interlayer and 8 in the WB direction with a NWGF interlayer. Test locations included a center slab in non-distressed panels, areas near transverse joints with and without longitudinal cracks, and near the lane-shoulder joints.

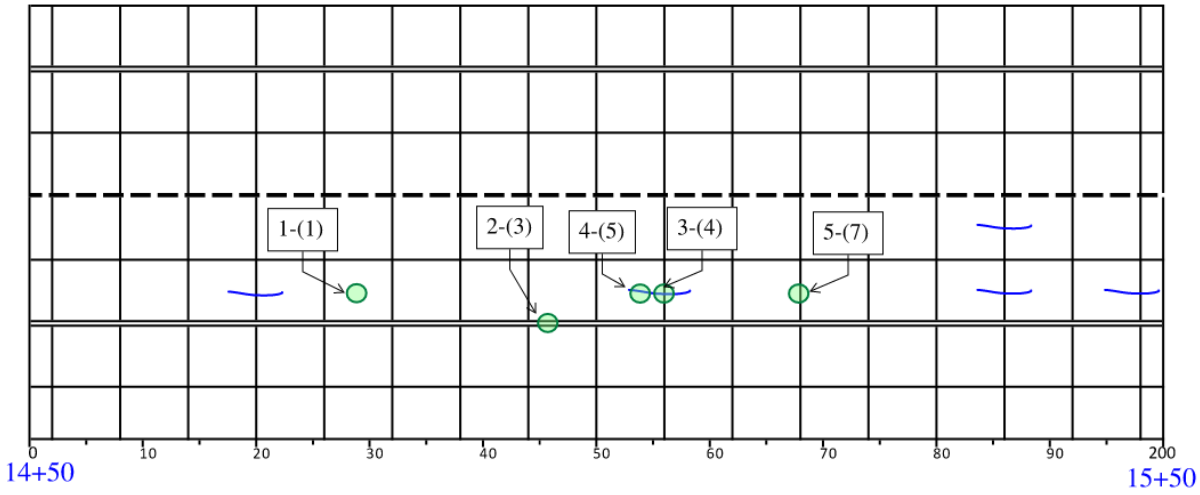

Figure 47. Illustration. Example of distribution of MIRA measurements in sound concrete slab areas and near locations selected for coring in I-72 EB. 1-(1) at the center of an uncracked overlay panel. 2-(3) parallel to lane-shoulder joint. 3-(4) parallel to transverse joint near the middle of a slab with a longitudinal crack. 4-(5) measurement 10 in. away from transverse joint near longitudinal crack and 5-(7) parallel to transverse joint near the middle of a slab.

Figure 48 provides field photographs of the MIRA device's position at various slab locations. These correspond to the different location descriptions annotated in Table 22 and Table 23. The MIRA device was positioned parallel to the joint with an offset of at least 3 in. (75 mm) to reduce boundary interference in ultrasound-based image reconstructions. A similar offset was maintained from the longitudinal cracks to ensure continuous wavefronts under the device's footprint.

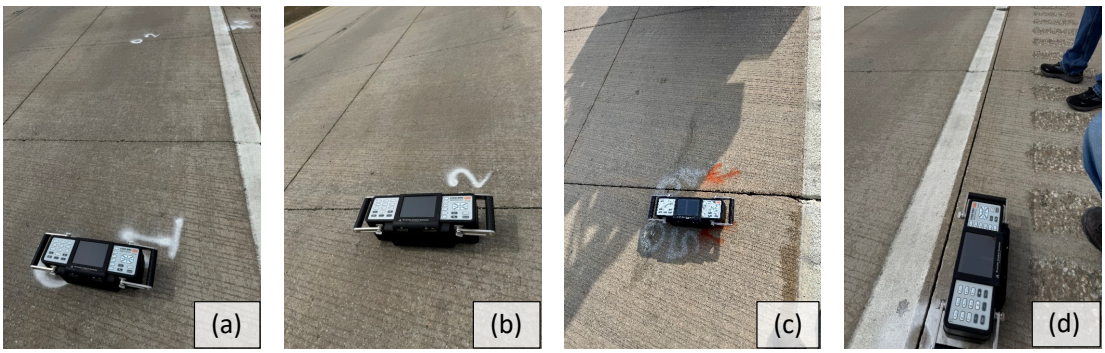

Figure 48. Photos. Positions of MIRA device at selected test locations marked for coring: (a) center, (b) near the transverse joint (TJ) on approach slab, (c) near TJ avoiding longitudinal crack on approach slab, (d) near lane-shoulder joint on the shoulder side.

Observations and Results from I-72 EB

Figure 49 shows two representative B-scan images of shear wave reflections collected at the center of uncracked panels in I-72 EB. Figure 49-a corresponds to station 14+77 and Figure 49-b to station 144+63. In both cases, the dominant thickness reflections appear around 195 mm. Dominant thickness reflection refers to the depth at which the strongest reflection region is visible in B-scans. The average estimated shear wave speed in the center of slabs was 2,605 m/s with a coefficient of variation of 5.7%. Given the expected overlay thickness of 6 in. (152 mm) and HMA interlayer thickness of 1.25 in. (32 mm), this dominant reflection depth aligns closely with the bottom of the HMA interlayer. In some cases (Figure 49-b), an additional reflection is visible near 150 mm depth, suggesting that part of the shear wave energy is being reflected at the concrete overlay-HMA interface. This may indicate partial bonding at the concrete interface and also supports the interpretation that HMA is unbonded from the underlying CRCP layer. While in other locations (see Figure 49-a), B-scans showed no traces of reflections at the concrete overlay-HMA interface. Instead, strong and consistent reflections were observed from the bottom of the HMA interlayer (top of the existing CRCP layer). This pattern suggests the overlay is well bonded to the HMA, but the HMA itself is unbonded to the underlying CRCP, likely indicating a kissing bonding at the HMA-CRCP interface.

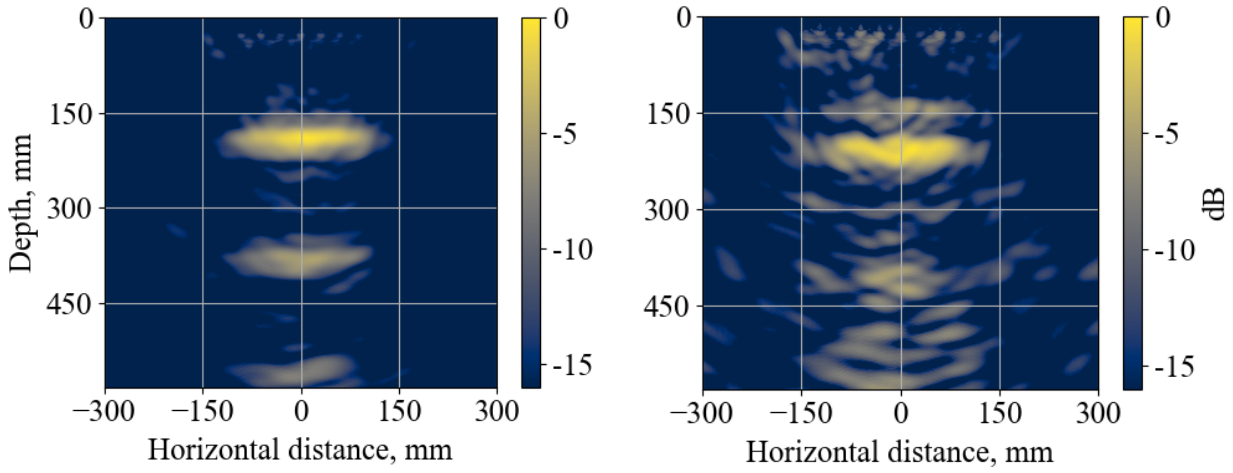

(a) Station 14+77 (b) Station 144+63

Figure 49. Graphs. Example of typical ultrasound-based cross-sectional reconstructions (B-scans) from tests in the center of slabs at (a) station 14+77 and (b) station 144+63.

Figure 50 compares B-scan reconstructions at two test locations that are parallel to the transverse joint with station 144+78 containing a visible longitudinal crack and station 82+66 without any cracking, respectively. Both cases exhibit similar reflection behavior, including a distinguishable interface near the bottom of the concrete overlay and dominant reflection from the bottom of the HMA interlayer at about 190 mm, regardless of the surface cracking. No substantial differences in reflection amplitude or continuity are observed between the two conditions, suggesting that the presence of a longitudinal crack at the surface may not always correlate with a significant loss of interfacial contact detectable by shear wave ultrasound. However, this may also indicate that deterioration begins at the bottom of the interlayer, affecting first the bond between the HMA interlayer and the existing CRCP.

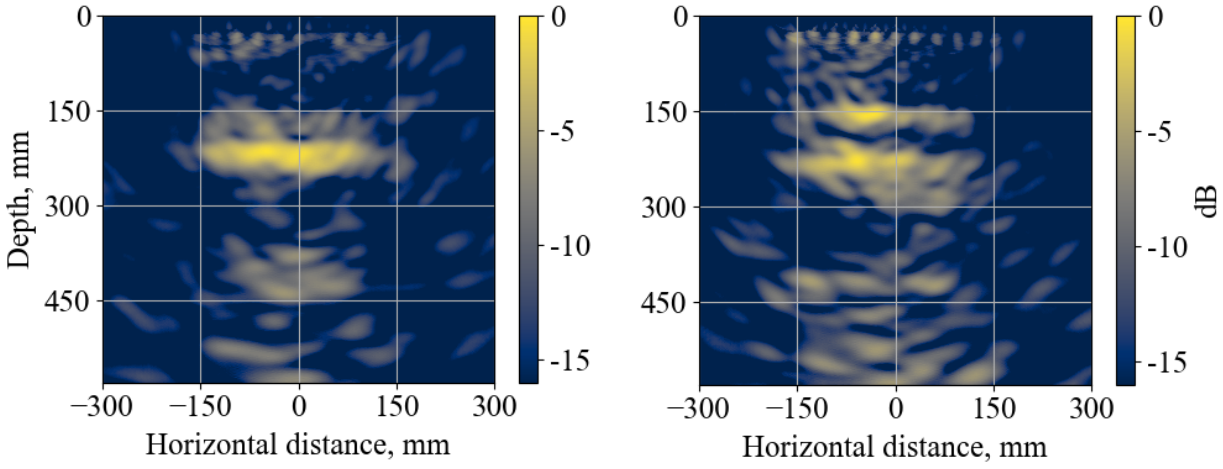

(a) Station 144+78 (b) Station 82+66

Figure 50. Graphs. Example of typical B-scans in locations near (a) transverse joint with longitudinal crack at station 144+78 and (b) transverse joint without longitudinal crack at station 82+66.

Figure 51 displays an example of the B-scan from a location more than 10 in. from a transverse joint containing a longitudinal crack. In this B-scan the dominant reflection comes from a depth around 6 in. (152 mm), but the lack of echoes from this reflection (e.g., at 304 mm and 456 mm) indicate that the overlay may be partially bonded to the HMA interlayer, which is dissipating shear wave energy in the HMA and CRCP layer.

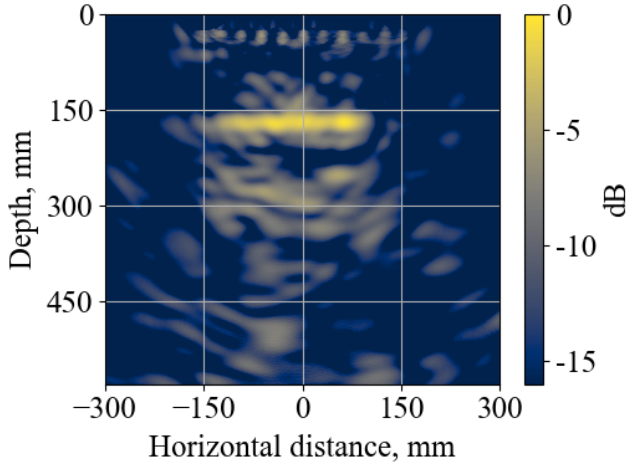

Figure 51. Graph. Example of the typical B-scan obtained 10 in. offset from a transverse joint with longitudinal crack at station 15+03.

The average shear wave speed (C_s) and dominant thickness reflection (e.g., concrete overlay to HMA or HMA to CRCP) for all locations, except near the lane-shoulder joint, are summarized in Table 24. The overall average C_s was 2,672 m/s with a standard deviation (SD) of 108 m/s and a CoV of 4.0%. The average dominant thickness reflection was 194 mm (7.65 in.), with an SD of 25 mm (1 in.) and a CoV of 12.9%, while the as-designed overlay+HMA thickness was 7.25 in. (184 mm). These estimates assume both layers have the same C_s, but the HMA is expected to have a lower C_s than the concrete

layer, which should overestimate the thickness of the overlay+HMA layer. The estimation of C_s in HMA was not determined in this study. The B-scans of the HMA interlayer showed that the dominant thickness (reflection) was at the depth of the HMA-CRCP interface.

Table 24. Summary of Estimated Shear Wave Speed (C_s) and Dominant Thickness Results for I-72 EB

Station	14+77	15+04	15+03	15+16	82+66	144+54	144+63	144+78	144+72	144+71
Position	**C**	**TJWC**	**10" TJ**	**WOC**	**WOC**	**WOC**	**C**	**TJWC**	**TJWC**	**10" TJ**
Repeats	6	3	3	6	4	4	4	4	3	3
Avg C_s, m/s	2,709	2,475	2,689	2,732	2,794	2,696	2,500	2,795	2,660	2,670
SD, m/s	99	181	101	21	12	166	171	10	152	55
CoV, %	4	7	4	1	0.4	6	7	0	6	2
Avg thickness, mm	198	199	160	200	234	213	192	205	146	196
SD, mm	7	13	6	35	16	14	15	4	10	5
CoV, %	4	7	4	18	7	7	8	2	7	3

C is slab center, WOC is for tests near a transverse joint without a longitudinal crack, and LJ-DL is for longitudinal joint between the driving lane and shoulder.

Most of the MIRA tests collected at shoulder-lane locations in I-72 WB resulted in signals with lower signal quality than in the rest of the locations, leading to unreliable C_s estimates and inadequate B-scan reconstructions. On the shoulder side, these findings were attributed to testing with the MIRA device orientated perpendicular to the transverse tining, while on the driving lane, it was mostly attributed to the thickness of the reflective lane markings. These two conditions have a direct impact in the ability of shear waves to propagate across the surface. With these conditions, the proposed approach to reconstruct B-scans at the lane-shoulder joint was to use a representative C_s from all other locations (i.e., 2,672 m/s). As observed in Figure 52-a and Figure 52-b, the B-scans obtained on either side of the lane-shoulder longitudinal joint provide limited reflection traces that differentiated interfaces corresponding to the overlay-HMA or the HMA-CRCP.

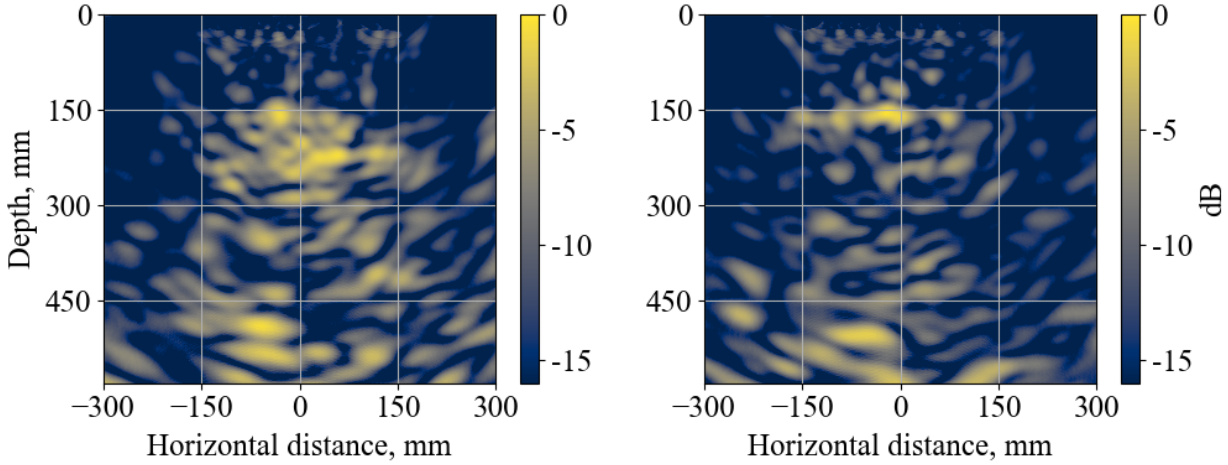

(a) Driving lane (b) Shoulder side

Figure 52. Graphs. Example of B-scans obtained parallel to the driving lane-shoulder joint at STA 14+93 on the (a) driving lane and (b) the shoulder side.

Observations and Results from I-72 WB

Figure 53 presents representative B-scan reconstructions from MIRA testing conducted on I-72 WB at the transverse joint (Figure 53-a) and at the center of an intact slab panel (Figure 53-b). In both cases, strong and well-defined reflections are observed at depths consistent with the expected overlay thickness (i.e., overlay-NWGF interface). This response was anticipated because of the NWGF interlayer system, which is designed to separate the CRCP and concrete overlay. The NWGF interface acts as a distinct acoustic boundary, producing a dominant thickness reflection at the overlay-NWGF interface. Secondary and tertiary echoes or reverberations of the original shear wave within the overlay are visible at evenly spaced depth intervals. These echoes reinforce the interpretation of a continuous unbonded interface. No additional reflections from beneath the NWGF were observed, further confirming that the wave energy is contained within the overlay layer and not interacting with any deeper pavement layers.

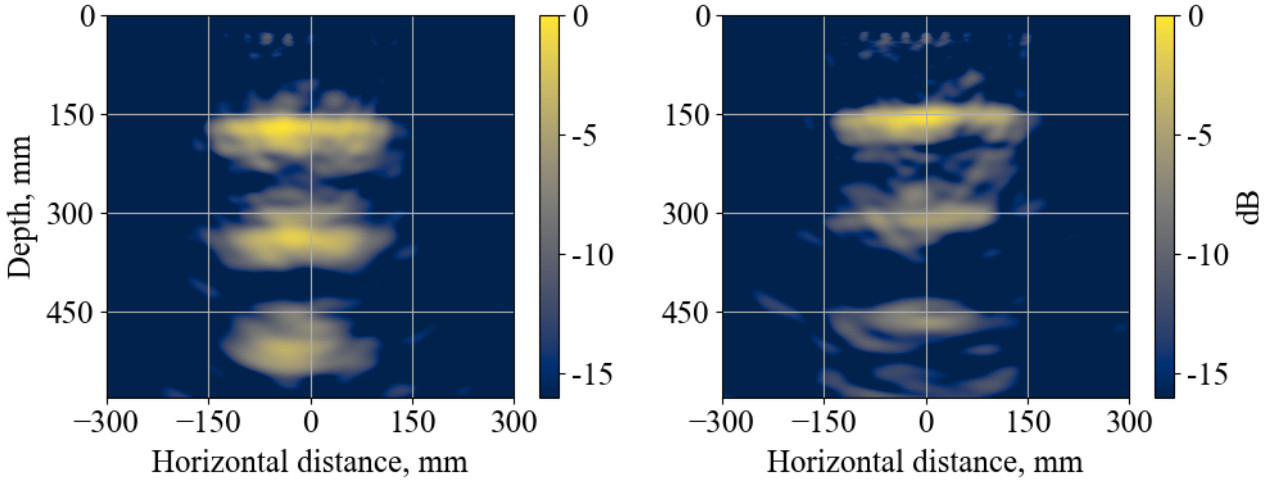

(a) Station 109+43 (b) Station 109+52

Figure 53. Graphs. Example of B-scan reconstruction in I-72 WB (a) near TJ at station 109+43 and (b) at the center of slab at station 109+52.

For most of I-72 WB, the MIRA test results collected near the driving lane-shoulder longitudinal joint also displayed low quality signals that were unusable for calculating reliable estimations of C_s. As shown in Figure 54-a, the signal at station 109+66 collected on the driving lane side of the longitudinal joint was the only one that provided clear and consistent waveforms that allowed for a reliable estimation of C_s (2,780 m/s) and reconstruction of the corresponding B-scan. In contrast, the same joint location on the shoulder side (Figure 54-b) produced a poor signal quality, likely because of surface conditions, resulting in an unreliable estimate of C_s (2,160 m/s) and an unrepresentative B-scan. In these cases, where direct estimation of C_s was not feasible, a representative C_s based on the average value from more reliable scans (as discussed in the I-72 EB section) was used for the reconstructions. This allowed for a qualitative assessment of reflection behavior while acknowledging that depth measurements in these locations may be less accurate.

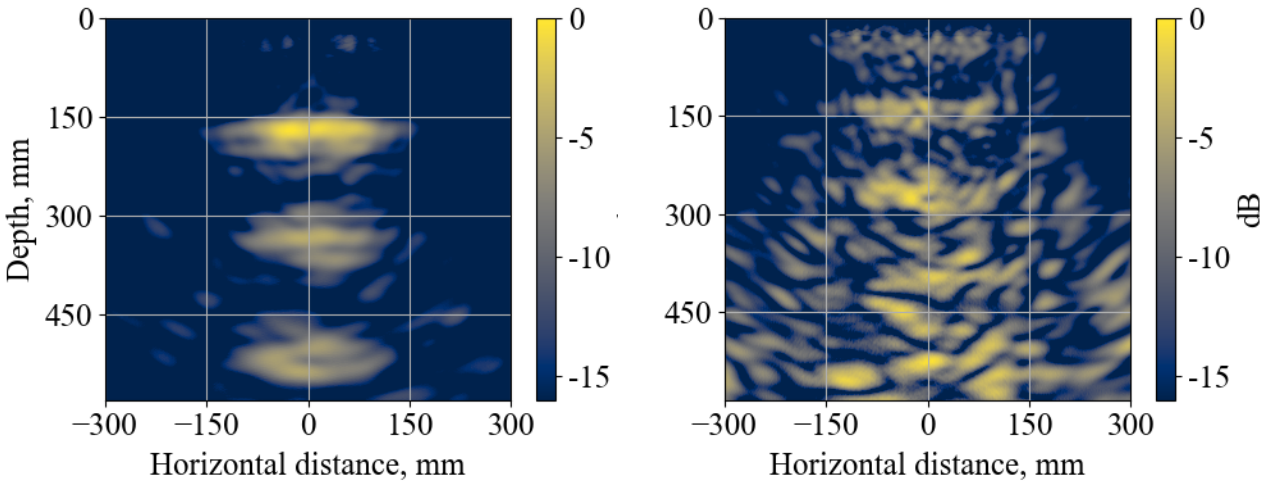

(a) Driving lane (b) Shoulder side

Figure 54. Graphs. Example of B-scan reconstructions across the lane-shoulder joint at station 109+66 (a) on driving lane side with reliable signals (estimated C_s = 2,780 m/s) and (b) on shoulder side with unreliable signals (estimated C_s = 2,160 m/s).

Figure 55 illustrates the effect of using an average C_s during the image reconstruction process. When C_s was underestimated, the resulting B-scan is distorted and does not represent actual interface depths, as seen in Figure 55-a. In contrast, Figure 55-b shows the same signals reconstructed using the average WB C_s of 2,713 m/s, resulting in a B-scan of higher quality and more distinct interfaces.

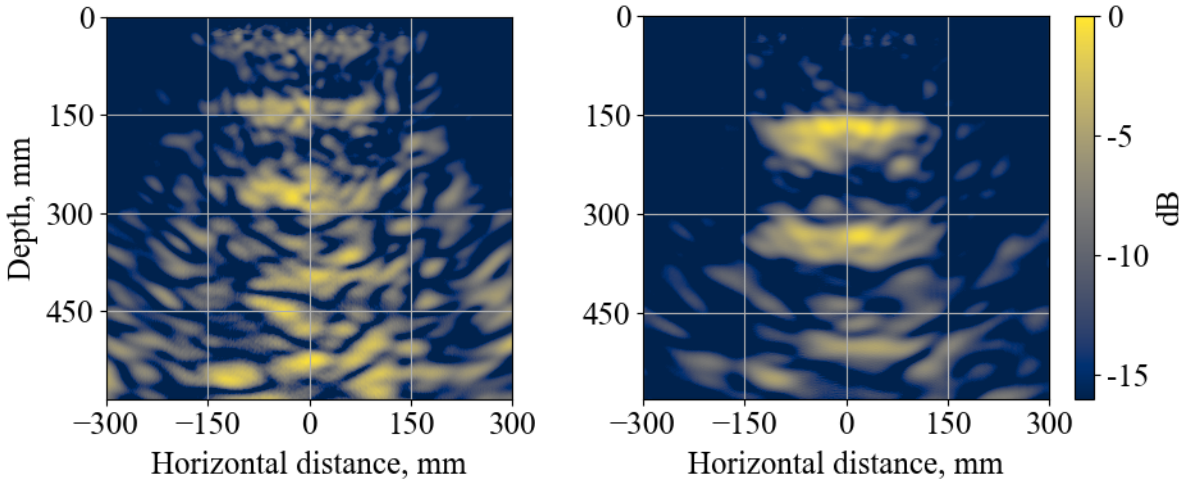

(a) Underestimated C_s (b) Average C_s

Figure 55. Graphs. Effect of C_s selection on B-scan reconstruction quality for the same signal dataset (a) using an underestimated C_s (2,160 m/s) and (b) the average C_s (2,713 m/s) for I-72 WB.

The estimated shear wave speeds (C_s) and overlay thicknesses for locations with reliable signals on I-72 WB are summarized in Table 25. The estimated C_s values were consistent across most locations and had low coefficient of variation, indicating reliable and repeatable signal quality especially at station 109+43. The overall average C_s was 2,713 m/s with a coefficient variation of 2.1% for I-72 WB.

The estimated overlay thicknesses of 6.4 in. (162 mm) with coefficient of variation of 4.1% aligned closely with the overlay design thickness of 6 in. (152 mm).

Table 25. Estimated Shear Wave Speed (C_s) and Dominant Thickness Results for I-72 WB

Station	109+52	109+43	150+68	150+59	109+66
Position	**C**	**WOC**	**C**	**WOC**	**LJ-DL**
Repeats	4	5	4	4	3
Avg C_s, m/s	2,727	2,758	2,751	2,614	2,714
SD, m/s	47	15	46	121	57
CoV, %	1.7	0.5	1.7	4.6	2.1
Avg thickness, mm	153.5	165.8	170.5	158.8	159
SD, mm	2.9	0.8	3.7	7.5	4.4
CoV, %	1.9	0.5	2.2	4.7	2.7

C is slab center, WOC is for tests near a transverse joint without a longitudinal crack, and LJ-DL is for longitudinal joint between the driving lane and shoulder.

East Grand Road (Crainville, Illinois) Testing Summary

A total of 35 MIRA scans were conducted along the EB and WB directions of East Grand Road in Crainville, Illinois, to evaluate interface conditions between the concrete overlay, HMA interlayer, and existing concrete pavement. No coring and FWD were conducted on this test section. Figure 56 presents a typical layout of selected slab positions and spatial distribution along the pavement section, which consisted of center, corner, and longitudinal edge (called curb) positions. Tested station and slab location are summarized in Table 26, and detailed information about the test locations can be found in Appendix B.

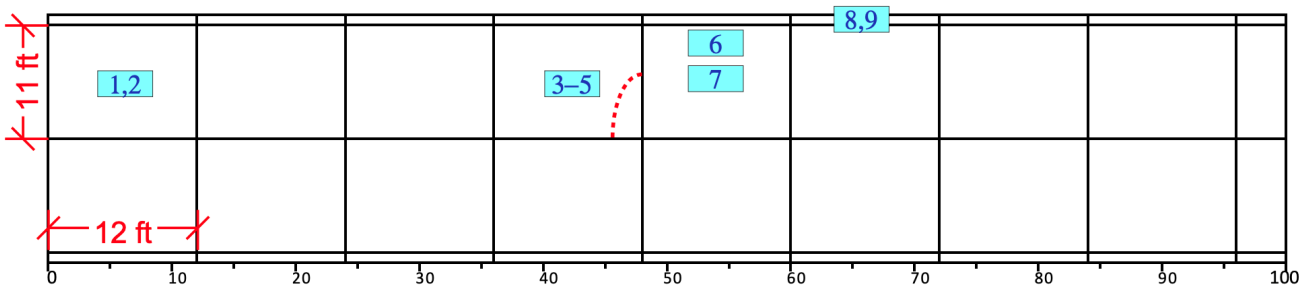

Figure 56. Illustration. Example of typical test location and identification (blue rectangles) starting from station 0+00 (EB lane) on the left end and moving westward.

Table 26. Summary of MIRA Test Locations on East Grand Road, including Station, Test Direction, and Relative Position within the Slab (Center, Corner, or Curb)

Test No.	STA	Location	Dir	Test No.	STA	Location	Dir
1	0+06	Center	EB	19	6+04	Center	EB
2	0+06	Center	EB	20	6+04	Center	EB
3	0+42	Center	EB	21	25+04	Center	EB
4	0+42	Center	EB	22	25+04	Center	EB
5	0+42	Center	EB	23	25+04	Center	EB
6	0+54	Near Curb	EB	24	25+26	Curb	EB
7	0+54	Center	EB	25	25+26	Curb	EB
8	0+66	Curb	EB	26	26+10	Center	WB
9	0+66	Curb	EB	27	27+06	Center	EB
10	0+66	Curb	EB	28	27+06	Center	EB
11	1+86	Center	EB	29	27+18	Center	EB
12	2+82	Center	EB	30	27+18	Center	EB
13	4+62	Center	EB	31	20+94	Center	WB
14	4+62	Center	EB	32	9+90	Center	WB
15	4+71	Corner	EB	33	9+90	Center	WB
16	4+71	Corner	EB	34	9+66	Center	WB
17	4+74	Curb	EB	35	7+26	Center	WB
18	6+02	Corner	EB				

Figure 57 shows representative B-scan reconstructions from the slab center and curb areas. Test no. 2 (Figure 57-a), collected near station 0+06, displays a clearly defined reflection at a depth consistent with the expected overlay thickness of 6 in. (152 mm) and minimal noise, indicating good surface coupling and likely an unbonded condition (kissing bond) at the concrete overlay-HMA interface. In contrast, test no. 6 (Figure 57-b), located near the curb edge at STA 0+54, shows a deeper dominant reflection and more irregular patterns. This can be a result of greater overlay thickness variation or, more likely, a reflection from the bottom of the HMA layer, which is thicker at the edge due to past pavement widening. Moreover, this deeper dominant reflection can be associated with the existing thicker HMA section near the curb applied for lane widening.

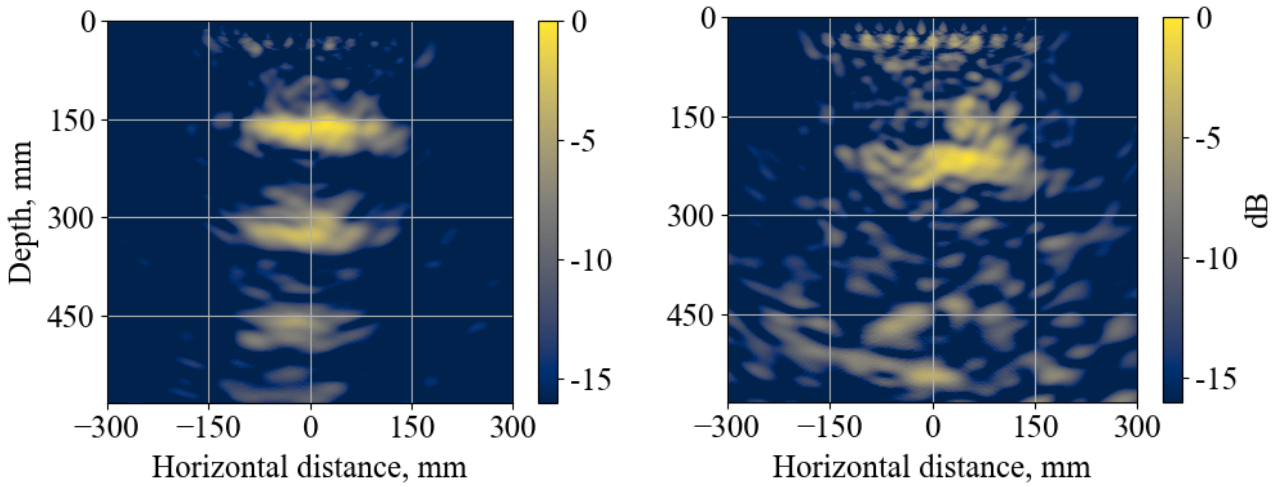

(a) Test No. 2 (b) Test No. 6

Figure 57. Graphs. Example of B-scan reconstructions in East Grand Road at (a) test no. 2 (station 0+06) in slab center with a C_s of 2,413 m/s and an overlay thickness of 6.2 in. (157 mm), (b) test no. 6 (station 0+54) near left-side curb with a C_s of 2,474 m/s and a thickness of 8.2 in. (209 mm).

Figure 58 summarized the average surface wave speed, C_s, and dominant reflection thicknesses obtained from MIRA testing throughout 35 locations on East Grand Road, grouped by slab position: center, corners, and curbs. The average estimated overlay thickness at the center locations was 7.2 in. (182.6 mm), compared to 6.0 in. (153 mm) at the curb and 5.4 in. (136 mm) near the corners. Corresponding average C_s values were 2,490, 2,399, and 2,457 m/s, respectively. Approximately 46% of the test locations produced reflection depths within ±10 mm of the expected design thickness, while the remainder showed deviations that suggest spatial variability in overlay thickness or in the bonding condition at the concrete overlay-HMA interface. This variation is consistent with the construction details shown in the typical section (Figure 5), which specifies variable-depth HMA surface removal prior to overlay placement. It is likely that slab interior regions were milled deeper, while areas near curbs and corners may have retained more of the existing HMA.

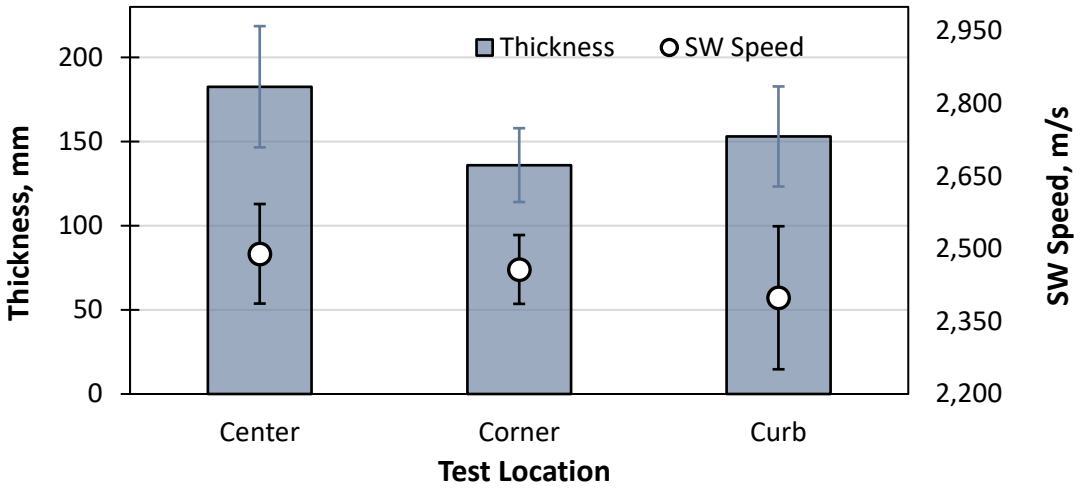

Figure 58. Chart. Average estimated thickness and surface wave speed from MIRA testing at center, corner, and curb slab locations along East Grand Road. Error bars represent one standard deviation from the mean for each location group.

I-57 (Anna, Illinois) Testing Summary

Testing on I-57 was limited because of traffic control constraints, allowing only six exploratory MIRA tests near station 276+90 in the northbound direction. The B-scan reconstructions offered a preliminary view of the concrete slab-HMA interlayer interface, but there were insufficient tests for drawing conclusions. Figure 59 shows two representative reconstructions where the estimated dominant reflection depth approximates the design concrete overlay thickness of 10 in. (254 mm). The absence of multiple echo patterns and the presence of relatively weak reflections near the expected overlay depth suggest some adhesive concrete-HMA bonding and dissipation of significant amount of energy in the HMA interlayer and existing JRCP layer.

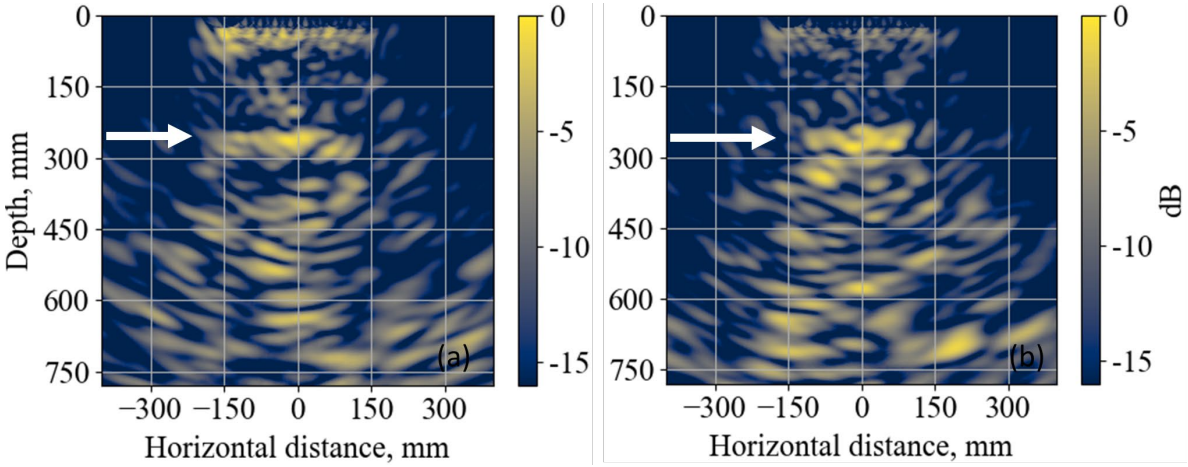

(a) Test No. 5 (b) Test No. 6

Figure 59. Graphs. Example of B-scan in I-57 northbound near station 276+90 at (a) test no. 5 and (b) test no. 6. Arrow in white indicates the depth of the overlay thickness reflection.

The shear wave speed and thickness estimates are summarized in Table 27. The average shear wave speed (C_s) across the six tests was 2,811 m/s with a standard deviation of 118.5 m/s, resulting in a coefficient of variation (COV) of 4.2%. This low variation suggests relatively consistent material quality and transducer coupling across the test areas.

This UBOL section had a design thickness of 9.75 in. (248 mm) with a 3.25 in. dense-graded HMA interlayer on an existing 10 in. JRCP. This adds to a composite UBOL thickness of 13 in. (330 mm) if the overlay is bonded to the HMA interlayer. Moreover, the top 1.25 in. of the HMA interlayer is new material and the bottom 2 in. is the existing HMA overlay. From the MIRA results, the dominant reflection depths averaged 11.7 in. with a COV of 20.5%, suggesting variability in the overlay thickness or changes in the interface condition, such as localized areas with a bonded overlay-HMA interface or unbonded HMA-JRCP interface. Therefore, tests 3–6 are likely on areas where the overlay is unbonded from the HMA interlayer, while tests 1 and 2 are likely concrete-HMA bonded. On concrete-HMA sections, the MIRA thickness estimates are likely to overestimate thickness due to the differences in wave propagation speed in both materials. While these results offer useful insights in a localized section, broader testing or direct verification (e.g., cores) is needed to confirm interlayer thickness and contact condition in order to validate these interpretations.

Table 27. Summary of Estimated Shear Wave Speeds (C_s) and Estimated Thicknesses from MIRA Tests on I-57 Northbound at Station 276+90

Test No.	C_s, m/s	Estimated Thickness, in. (mm)
1	2,848	14.0 (355)
2	2,800	15.4 (390)
3	2,584	10.5 (267)
4	2,911	9.7 (247)
5	2,891	9.9 (252)
6	2,835	10.4 (265)
Ave.	2,811	11.7 (296)
SD	118.5	2.4 (60.8)
COV	4.2%	20.5

MIRA Field Test Summary

Table 28 provides a consolidated overview of MIRA testing outcomes from the three overlay projects, summarizing the number of test locations, interlayer types, and general observations on overlay-to-interlayer scenarios. For example, tests on I-72 WB with a NWGF interlayer resulted in clear reflections from the overlay bottom, suggesting a mostly unbonded interface. In contrast, tests on I-72 EB, with an HMA interlayer, had more variable responses. Some locations showed reflection at the bottom of the HMA interlayer, indicating bonding of the concrete overlay and HMA and likely a kissing-bond condition at the HMA-to-CRCP interface. The East Grand Road section exhibited variable thickness reflection across slab positions, which may suggest variable overlay-HMA bonding in

localized areas. Testing on I-57 NB was limited to a spot-check in a single area and showed uncertain bonding conditions due to variation in thickness reflections and absence of corroborating FWD or core data.

Table 28. Summary of MIRA Test Observations across Overlay Projects

Project	Test Loc.	IL Type	Observed Interface Condition
I-72 EB	14	HMA	Mixed interface conditions observed. Several slabs showed reflection from the bottom of the HMA interlayer, suggesting partial adhesive bond between overlay and HMA and likely a kissing-bond at the HMA-to-CRCP interface. Dataset included FWD and cores.
I-72 WB	8	NWGF	High-amplitude reflection and evenly spaced backwall echoes indicate unbonded (kissing-bond) interface between the FRC overlay and the NWGF interlayer. Full dataset included FWD and cores.
East Grand Road	22	HMA	Mixed bonding conditions observed with localized variation in reflection depths, which suggests partial adhesive bonding or thicknesses differences at specific locations, possibly due to uneven HMA removal. No FWD or cores available.
I-57 NB	1	HMA	Single location. Reflection depths varied, suggesting possible localized areas with adhesive bonding and others with kissing bond (unbonded). No FWD or cores available; further assessment recommended.

IL= interlayer

CORING

Coring was conducted to complement the distress surveys, FWD, and MIRA testing on I-72. Core analysis allowed for measurement of overlay and interlayer thicknesses, identification of interface conditions, and to assess crack depth that may not have been fully evident from distress surveys or MIRA B-scan reconstructions alone. All cores were taken from I-72 EB and WB at locations selected based on prior MIRA data collection (Table 22 and Table 23) and included a range of slab positions such as slab center, transverse joints (with and without longitudinal cracks), and driving lane-shoulder longitudinal joint. The detailed I-72 map including the core locations can be found in Appendix A, which includes the crack mapping from the distress survey.

Core Marking and Extraction

Coring areas were outlined with white spray paint, and reference numbers were added to ensure trackability. Figure 60 displays different locations marked for coring, including a core location in the center of a slab (Figure 60-a), over the transverse joint on a longitudinal crack, 10 in. from the same transverse joint (Figure 60-b) and over the driving lane-shoulder longitudinal joint (Figure 60-c).

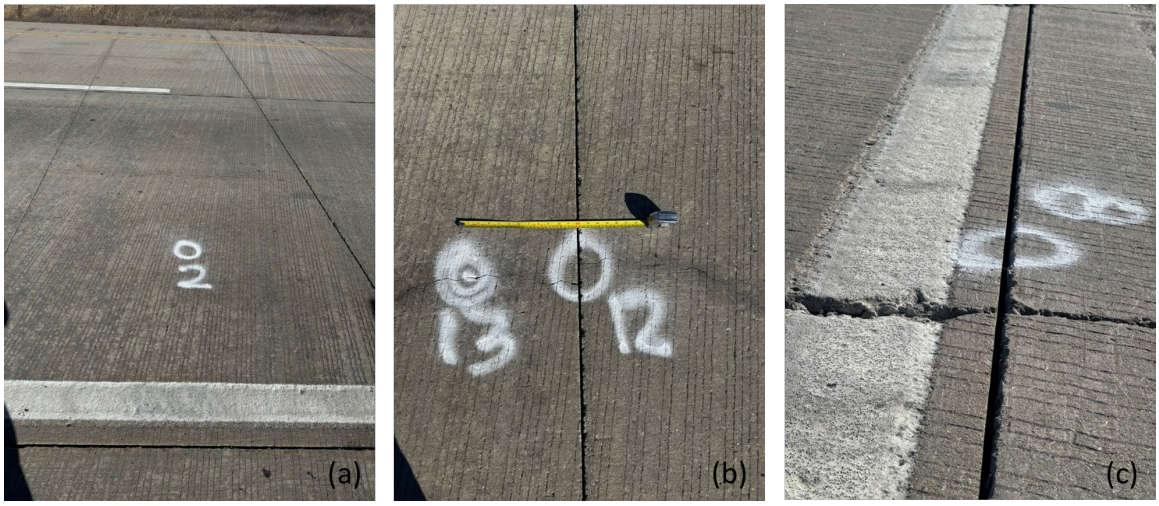

Figure 60. Photos. Example of core location markings at (a) slab center, (b) transverse joint with a longitudinal crack, and (c) over the driving lane-shoulder joint.

Coring was carried out using a trailer-mounted coring rig, as observed in Figure 61-a, that did not require installing in situ anchors. Once each core was extracted, a visual inspection of the borehole was completed to document any cracks, voids, joint activation, or potential bonding failure along the interlayer (Figure 61-b and Figure 61-c). Each core was labeled, photographed, and stored in sealed plastic bags for later analysis of thickness and concrete-HMA interlayer bonding condition in a laboratory.

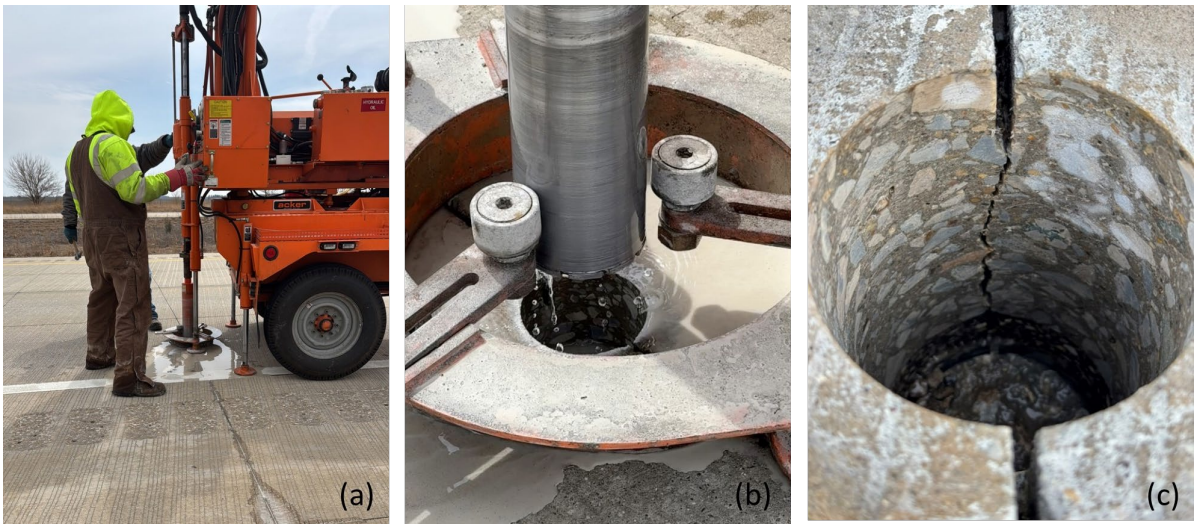

Figure 61. Photo. Core extraction at the middle of a transverse joint showing (a) coring rig operation, (b) borehole after core removal, and (c) inspection of borehole for joint activation.

Observations from I-72 EB Core Samples

A total of 14 cores were extracted from the I-72 EB overlay section at different slab positions. Representative core samples from I-72 EB are shown in Figure 62–Figure 66, including slab center,

transverse joint with a longitudinal crack, and driving lane-shoulder longitudinal joint. The results of the coring showed 13 out of 14 met the minimum design of 6 in. with an overall average of 6.26 in. The two cores extracted from the EB direction at the slab center displayed a fully bonded condition with the HMA interlayer without signs of degradation in the HMA layer, as seen in Figure 62.

Figure 62. Photo. Side and top view of cores extracted from slab centers.

Two of the three cores extracted over transverse joints with longitudinal cracks were adhesively bonded to the HMA layers (i.e., no visible degradation), and the longitudinal crack visually propagated from 2 to 3 in. deep, as shown in Figure 63-a. Two of the three cores had an activated transverse joint extending full depth (Figure 63). However, only one of these cores (Figure 63-b) had an observable longitudinal crack that also propagated the full depth of the concrete overlay and was completely unbonded from the HMA interlayer. This unbonded HMA interlayer displayed degradation likely due to erosion. The third core, in which the transverse joint did not activate, can be found in Appendix C.

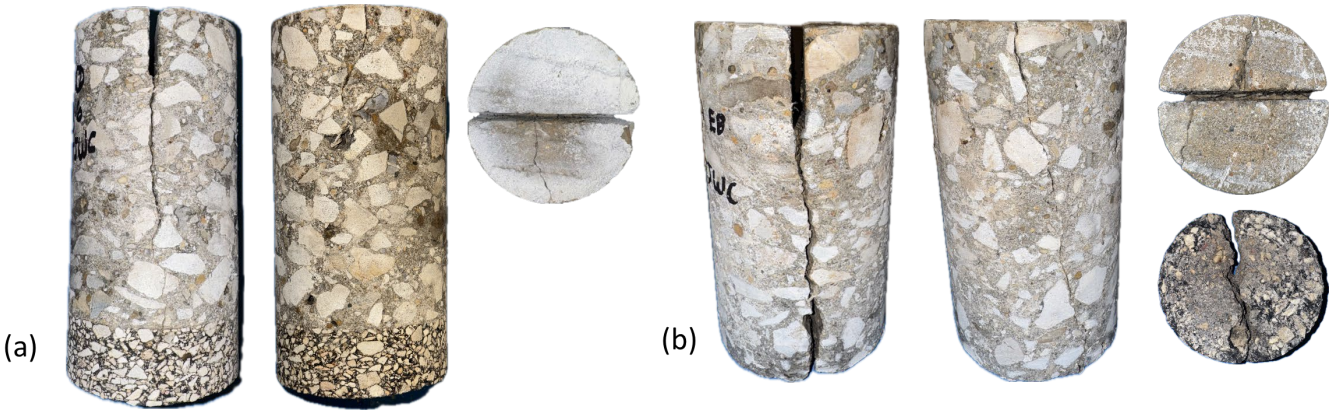

Figure 63. Photo. Examples of cores from transverse joints with longitudinal cracking. (a) Complete joint activation and partial longitudinal crack activation with bonded HMA layer. (b) Core with full-depth activation of both the longitudinal crack and joint but completely unbonded from the HMA interlayer. Each core is shown in front view (aligned with the transverse joint), side view (aligned with the longitudinal crack), top view, and bottom view (included only when interlayer was unbonded).

The three cores extracted from transverse joints without longitudinal cracks all showed full-depth joint activation, as observed in Figure 64. Two of these cores were fully bonded to the HMA interlayer (Figure 64-a and Figure 64-c), and one was unbonded (Figure 64-b). Therefore, joint activation or HMA debonding is not sufficient for longitudinal crack initiation, but these characteristics all occur for cores with longitudinal cracking. For example, the HMA layer fractured through the activated transverse joint, as seen in Figure 64-b, and the joint widens at the bottom of the overlay and shows some degradation at the concrete overlay-HMA interface. Longitudinal cracking may likely initiate eventually under these conditions.

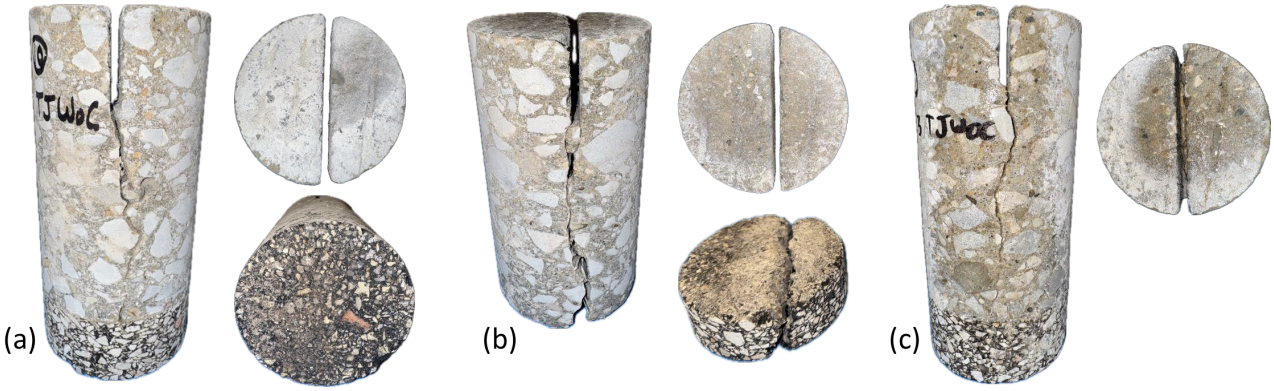

Figure 64. Photo. Cores extracted from transverse joint without longitudinal cracking (a,c). Cores with full-depth joint activation and bonded HMA interlayer. (b) Core with full-depth joint activation and unbonded HMA interlayer, showing degradation at the concrete overlay-HMA interface near the joint. Images include front view (aligned with joint), top view, and bottom view when applicable.

Figure 65 displays two cores extracted 254 mm (10 in.) from transverse joints along a longitudinal crack path. Both concrete overlay cores were fully bonded to the HMA interlayer, and the longitudinal cracks propagated only 1–1.5 in. deep. These observations suggest that bonding at the HMA interlayer may be preserved when a crack has not activated full depth and degraded significantly (i.e., widened enough to disrupt the bond). The observation could also suggest that debonding in these cores is taking place first at the HMA-CRCP interface, as seen in Figure 65-b.

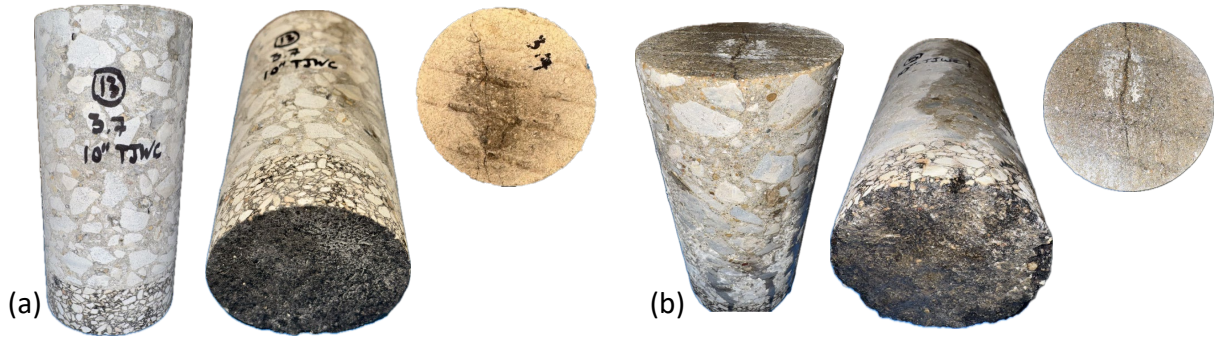

Figure 65. Photo. Cores extracted 10 in. from transverse joint along longitudinal crack path. (a) Cores showed full bonding to the HMA interlayer with crack depths between 1 and 1.5 in. at station 144+71 and (b) and at station 15+03.

The four cores extracted from the driving lane-shoulder had completely activated longitudinal joints and showed severe degradation in the HMA interlayer. The remaining HMA was nearly absent, and such degradation was generally more severe on the shoulder side of the core than on the driving lane side (see Figure 66). The concrete portion of these cores was completely split or remained held together by only a few fibers, as shown in Figure 66. The order of degradation is not clear, but the lane-shoulder joint is wide, low LTE exists, the macrofibers are no longer effective, there is 0.25 in. faulting present, and the HMA interlayer has significantly eroded.

Figure 66. Photo. Example of cores extracted from driving lane-shoulder longitudinal joints showing full-depth joint activation and an advanced HMA interlayer degradation. (a) Core split along longitudinal joint. (b) Core that remained held together by only a few macrofibers.

As summarized in Table 29, the 14 cores were grouped into three groups: five cores between station 10+00 and station 20+00, two cores between 74+15 and 84+15, and seven cores between 142+50 and 152+50. The average core overlay length for each group were 6.59 in., 6.16 in., and 6.05 in., respectively, with COV lower than 1% in all groups. The average thickness of the HMA layer for each group was 1.14 in., 1.55 in., and 1.46 in., respectively. In the EB, the concrete overlay design thickness was met by 93% of the cores, and the HMA interlayer design thickness by 70% of the cores where the interlayer displayed little to no degradation. Additional observations for each individual core can be found in Appendix C.

Table 29. Summary of Overlay and HMA Layer Thickness Measurements for Cores Extracted from I-72 EB

Test. No.	Station	Location	Overlay thickness, in.	Diameter, in.	HMA thickness, in.
1	14+77	1.1 Center	6.49	3.70	1.11
2	14+93	2-3 SH/DL	6.62	3.69	1.00*
3	15+04	1.3 TJWC	6.61	3.70	1.13
4	15+03	1.4 10”-TJWC	6.59	3.71	1.05
5	15+16	1.5 TJWOC	6.64	3.70	1.25
6	82+61	2.1 SH/DL	6.17	3.67	0.43*
7	82+66	2.2 TJWOC	6.15	3.71	1.55

Test. No.	Station	Location	Overlay thickness, in.	Diameter, in.	HMA thickness, in.
8	144+43	3.1 SH/DL	6.11	3.64	0.31*
9	144+55	3.2 SH/DL	6.03	3.61	0.36*
10	144+54	3.3 TJWOC	6.05	3.70	1.64
11	144+63	3.4 Center	5.97	3.70	1.57
12	144+78	3.5 TJWC	6.07	3.69	1.43
13	144+72	3.6 TJWC	6.06	3.70	1.33
14	144+71	3.7 10”-TJWC	6.06	3.71	1.34
		Ave. / COV	6.26 / 4.2%	3.69 / 0.8%	1.11 / 40%

*Refers to a HMA thickness measurement where this layer presented observable degradation.

SH/DL: Shoulder driving lane; TJWC: Transverse joint with longitudinal crack; TJWOC: Transverse joint without longitudinal crack.

Observations from I-72 Westbound Core Samples

A total of eight cores were taken from the I-72 WB overlay section, covering slab center, transverse joints, and driving lane-shoulder longitudinal joint locations. Representative samples are shown in Figure 67. The extracted cores from the WB had an average thickness of 6.59 in. with all cores meeting the minimum design of 6 in. Only a single core had the NWGF layer still adhered to the concrete overlay (Figure 67-a) after extraction from a slab center. The two cores taken from transverse joints exhibited full-depth joint activation and showed a more pronounced degradation (i.e., wider crack) of the bottom of the core (Figure 67-b). The four cores extracted from driving lane-shoulder joints had the NWGF unbonded (separated), and the joints were activated full-depth with a significant degradation near the core bottom, as seen in Figure 67-c. Additionally, cores from the driving lane-shoulder joint had a higher elevation on the shoulder than the driving lane, and the degradation along the joint crack path seems to follow an upward movement of the shoulder. In some of these cases, the concrete remained together only by a few bridging macrofibers. The wider joint opening reduced the impact of fiber reinforcement across this contraction joint, which was seen in the low LTE across the lane shoulder (average of 24%).

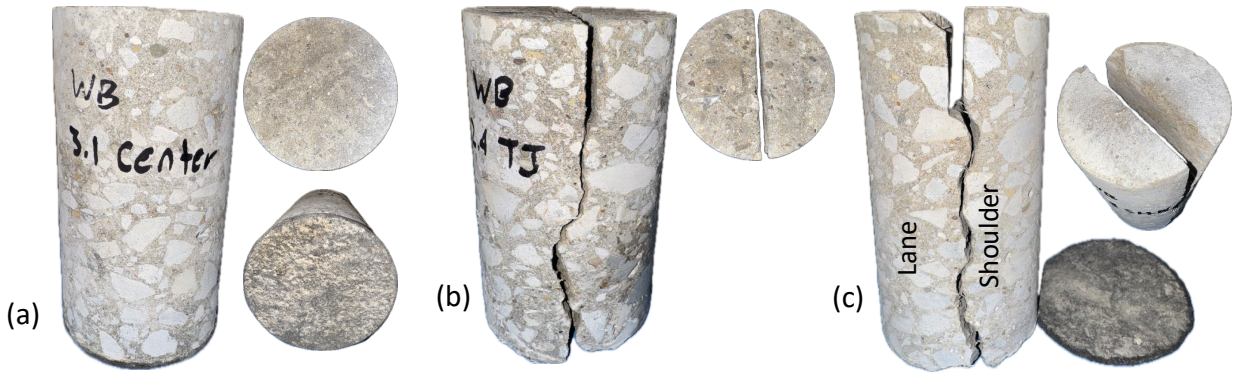

Figure 67. Photo. Examples of cores extracted on I-72 WB at (a) slab center, (b) transverse joint without longitudinal crack, and (c) driving lane-shoulder joint. Each image includes front view (aligned with joint where applicable), top view, and a view of the NWGF as available.

Table 30 summarizes the concrete overlay and NWGF thickness of the eight cores taken in I-72 WB. Four cores were taken (i.e., one at a slab center, one at a transverse joint, and two at lane-shoulder joints) in a segment between stations 152+50 to 142+50. Similar four cores were taken in another segment between stations 112+50 and 102+50. The average overlay core thickness for each group were 6.36 in. and 6.81 in. with COV of 3% and 4%, respectively. The concrete overlay design thickness was met by all cores. The NWGF had an average of 0.122 in. with a COV of 16.8%, while its design thickness was 0.125 in. In general, the NWGF was unbonded from the concrete, which suggests it properly works as an interlayer system that prevents adhesive bonding. Additional observation for each individual core can be found in Appendix B.

Table 30. Summary of Overlay and NWGF Thickness Measurements for Cores Extracted from I-72 WB

Test No.	Station	Location	Overlay thickness, in.	Diameter, in.	NWGF thickness, in.
1	150+68	2.1 SH/DL	6.19	3.69	0.15
2	150+59	2.2 SH/DL	6.55	3.68	0.11
3	150+82	2.3 Center	6.21	3.70	0.10
4	150+58	2.4 TJ	6.50	3.70	0.13
5	109+78	3.1 Center	6.85	3.70	0.09
6	109+66	3.2 TJ	6.85	3.71	0.14
7	109+52	3.3 SH/DL	6.45	3.68	0.12
8	109+43	3.4 SH/DL	7.11	3.66	0.15
		Ave. / COV	6.59 / 4.9%	3.69 / 0.5%	0.122 / 17%

CHAPTER 6: SUMMARY AND CONCLUSIONS

This field research study conducted visual distress surveys, nondestructive testing, and core extraction on the following three unbonded concrete overlay (UBOL) sections of JPCP in Illinois: I-72 near Riverton, East Grand Road in Crainville, and I-57 near Anna. The primary goal was to assess their current performance through surface distresses (e.g., cracking), structural and functional responses, cores, and shear wave assessment of the interlayer contact condition.

A literature review of recent UBOL studies in Iowa concluded long-term positive performance of UBOL projects. Several UBOL studies reported the initiation of longitudinal cracks at the transverse joint because of localized fatigue, stripping, erosion, or consolidation in the HMA interlayer. Recent updates to mechanistic-empirical UBOL design frameworks now reflect differences in the interlayer types, whether they are asphalt or geotextile fabrics, and incorporate critical stress calculations and erosion thresholds.

Overall, the three UBOLs with JPCP are performing well and should provide the intended design lives. The three UBOLs have very different traffic levels. I-57 is an interstate with high truck volume, I-72 is an interstate with medium truck volume, and East Grand Road (Crainville) is a local road with very few trucks. Although all are classified as UBOL, they have different slab geometries and structural support systems that make them distinct sections.

The I-72 UBOL, with 6 in. thickness and 6 ft by 6 ft panel size, near Riverton has a dense-graded HMA interlayer in the EB and a nonwoven geotextile fabric (NWGF) interlayer in the WB. Longitudinal cracking was observed in the EB driving lane in the wheel paths and emanating from the transverse joints. This cracking has occurred in 3.8% of the EB driving lane panels as of April 2025. Within three 1,000 ft long segments in the EB, this cracking increased from 6.3% of panels in the driving lane in 2020 to 7.0% in 2025. Currently, the longitudinal cracking is neither showing signs of significant increases nor accelerating the severity magnitude. No longitudinal cracking was found in the WB section. Corner spalling was seen more frequently in the WB section, with 1.1% of the driving lane panels in the WB exhibiting corner spalling. This spalling was attributed to insufficient full-width sawcutting of the transverse joints. Faulting of about 0.25 in. was consistently present along the driving lane-shoulder joint in both directions, with the shoulder edge having a higher elevation than the driving lane. FWD results indicated lower deflections in the EB than in the WB despite the longitudinal cracking occurring in the EB direction only. The 2024 back-calculated effective k-values of the support were 376 and 306 psi/in. for EB and WB, respectively, which have not significantly changed with time. The LTE across the transverse and lane-shoulder joints has decreased over time in both directions, with the WB lane-shoulder joint currently having an LTE of 24.4%. The 2025 average IRI values were 53 and 67 in./mi in the EB and WB, respectively, with WB values greater especially at the beginning of the section in the driving lane, which can be related to the original post-construction IRI. The 2025 IRI increased 8% in the EB and 20% in the WB relative to IRI values from 2021.

For the EB, the MIRA results suggest that an adhesive bond exists between the overlay and HMA interlayer while the HMA-CRCP interface has a kissing bond at most test locations. In the WB, an unbonded response exists (similar to a kissing bond response) between the JPCP overlay and the

existing CRCP with the NWGF acting effectively as an unbonded separation layer. The measured surface wave speeds (2,672 in EB and 2,713 m/s in WB) were relatively high in both directions, suggesting a consistent quality of the concrete overlay surface. The concrete cores confirmed stronger HMA interlayer bonding in the EB section, consistent with MIRA results, while WB cores showed consistent debonding at the NWGF interface.

The coring results from the I-72 EB and WB sections suggest the development of longitudinal cracking and faulting has the following components, which are not necessarily in order: (1) full-depth joint activation (transverse or longitudinal), (2) widening of the joint, (3) presence of water especially at the concrete-HMA interface, (4) erosion/pumping under repeated traffic loading, and (5) progressive deterioration at the bottom of the concrete overlay such as HMA stripping or movement of debris under the shoulder. Greater deterioration at the HMA interlayer was observed where full-depth joint cracks were wide, particularly at the lane-shoulder joints. Cores extracted at this location showed significant HMA interlayer erosion and stripping. Similarly, WB cores showed lane-shoulder joint widening and deterioration near the bottom of the concrete overlay, which has led to faulting across this longitudinal joint.

The East Grand Road 6 in. UBOL with 11 ft by 12 ft slabs in Crainville is performing well after nine years of service and very low truck traffic. A distress survey of the section determined 1.75% of the slabs exhibit some type of distress (cracking, spalling, joint raveling) but most of these distresses appeared within a year after construction. MIRA results on East Grand Road indicated an average surface wave speed of approximately 2,450 m/s, and 46% of the tests indicated reflection depths within 10 mm of the design thickness. Test results with deeper reflections suggested an adhesive bond at the concrete overlay-HMA interface. MIRA results suggest that the concrete overlay was thicker near the center than near the corners and edges.

The 9.75 in. UBOL on I-57 northbound near Anna did not exhibit surface distresses in the visual survey areas. Limited MIRA testing on I-57 showed no indication of concrete-HMA interface degradation. The average concrete surface wave speed was 2,811 m/s in I-57.

CHAPTER 7: RECOMMENDATIONS

UBOLs have shown satisfactory performance as a rehabilitation or replacement alternative for pavements reaching the end of their service life. However, opportunities for improvement remain, particularly regarding tie bar installation, surface preparation—before overlay placement—and drainage design. The following recommendations address these aspects in detail:

- Install steel tie bars across lane-shoulder longitudinal joints especially for thin UBOLs to maintain small joint widths, improve LTE, and limit faulting, regardless of the interlayer system. Macrofiber reinforcement alone was insufficient for controlling joint movement and limiting lane-shoulder faulting. Additionally, providing tie bars at lane-shoulder longitudinal joints could reduce erosion and stripping at or in the HMA interlayer. Tie bars do not need to be installed at the sawn longitudinal contraction joints located in the mid-lane driving or passing lane (i.e., at 6 ft offset from lane boundaries).

- The NWGF interlayer system is performing well in terms of distress development but may lead to higher IRI initially depending on the existing (longitudinal) lane profile prior to placing the concrete overlay. Pre-overlay surface preparation procedures should be reviewed to ensure the support layer is as close to the correct elevation as possible before placing the concrete overlay.

- Longitudinal cracking has developed on thin concrete overlays with an HMA interlayer as a combination of presence of water, repeated truck loading, and activated and wide concrete contraction joints. This distress development can be addressed through several key contributing factors, such as joint details, minimizing water infiltration into the joints, or conveying infiltrated water out of the pavement structure.

REFERENCES

Alland, K., Vandenbossche, J., Sachs, S., Desantis, J., Burnham, T., & Khazanovich, L. (2016). Failure Modes in Unbonded Concrete Overlays. 11th International Conference on Concrete Pavements.

Cackler, T. (2017). *Performance assessment of nonwoven geotextile materials used as separation layer for unbonded concrete overlay of existing concrete pavement applications in the U.S*. CP Road Map Brief December 2017. https://www.intrans.iastate.edu/wp-content/uploads/2018/10/MAPbriefDec2017.pdf

Caicedo, B., & Caro, S. (2023). Evaluation of the susceptibility to erosion of materials used as a base of rigid pavements using a vertical shaking table. *International Journal of Pavement Engineering*, *24*(1), 2225118. https://doi.org/10.1080/10298436.2023.2225118

Covarrubias, J. P., Binder, C., Rio, P. Del, & Fernández, M. (2023). Estado de Pavimentos Construidos con Losas de Geometría Optimizada Proyectos Públicos MOP Chile: Informe No. 1.

DeSantis, J., & Roesler, J. (2022a). *Longitudinal cracking investigation on I-72 experimental unbonded concrete overlay* (Report No. FHWA-ICT-22-002). Illinois Center for Transportation. https://doi.org/10.36501/0197-9191/22-002

DeSantis, J., & Roesler, J. (2022b). *Performance evaluation of stabilized support layers for concrete pavements* (Report No. FHWA-ICT-22-003). Illinois Center for Transportation. https://doi.org/10.36501/0197-9191/22-003

DeSantis, J., & Roesler, J. (2024). Erosion potential of stabilized support layers for concrete pavements and overlays. *Transportation Research Record*, *2678*(11). https://doi.org/10.1177/03611981241242774

Fick, G., Gross, J., Snyder, M., Harrington, D., Roesler, J., & Cackler, T. (2021). *Guide to concrete overlays*. 4th edition. https://www.intrans.iastate.edu/wp-content/uploads/2021/11/guide_to_concrete_overlays_4th_Ed_web.pdf

Hanson, T. (2023). *Interstate and primary PCC pavement overlays review* (Report No. MLR-23-01). Iowa Department of Transportation.

Harrington, D., DeGraaf D., Riley, R., Rasmussen, R., Grove, J., & Mack, J. (2007). *Guide to concrete overlay solutions*. National Center for Concrete Pavement Technology. https://www.concreteparking.org/downloads/guide_concrete_overlays.pdf

Harrington, D., & Fick, G. (2014). *Guide to concrete overlays: Sustainable solutions for resurfacing and rehabilitating existing pavements* (3rd edition) (M. Brink, Ed.). https://doi.org/10.13140/RG.2.1.3106.4724

Heckel, L., & Wienrank, C. (2018). Performance of concrete overlays on Illinois interstates, 1967 through 2016. *Transportation Research Record*, *2672*(40), 282–290. https://doi.org/10.1177/0361198118781146

Illinois Department of Transportation. (2022). *Standard Specifications for Road and Bridge Construction: Vol. Updated in 2021*. Illinois Department of Transportation.

Illinois Department of Transportation. (2025a). *Bureau of Design and Environment Manual:* Revised March 2025. Illinois Department of Transportation Bureau of Design and Environment. https://public.powerdms.com/IDOT/documents/1881647

Illinois Department of Transportation. (2025b). IROADS. https://webapps.dot.illinois.gov/IROADS/

Illinois Department of Transportation. (2025c). Special Provisions for Reclaimed Asphalt Pavement and Reclaimed Asphalt Shingles (BDE). Bureau of Design and Environment. https://public.powerdms.com/IDOT/documents/3130663

Khazanovich, L., Vandenbossche, J., DeSantis, J., & Sachs, S. (2020). *Development of an improved design procedure for unbonded concrete overlays* (Report No. MN 2020-08). Minnesota Department of Transportation. https://rosap.ntl.bts.gov/view/dot/53552

King, D., & Akakin, T. (2023). *Performance of concrete overlays over full depth reclamation* (Report No. NRRA202301). National Concrete Pavement Technology Center/Minnesota Department of Transportation. https://mdl.mndot.gov/_flysystem/fedora/2023-03/nrra202301.pdf

King, D., & Roesler, J. R. (2014). Backcalculation procedure for bonded concrete overlays of asphalt pavement. *Transportation Research Record*, *2457*(2), 72–79. https://doi.org/10.3141/2457-08.

King, D., & Taylor, P. (2023). Survival analysis of concrete overlays on low-volume roads in Iowa. *Transportation Research Record*, *2679*(1), https://doi.org/10.1177/03611981221147263

Li, Z., & Vandenbossche, J. M. (2013). Redefining the failure mode for thin and ultrathin whitetopping with 1.8- × 1.8-m joint spacing. *Transportation Research Record*, *2368*(1), 133–144. https://doi.org/10.3141/2368-13

Pierce, L., Stolte, S., Weitzel, N., Medina, J., Van Dam, T., Senn, K., Roesler, J., Scott, G., Sen, S., Jadallah, O., Maser, K., Carmichael, A., Smith, K., & Smith, K. (2022). Evaluation of bonded concrete overlays on asphalt pavements. *Transportation Research Board*. https://doi.org/10.17226/26760

Sakulneya, A., Anderson, C., Castro Perez, J., & Roesler, J. (2024). *Performance and design of continuously reinforced concrete pavements* (Report No. FHWA-ICT-24-009). Illinois Center for Transportation. https://doi.org/10.36501/0197-9191/24-011

Sen, S., & Khazanovich, L. (2025). UNOL: Unbonded Overlay Design. https://software.pavements.pitt.edu/UNOL

Sheffield, M. T., Cavalline, T. L., & Dean, G. (2023). Insights into increasing the implementation of concrete overlay rehabilitation methods for highway pavements. *Transportation Research Record*, *2677*(3), 757–767. https://doi.org/10.1177/03611981221117539

Souder, N., DeSantis, J., Vandenbossche, J., & Sachs, S. (2020). Modeling the development of permanent deformation in asphalt interlayers of unbonded concrete overlays of concrete pavements. *Transportation Research Record*, *2674*(9), 489–499. https://doi.org/10.1177/0361198120930013

APPENDIX A: DISTRESS SURVEY

In the distress map the blue lines represent new longitudinal cracks observed in 2021, red lines are new cracks from 2025, and green circles are locations for MIRA testing and core extraction.

I-72 EB

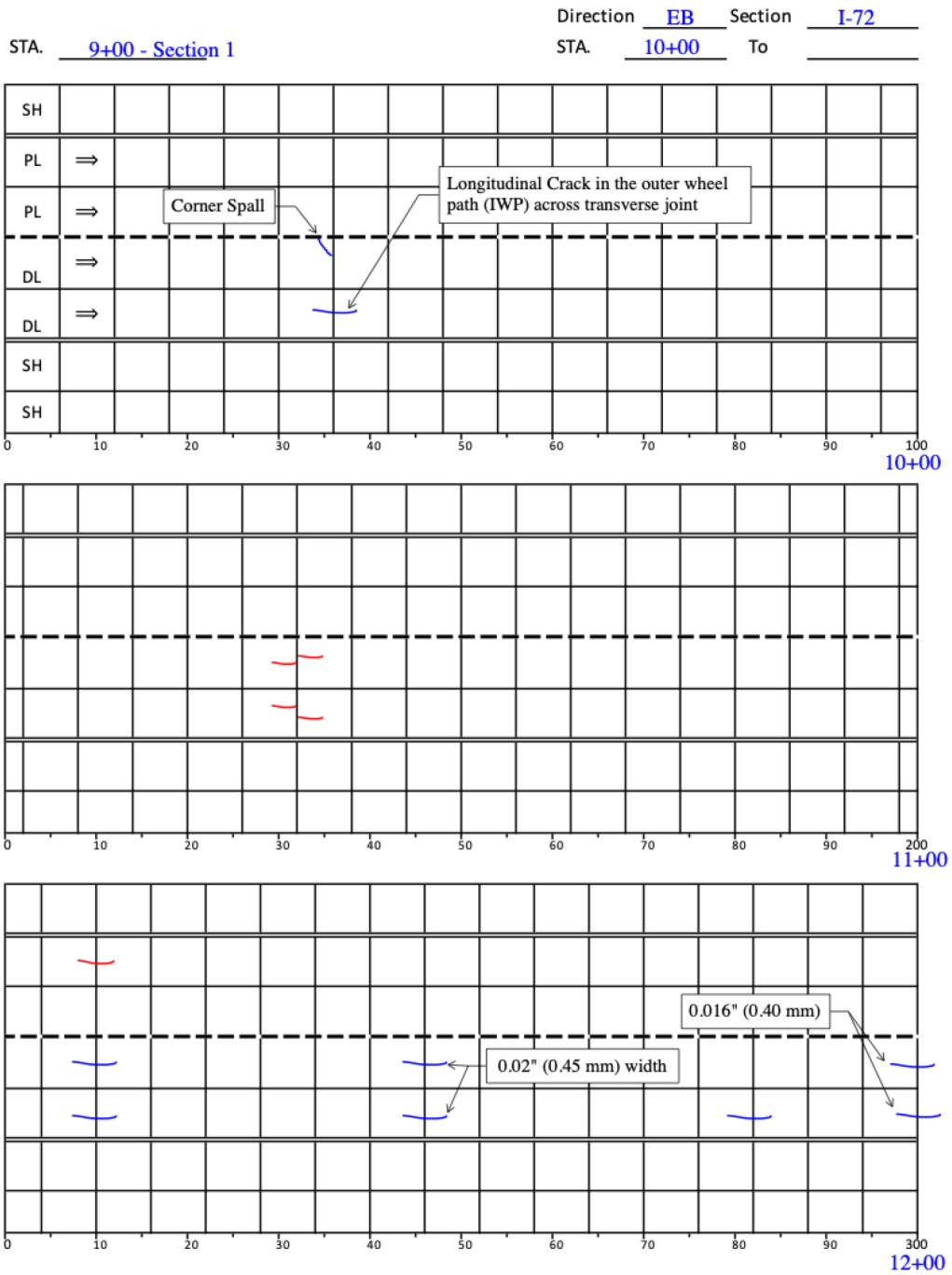

Figure 68. Illustration. Distress survey in I-72 EB at stations 9+00–12+00.

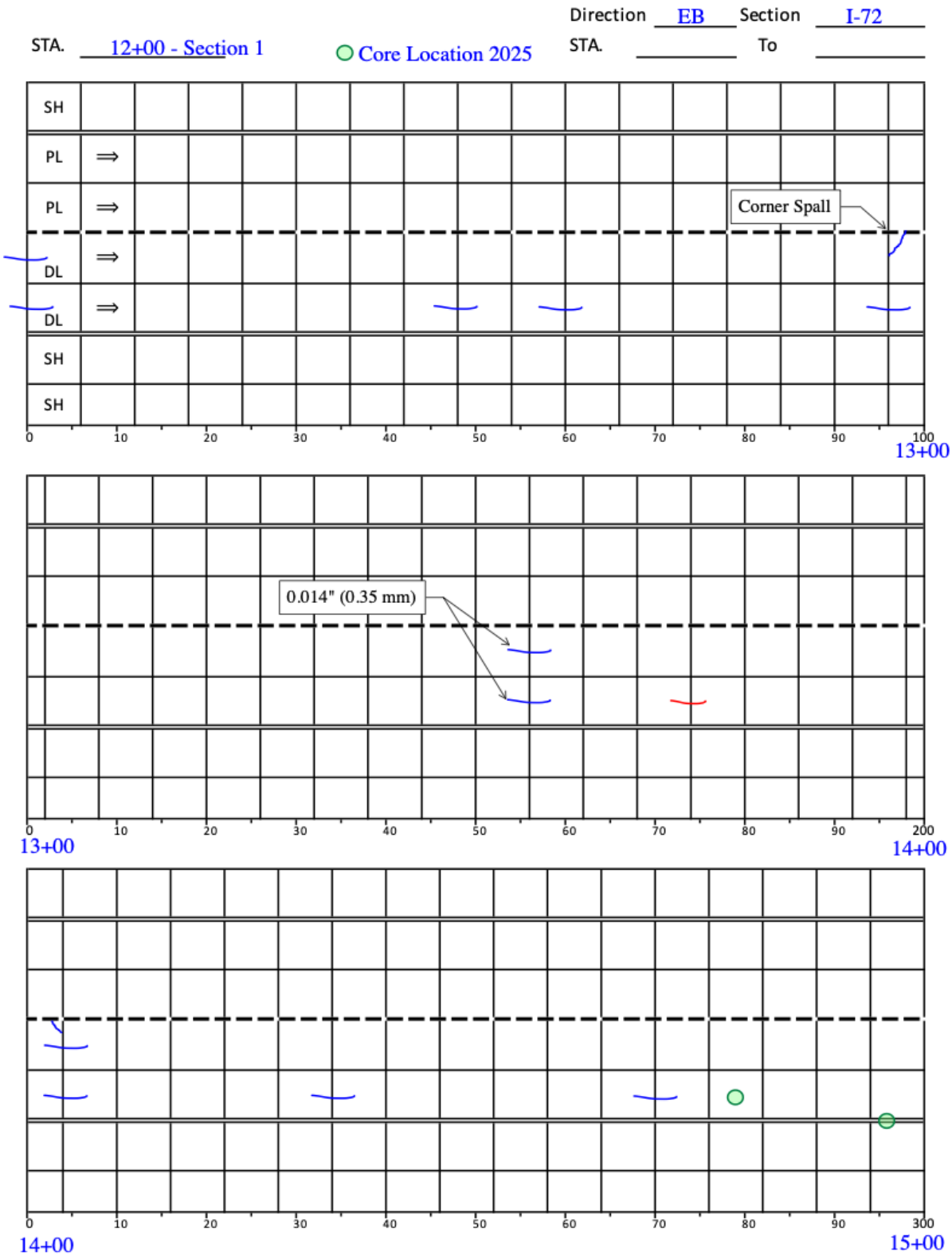

Figure 69. Illustration. Distress survey in I-72 EB at stations 12+00–15+00.

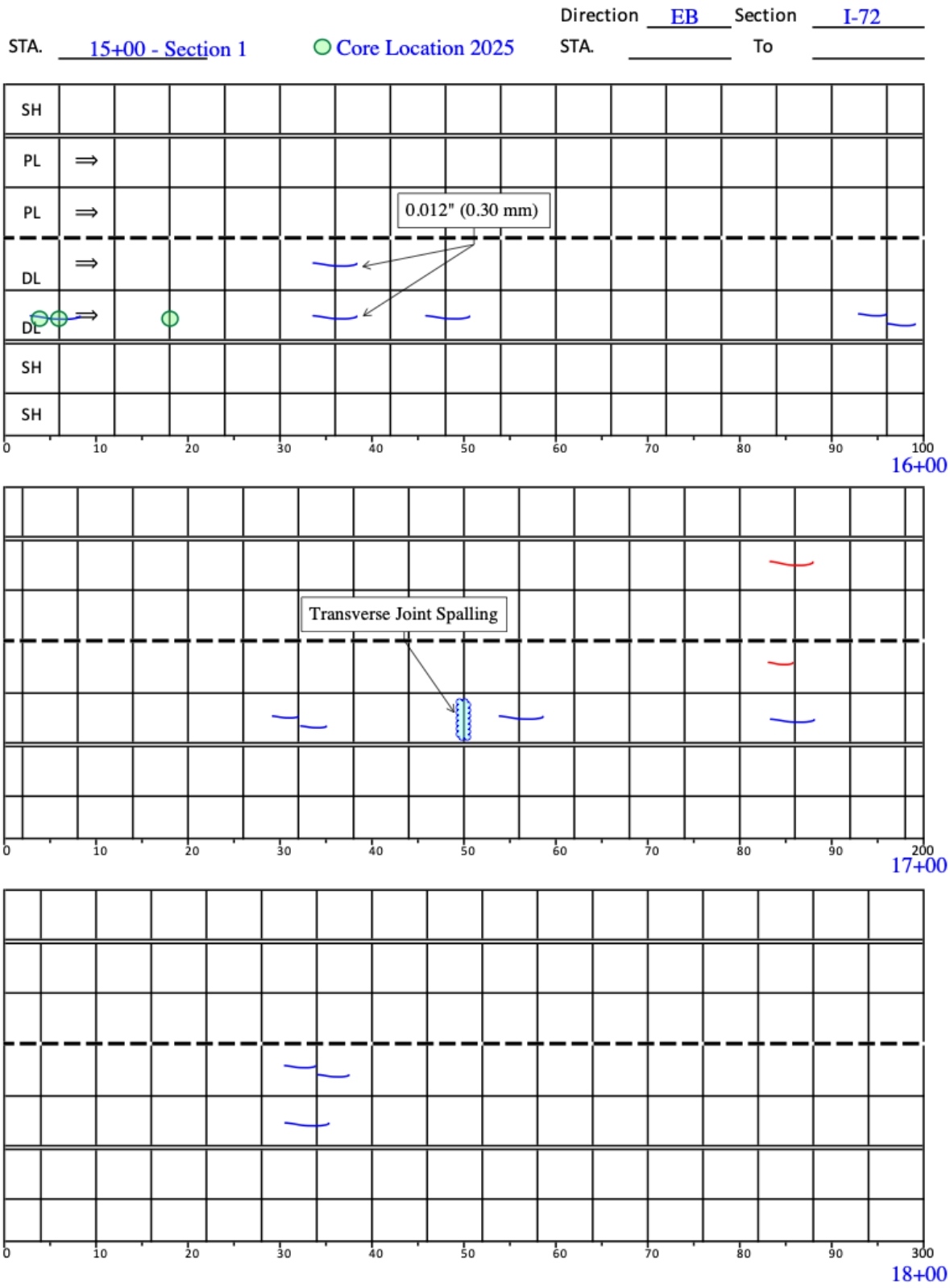

Figure 70. Illustration. Distress survey in I-72 EB at stations 15+00–18+00.

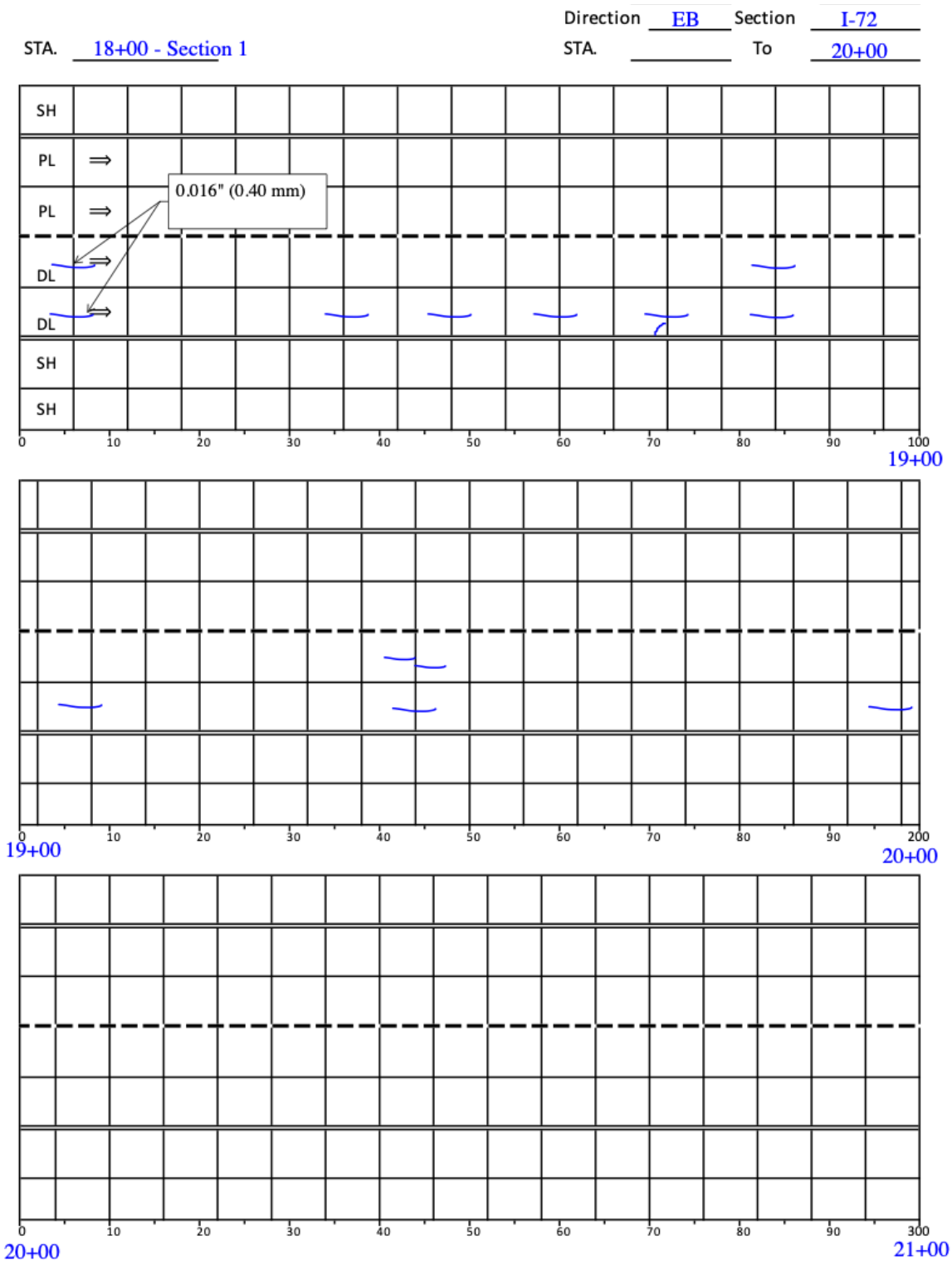

Figure 71. Illustration. Distress survey in I-72 EB at stations 18+00–21+00.

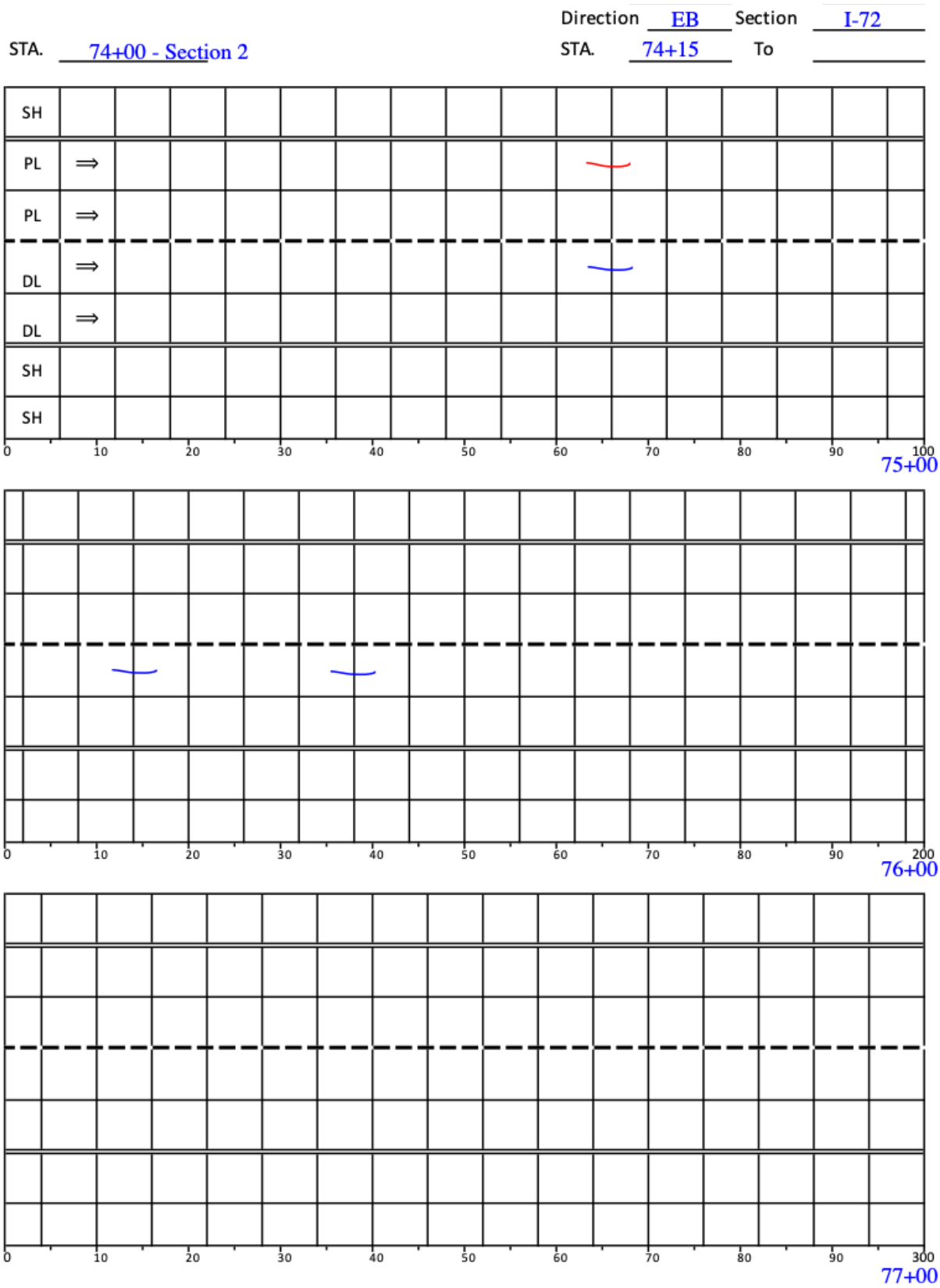

Figure 72. Illustration. Distress survey in I-72 EB at stations 74+00–77+00.

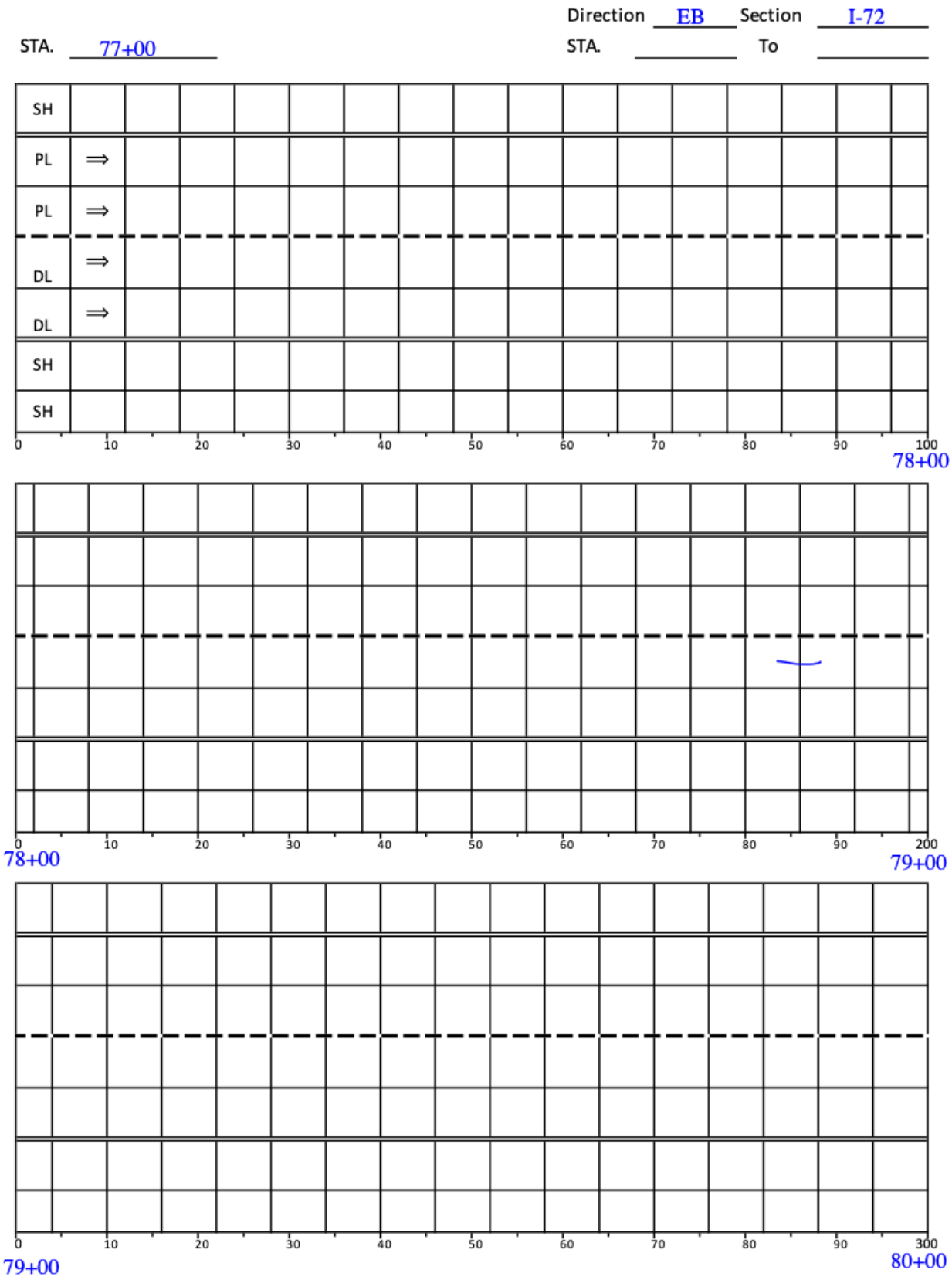

Figure 73. Illustration. Distress survey in I-72 EB at stations 77+00–80+00.

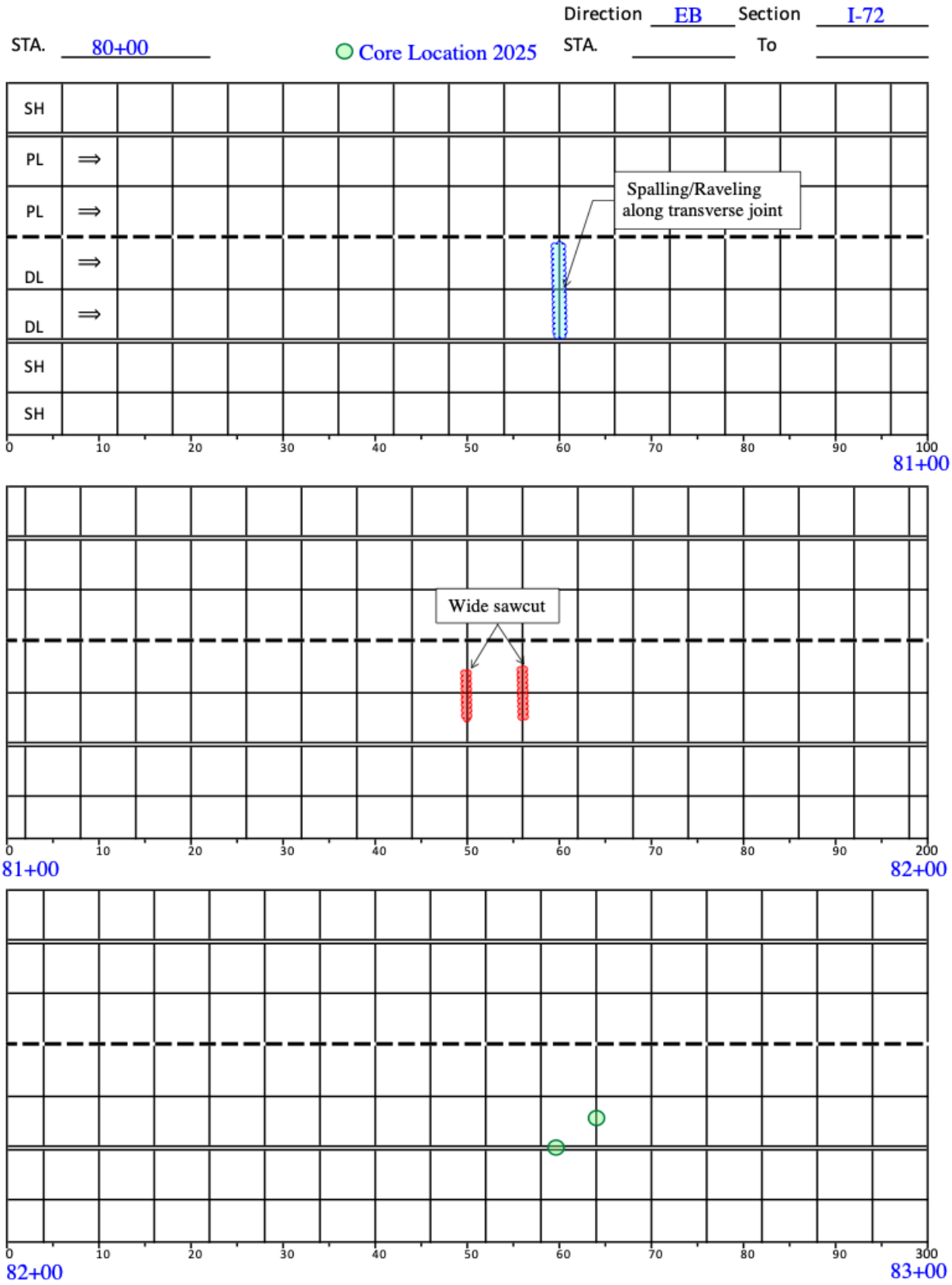

Figure 74. Illustration. Distress survey in I-72 EB at stations 80+00–83+00.

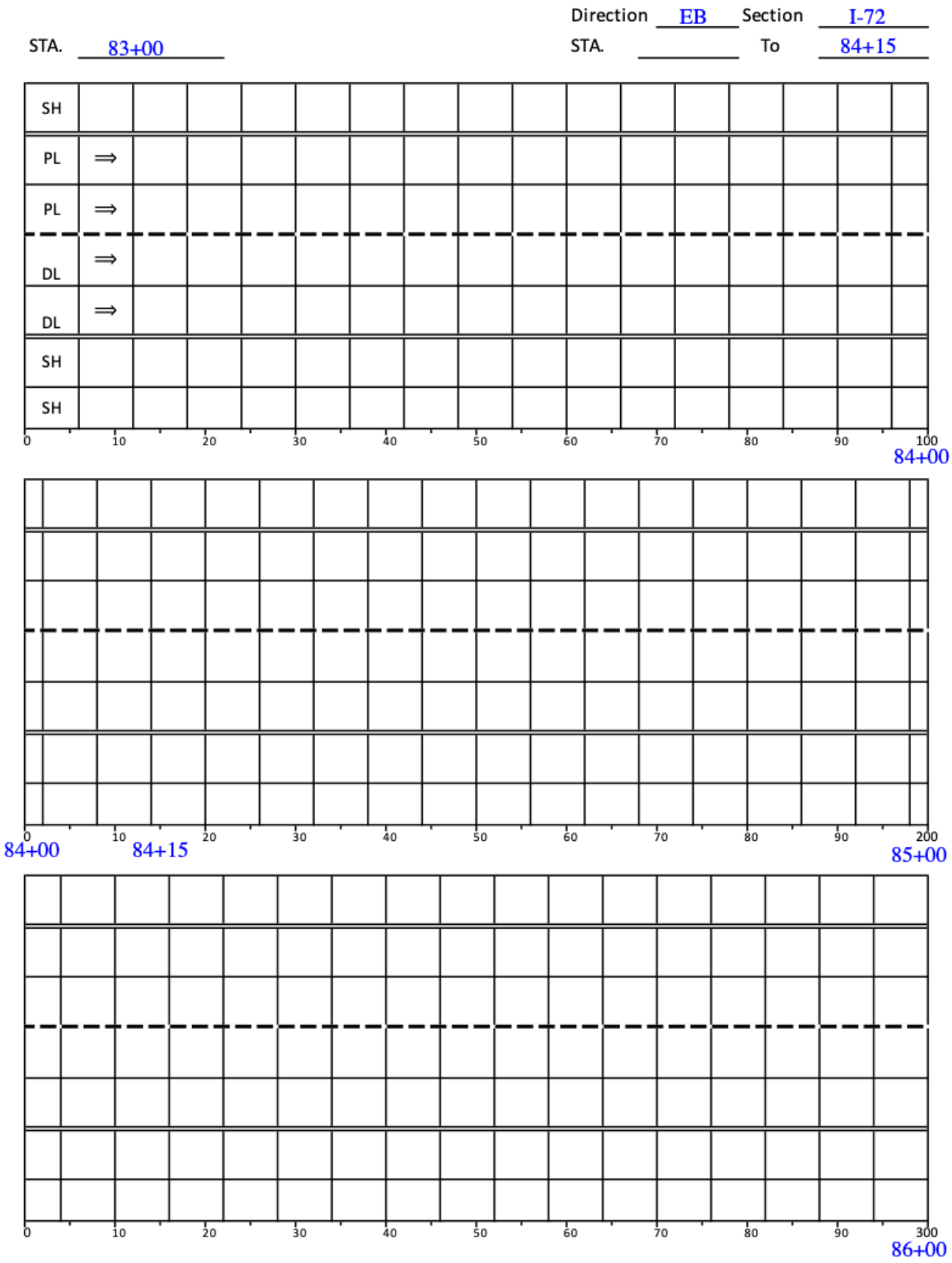

Figure 75. Illustration. Distress survey in I-72 EB at stations 83+00–86+00.

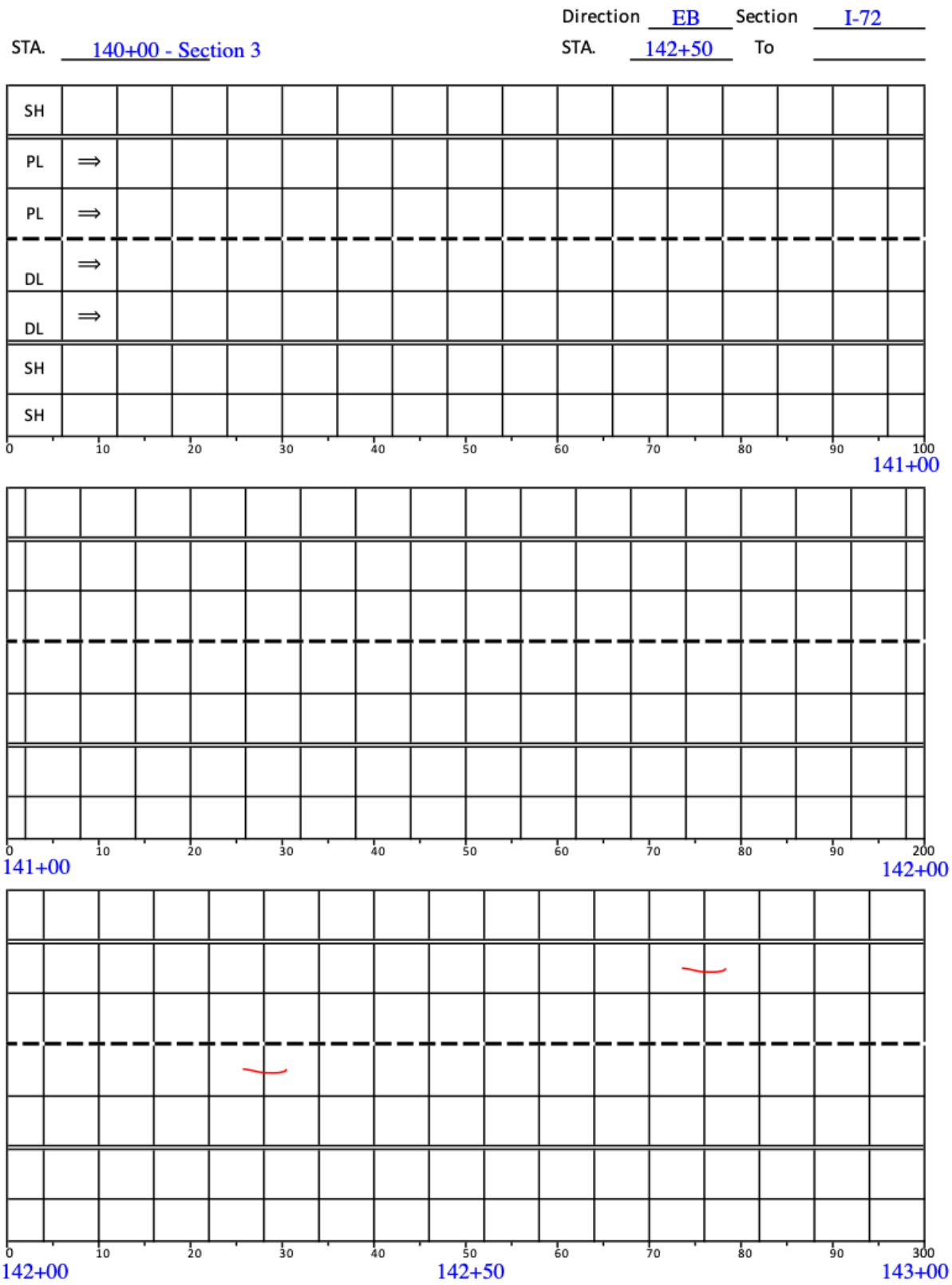

Figure 76. Illustration. Distress survey in I-72 EB at stations 140+00–143+00.

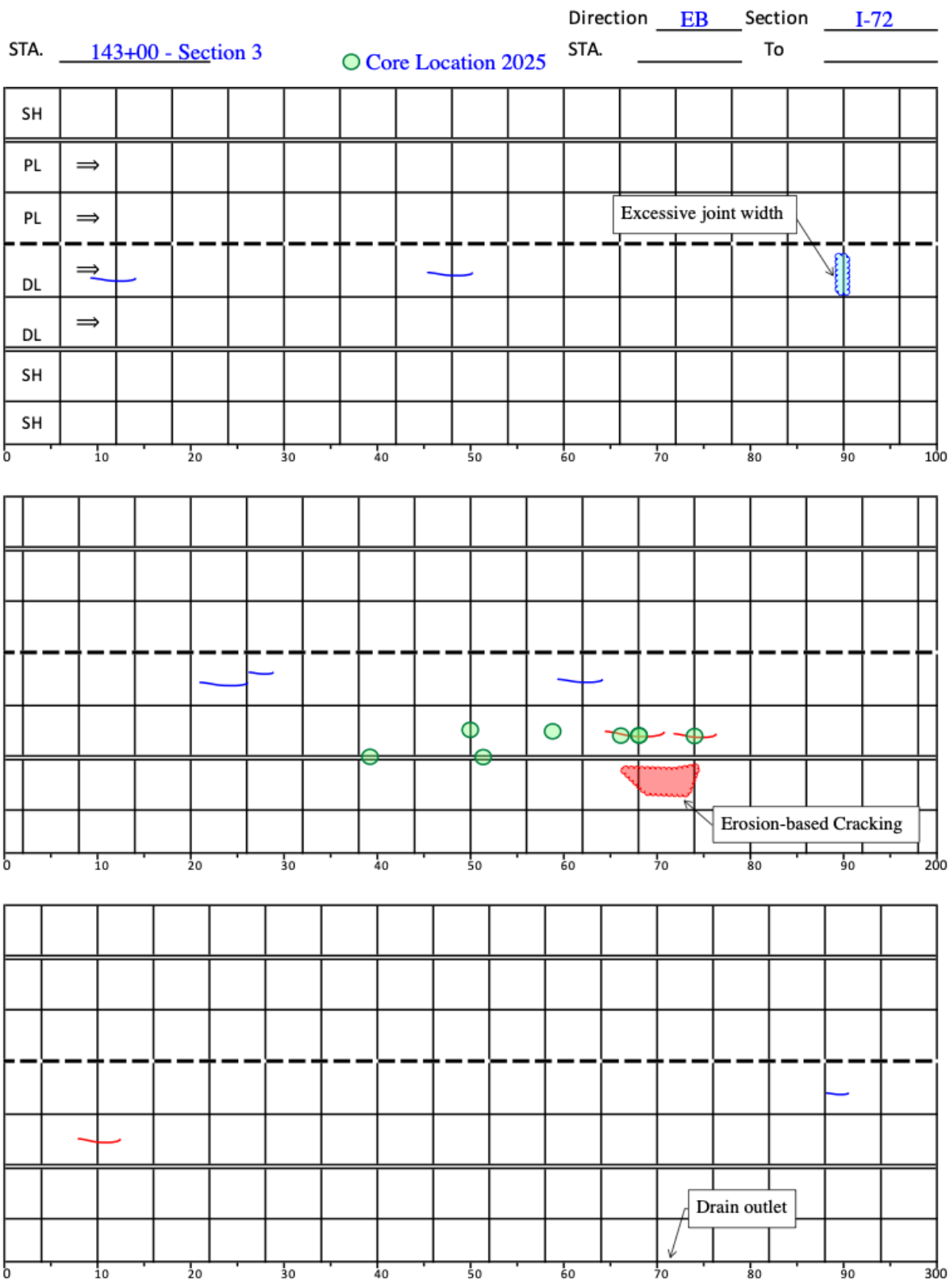

Figure 77. Illustration. Distress survey in I-72 EB at stations 143+00–146+00.

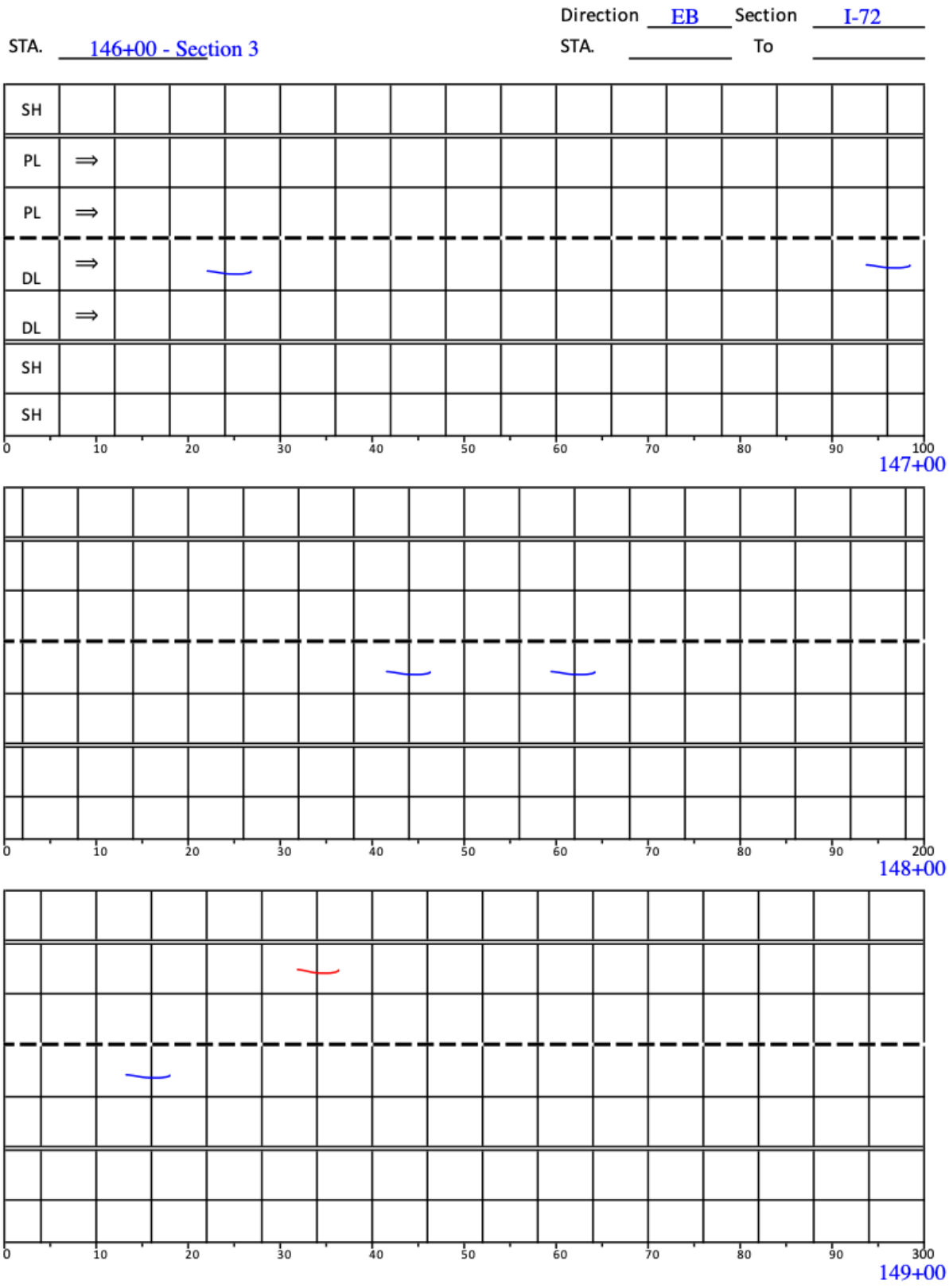

Figure 78. Illustration. Distress survey in I-72 EB at stations 146+00–149+00.

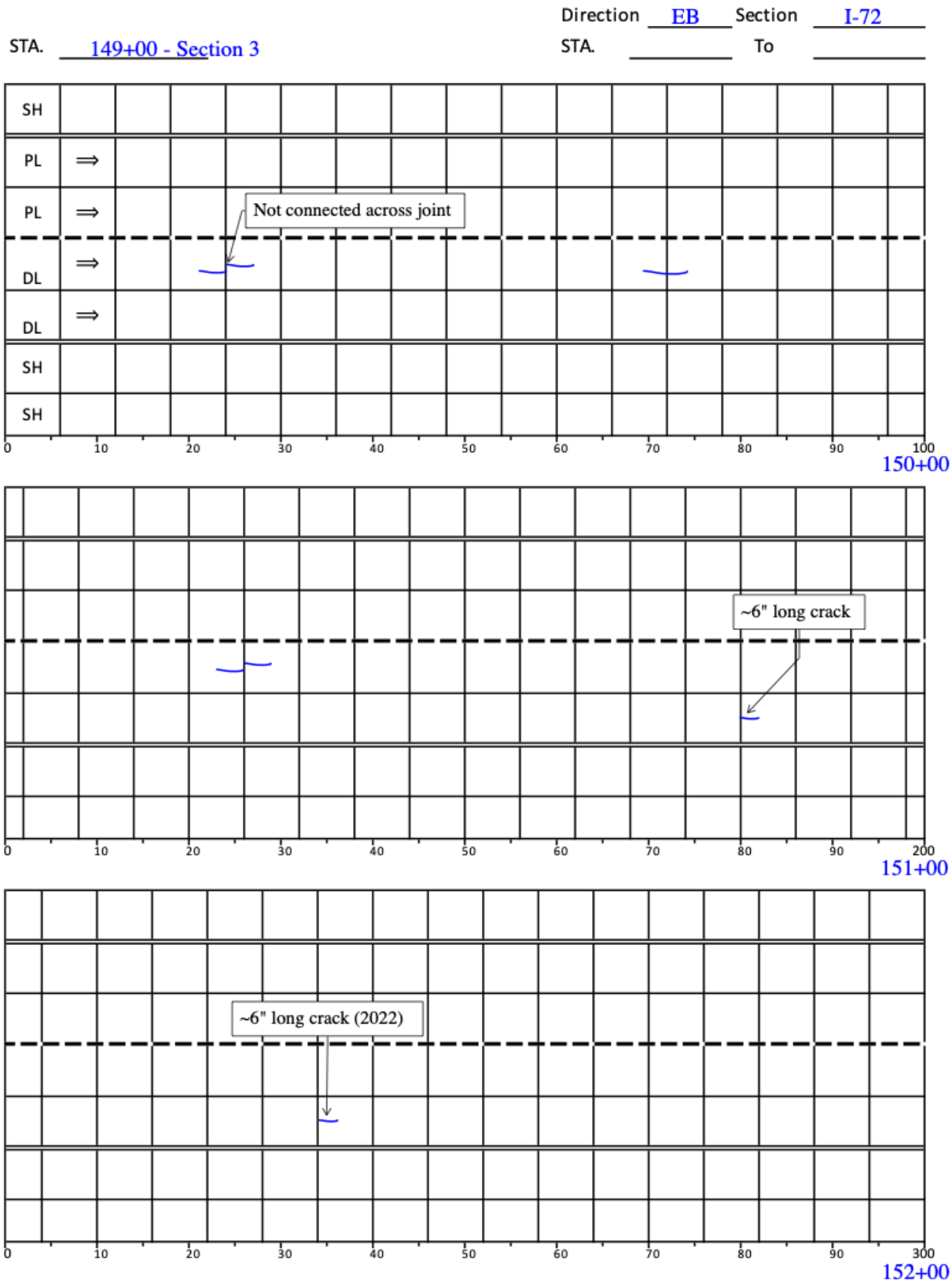

Figure 79. Illustration. Distress survey in I-72 EB at stations 149+00–152+00.

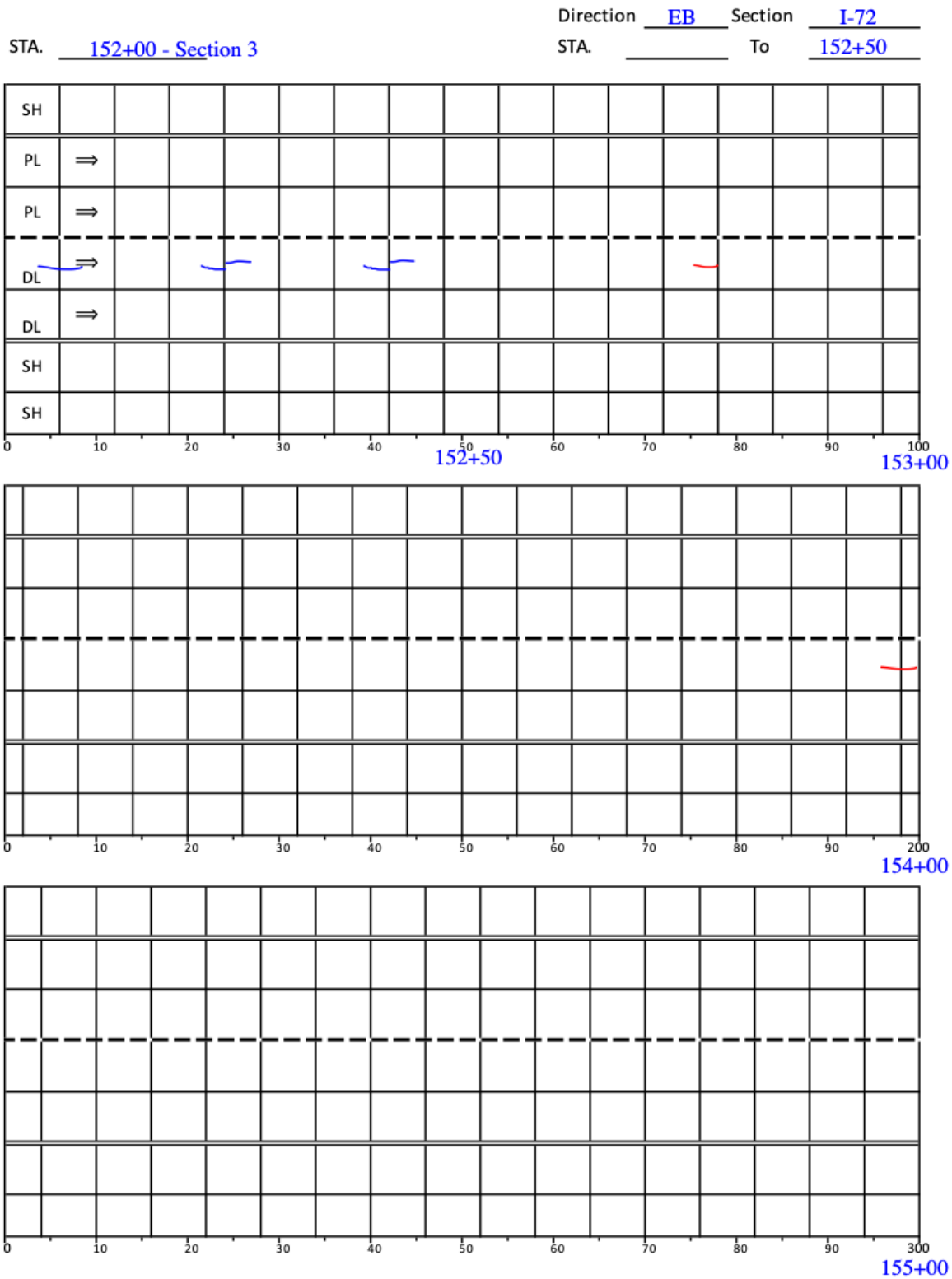

Figure 80. Illustration. Distress survey in I-72 EB at stations 152+00–155+00.

I-72 WB

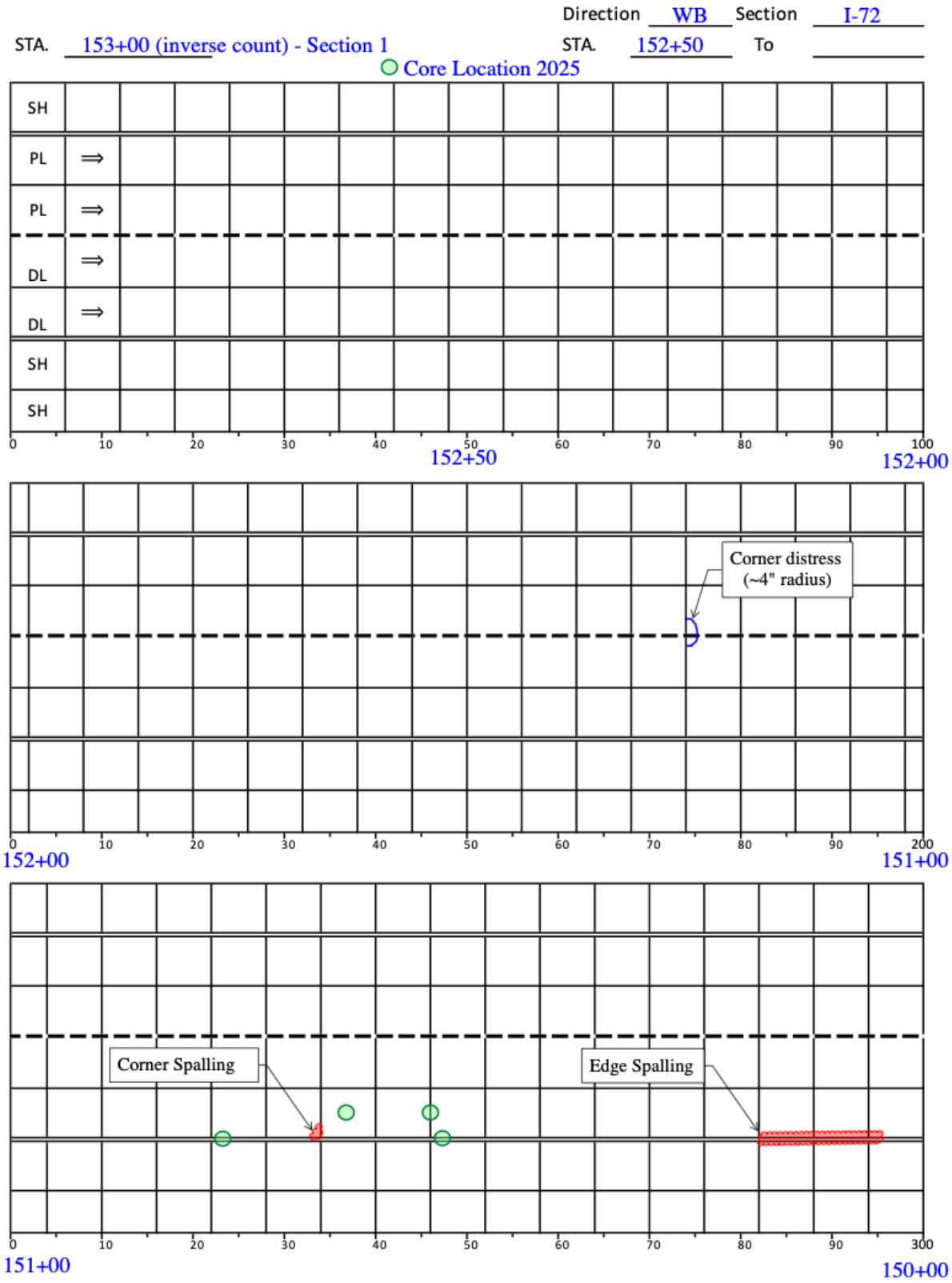

Figure 81. Illustration. Distress survey in I-72 WB at stations 153+00–150+00.

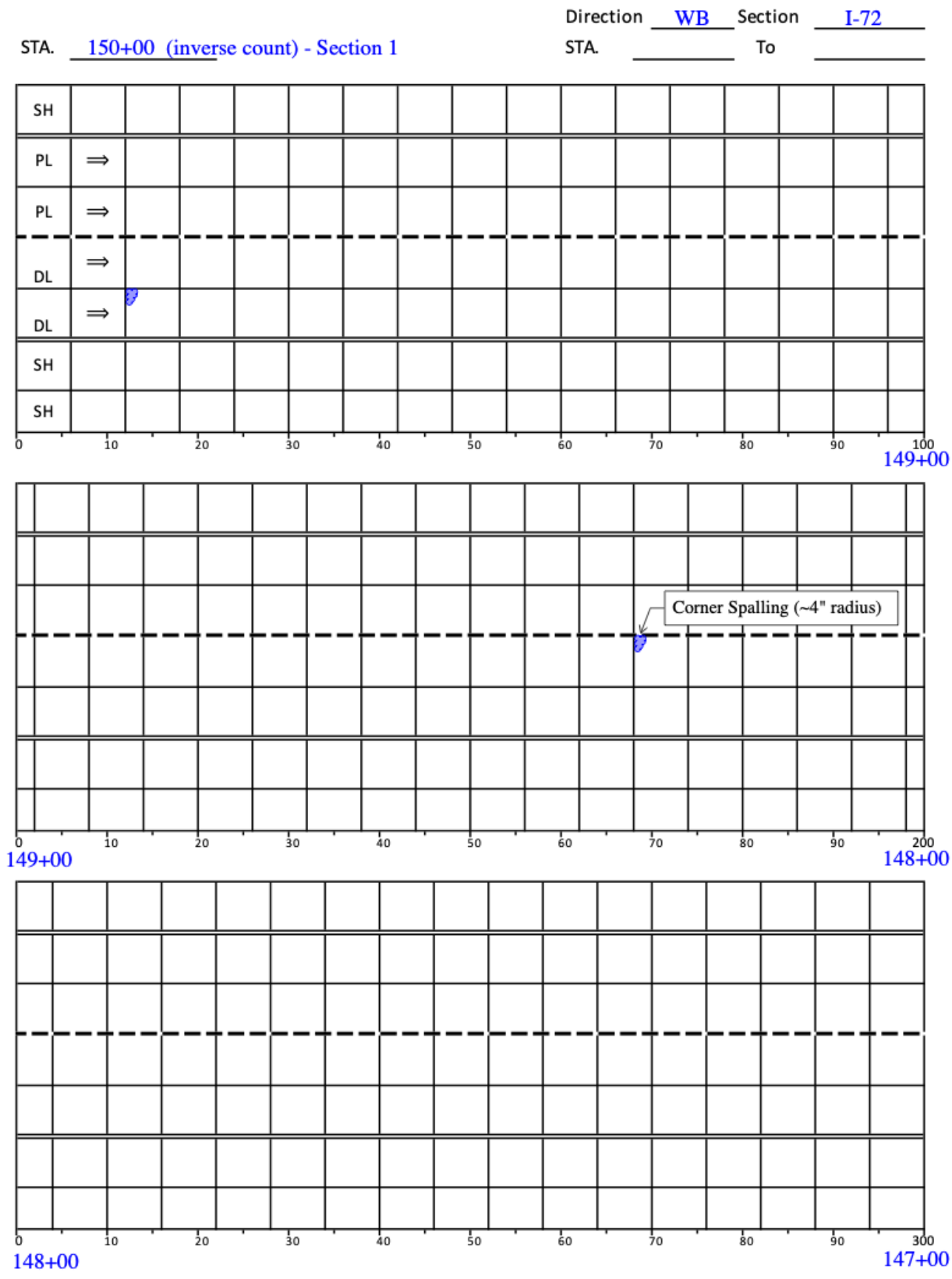

Figure 82. Illustration. Distress survey in I-72 WB at stations 150+00–147+00.

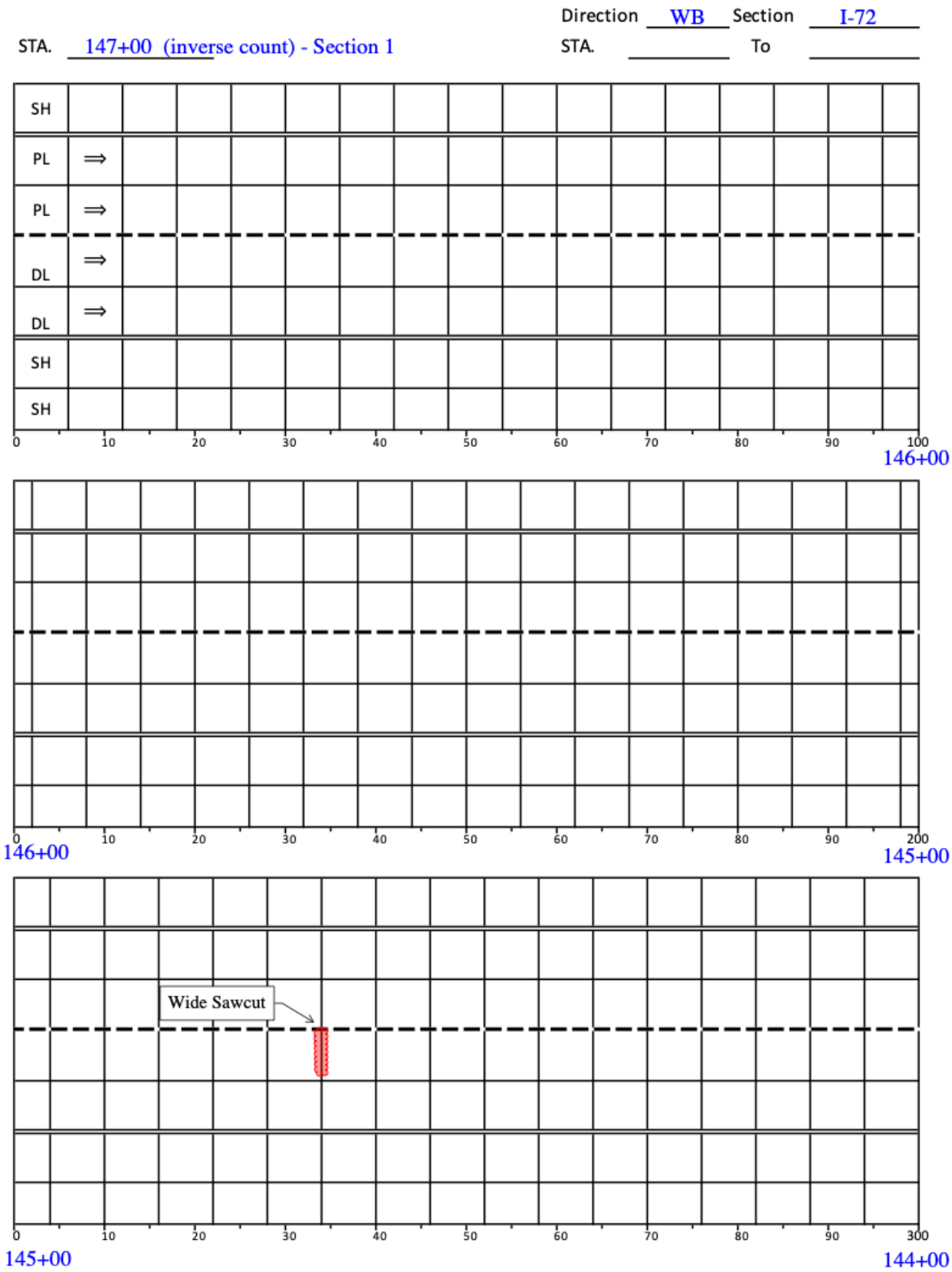

Figure 83. Illustration. Distress survey in I-72 WB at stations 147+00–144+00.

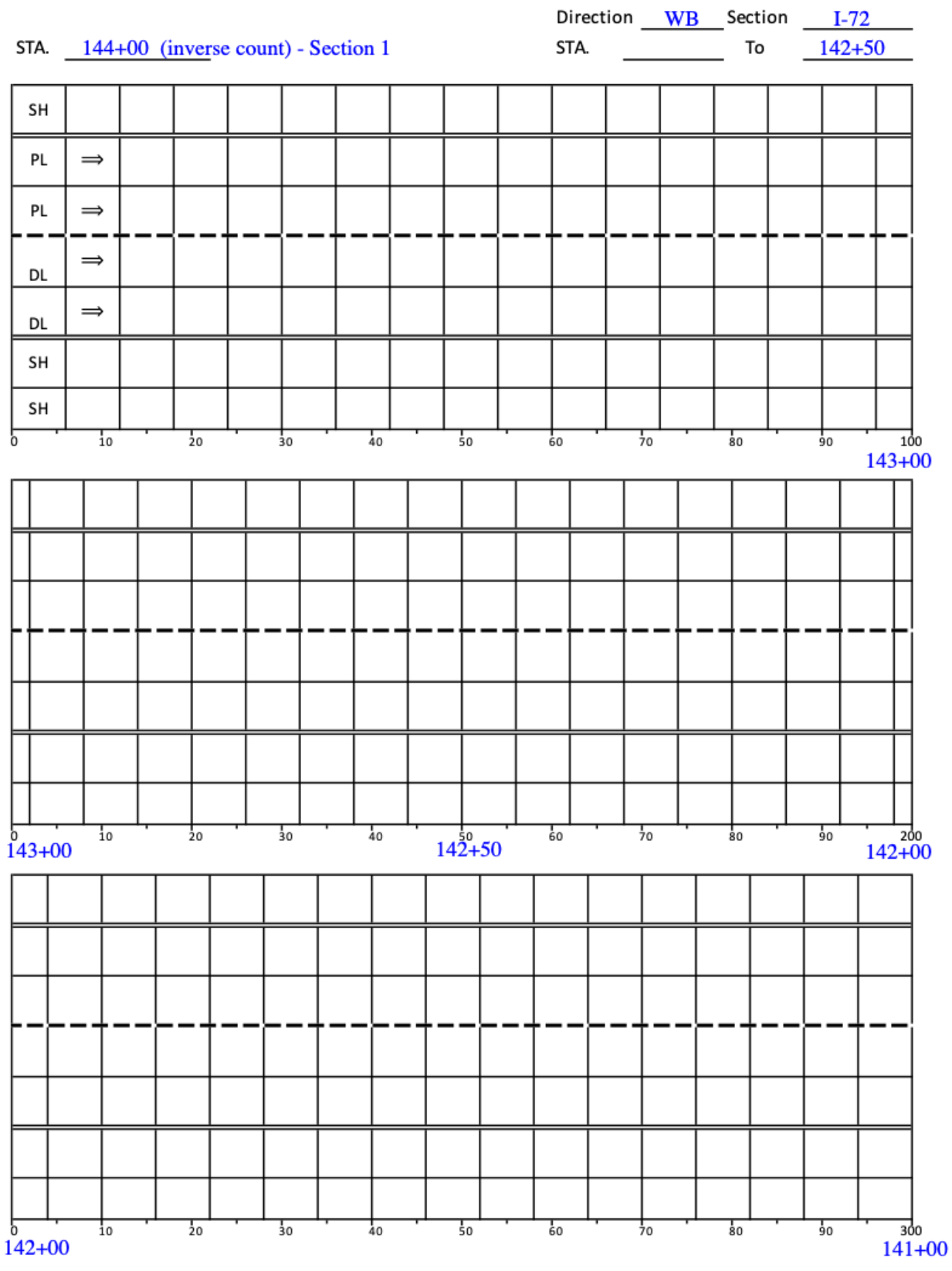

Figure 84. Illustration. Distress survey in I-72 WB at stations 144+00–141+00.

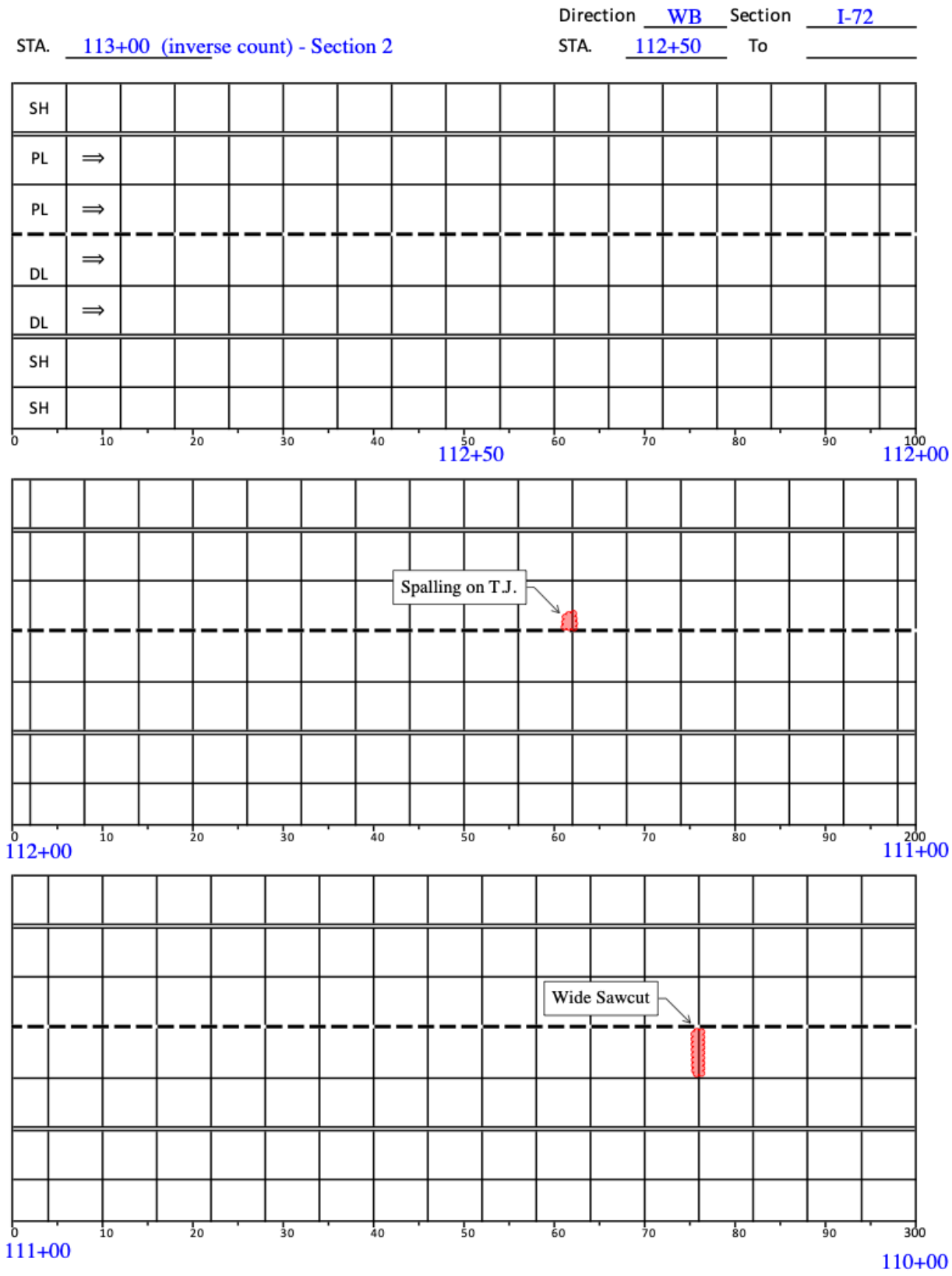

Figure 85. Illustration. Distress survey in I-72 WB at stations 113+00–110+00.

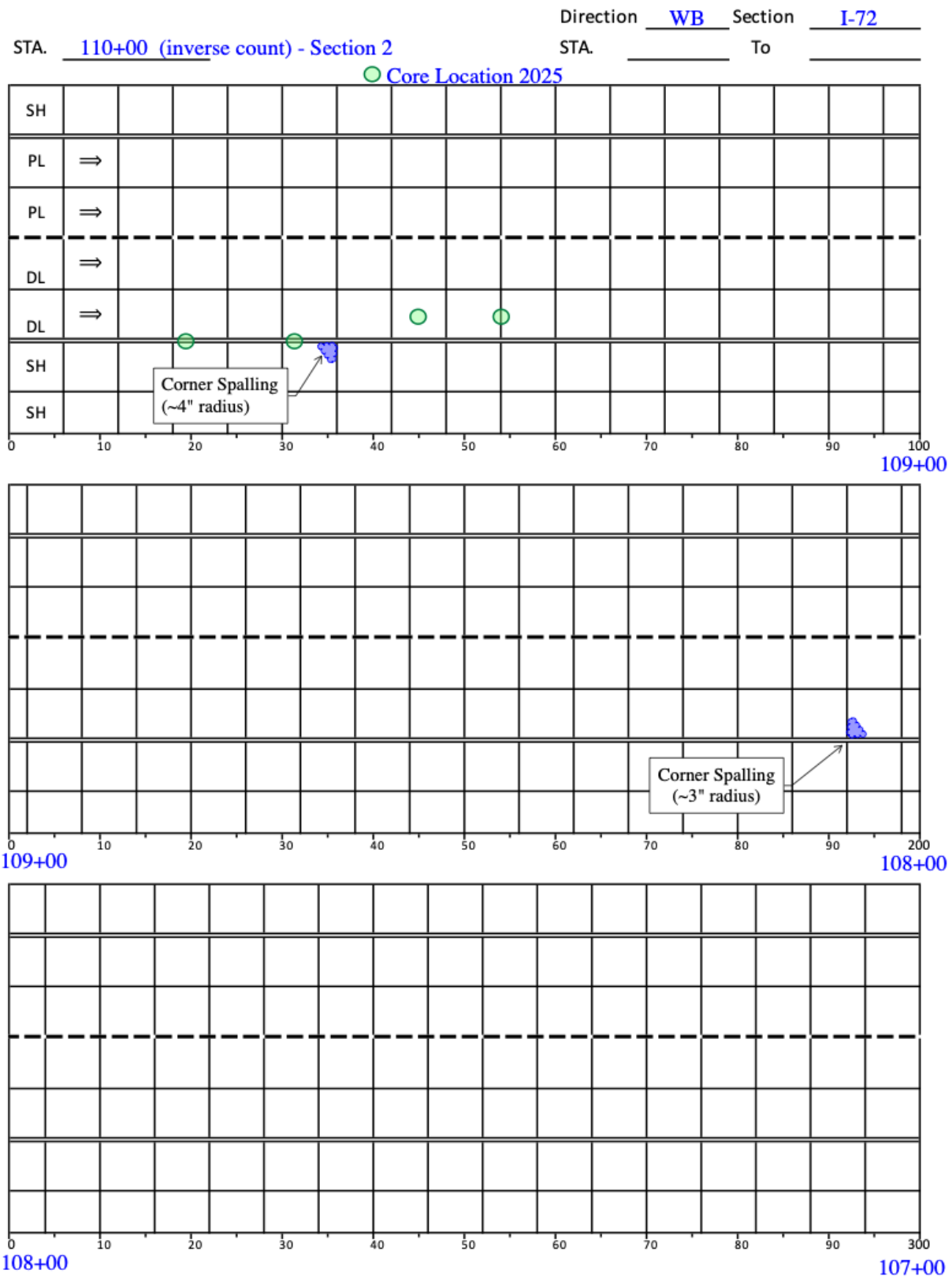

Figure 86. Illustration. Distress survey in I-72 WB at stations 110+00–107+00.

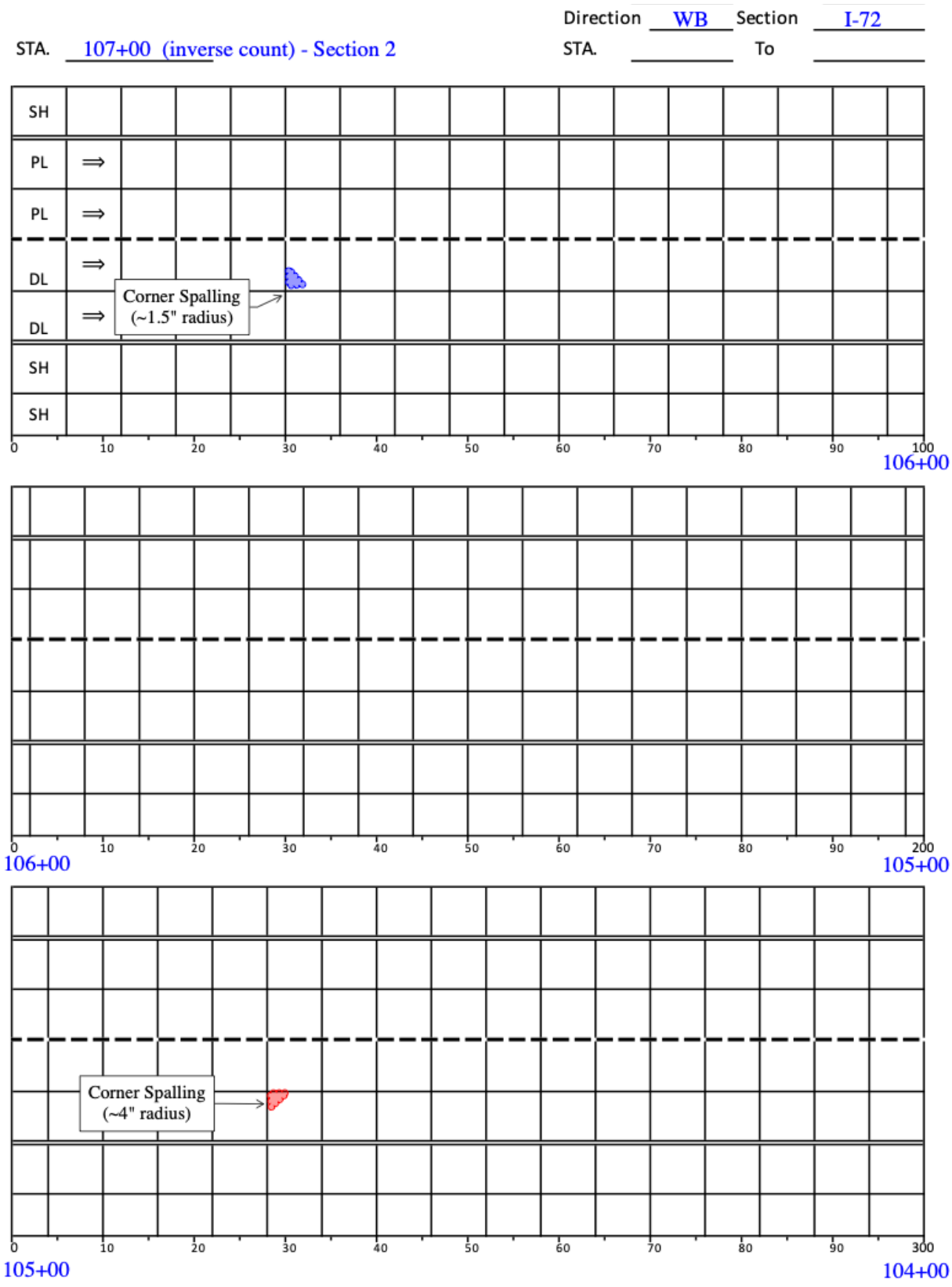

Figure 87. Illustration. Distress survey in I-72 WB at stations 107+00–104+00.

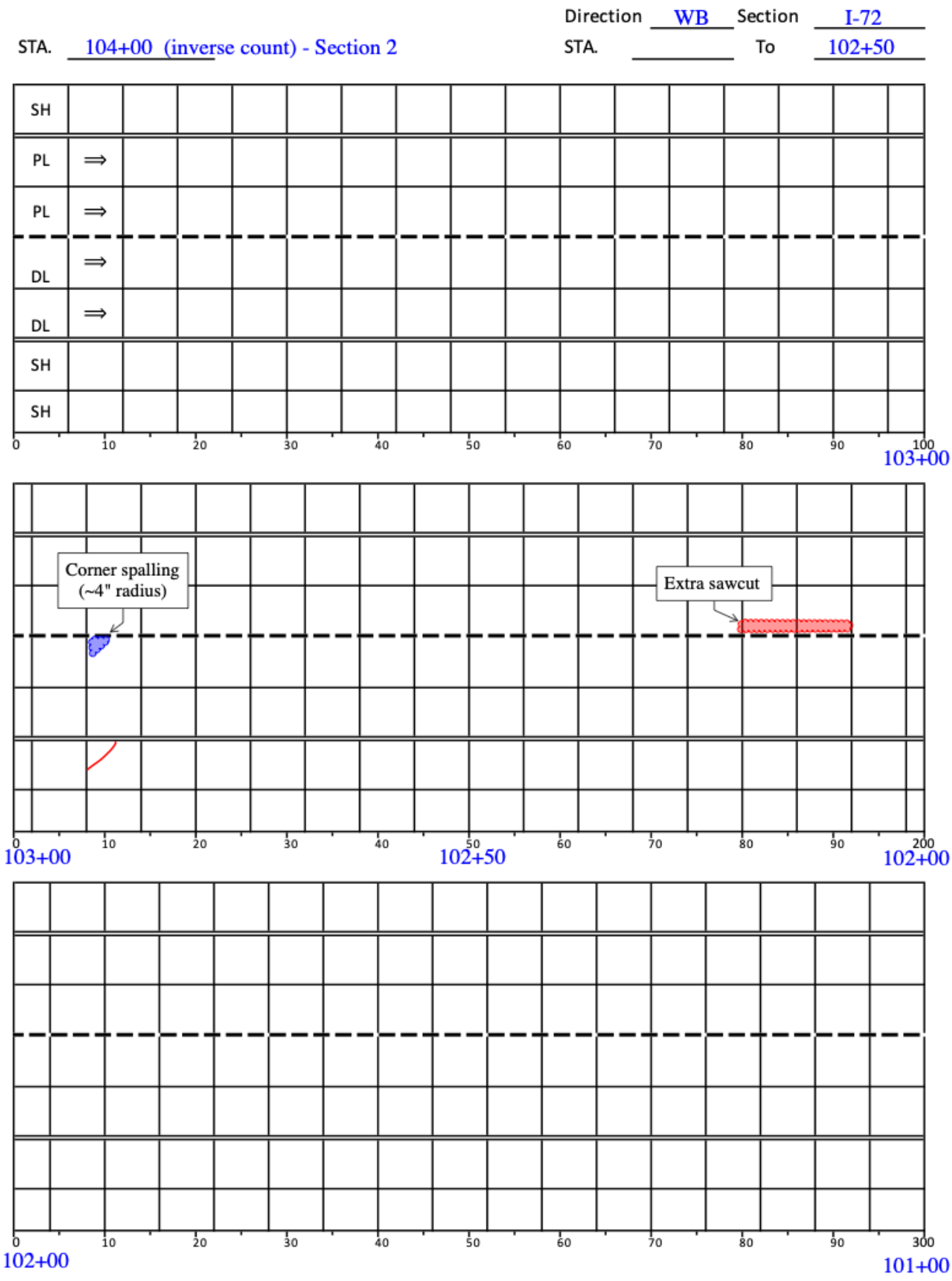

Figure 88. Illustration. Distress survey in I-72 WB at stations 104+00–101+00.

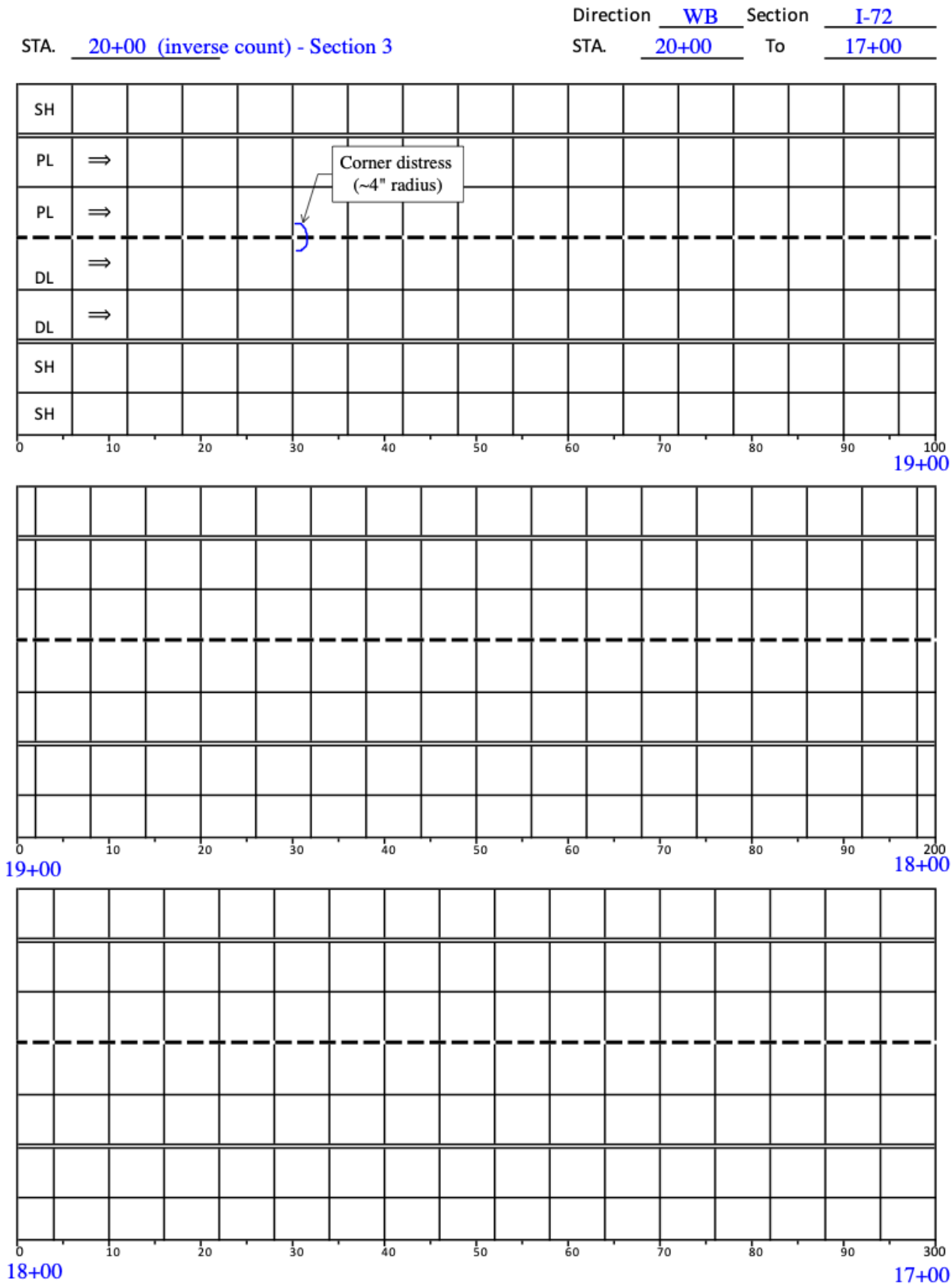

Figure 89. Illustration. Distress survey in I-72 WB at stations 20+00–17+00.

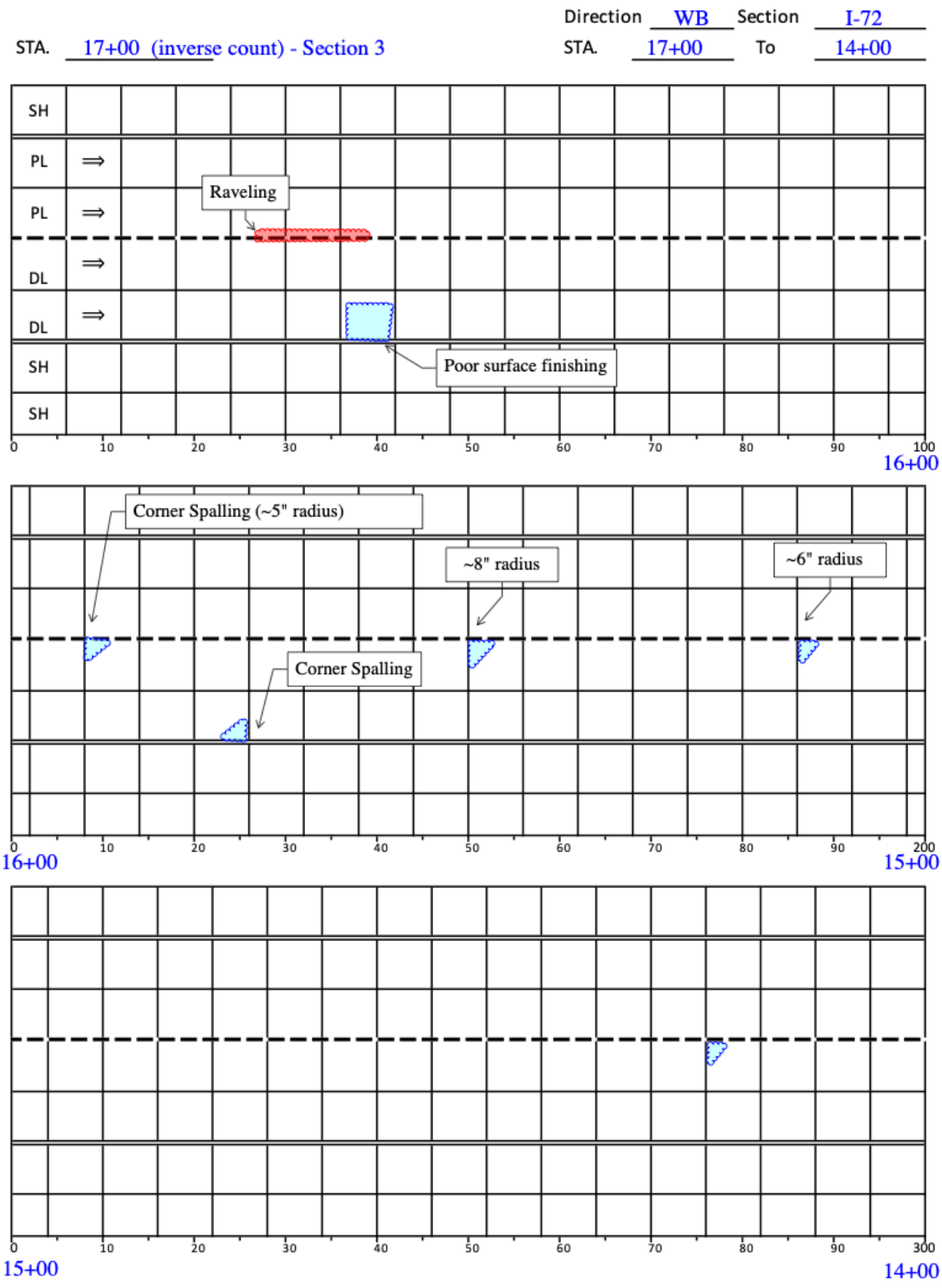

Figure 90. Illustration. Distress survey in I-72 WB at stations 17+00–14+00.

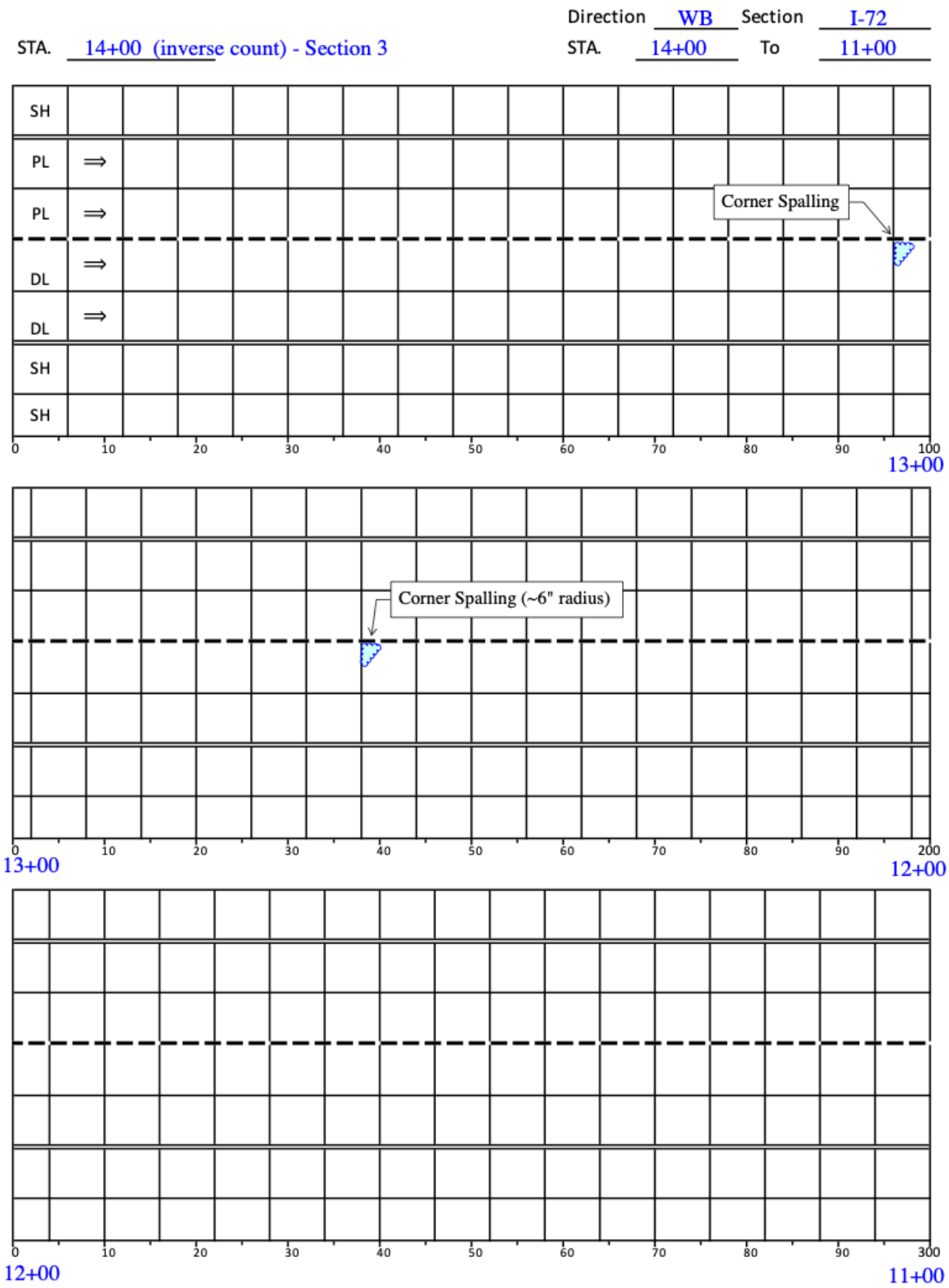

Figure 91. Illustration. Distress survey in I-72 WB at stations 14+00–11+00.

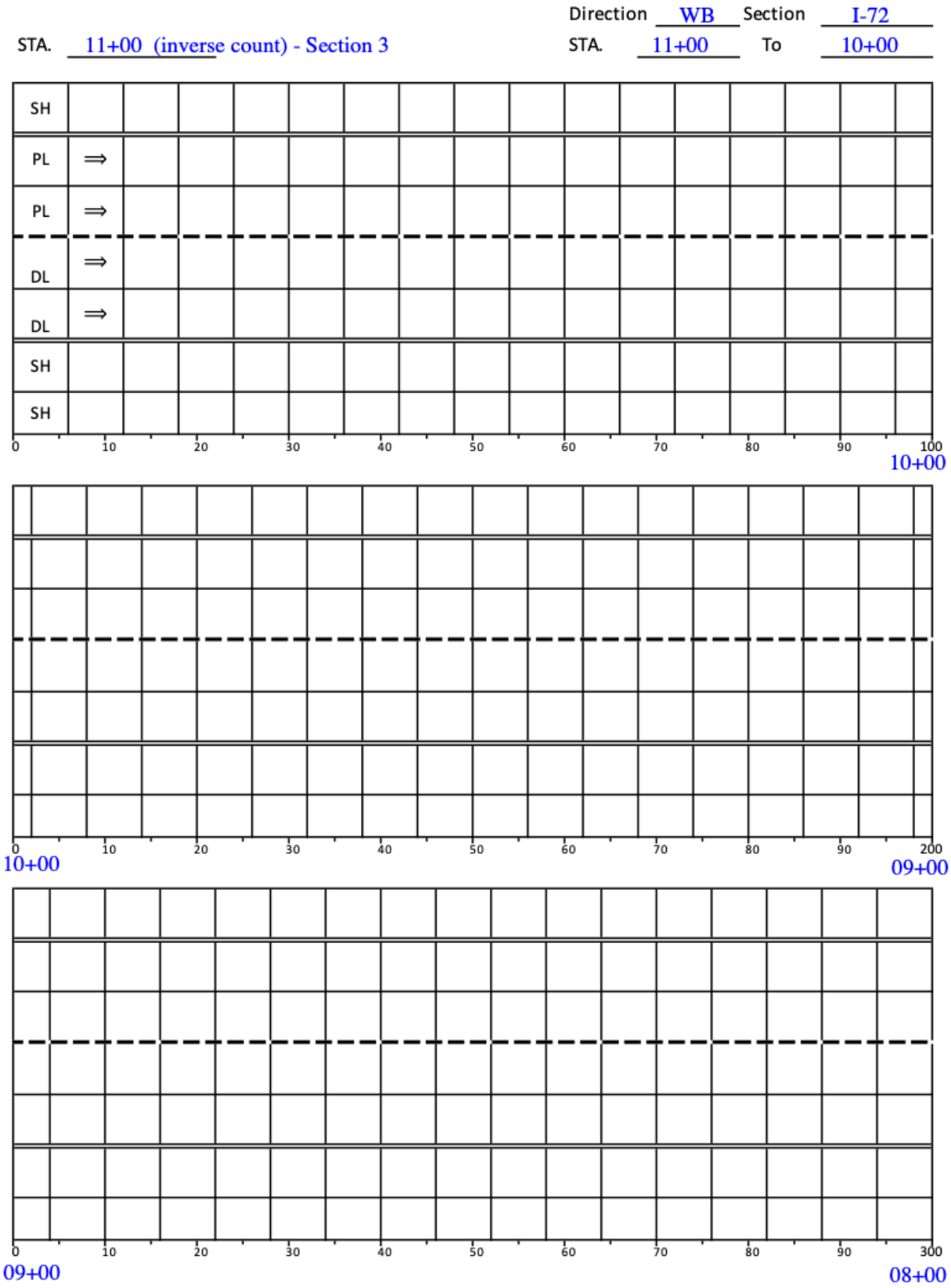

Figure 92. Illustration. Distress survey in I-72 WB at stations 11+00–8+00.

APPENDIX B: DISTRESS SURVEY IN CRAINVILLE, ILLINOIS

In the distress map the blue lines represent new longitudinal cracks observed in 2021, red lines are new cracks from 2025, and blue boxes are locations for MIRA testing.

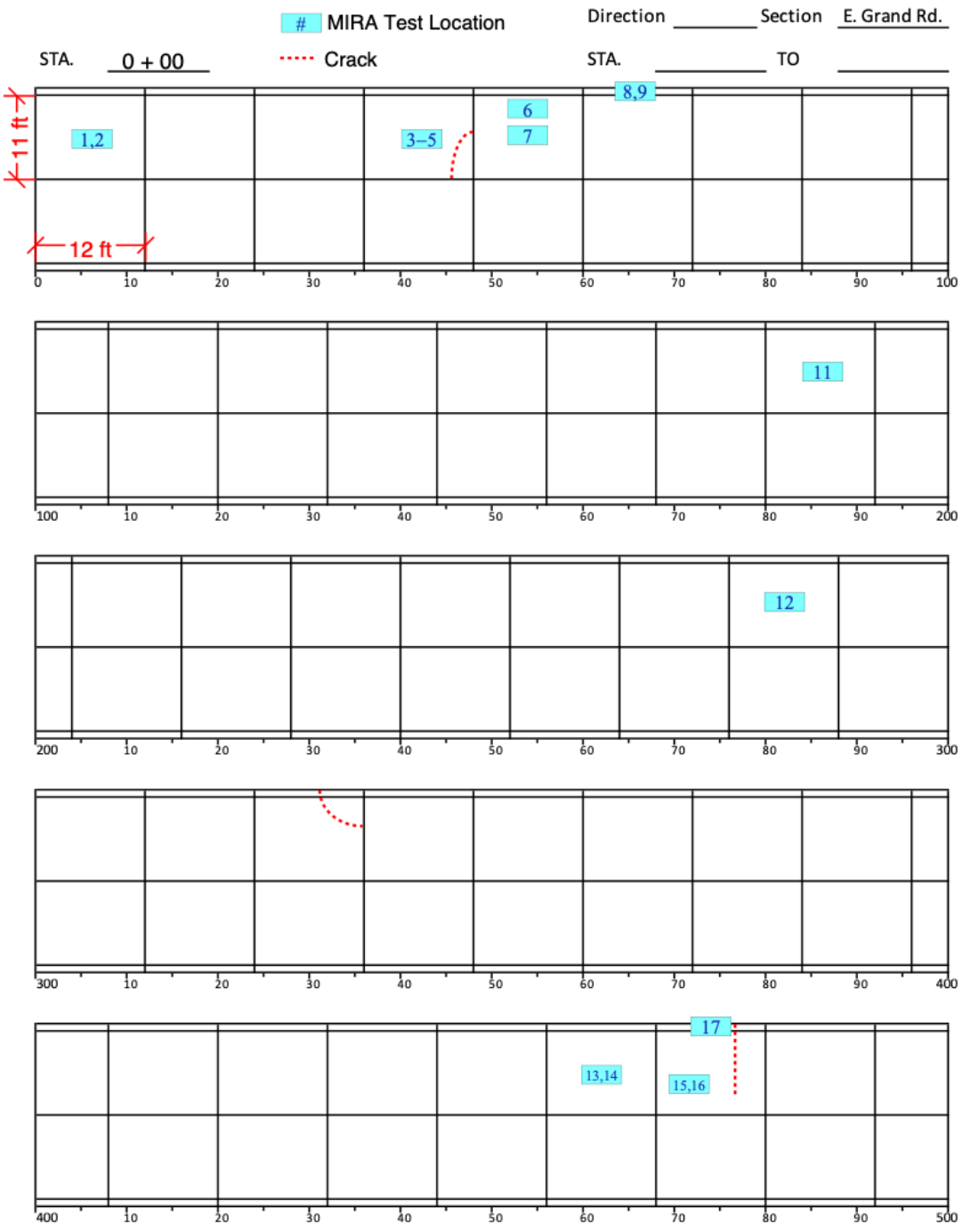

Figure 93. Illustration. Distress survey in East Grand Road at stations 0+00–5+00.

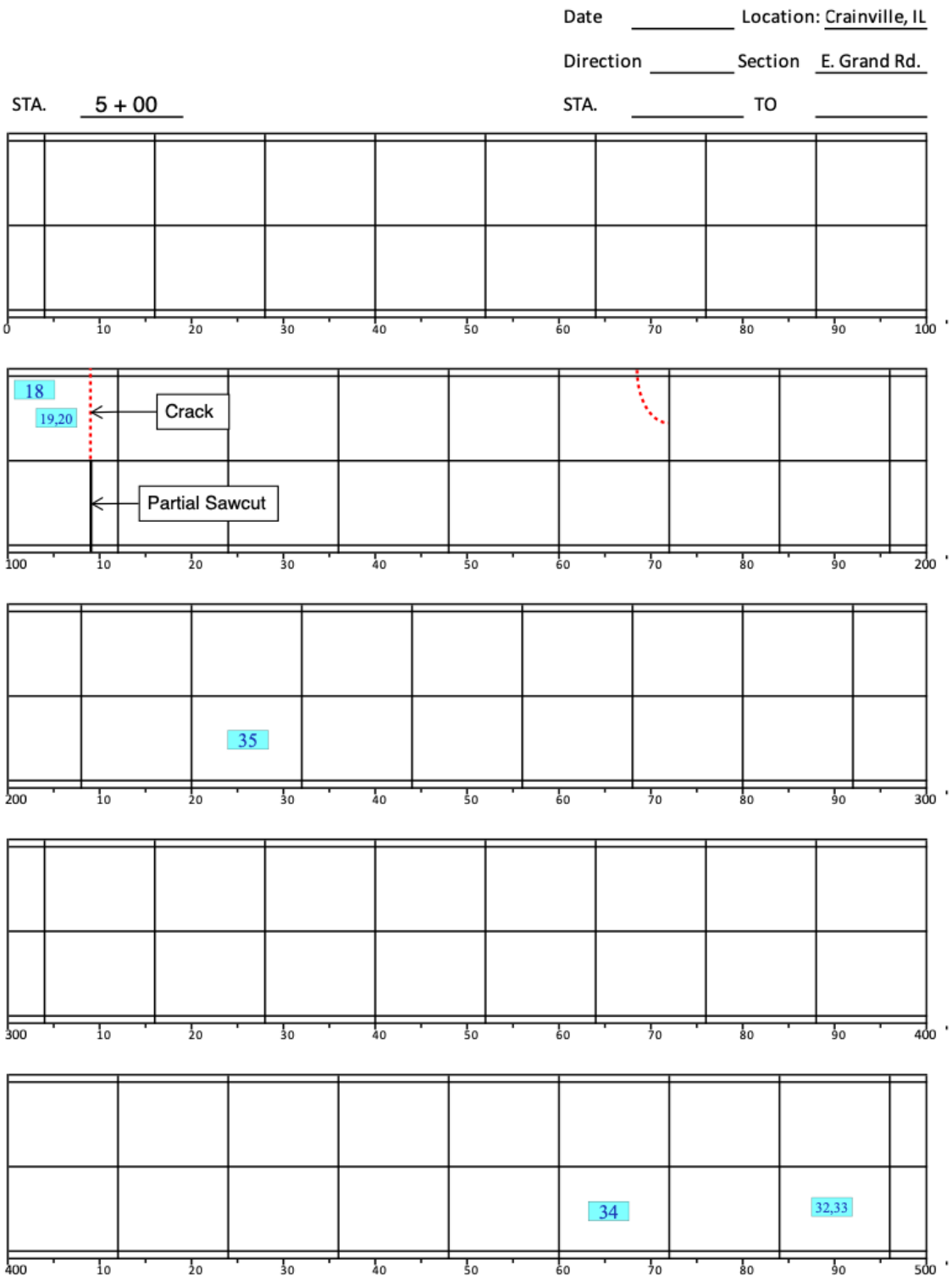

Figure 94. Illustration. Distress survey in East Grand Road at stations 5+00–10+00.

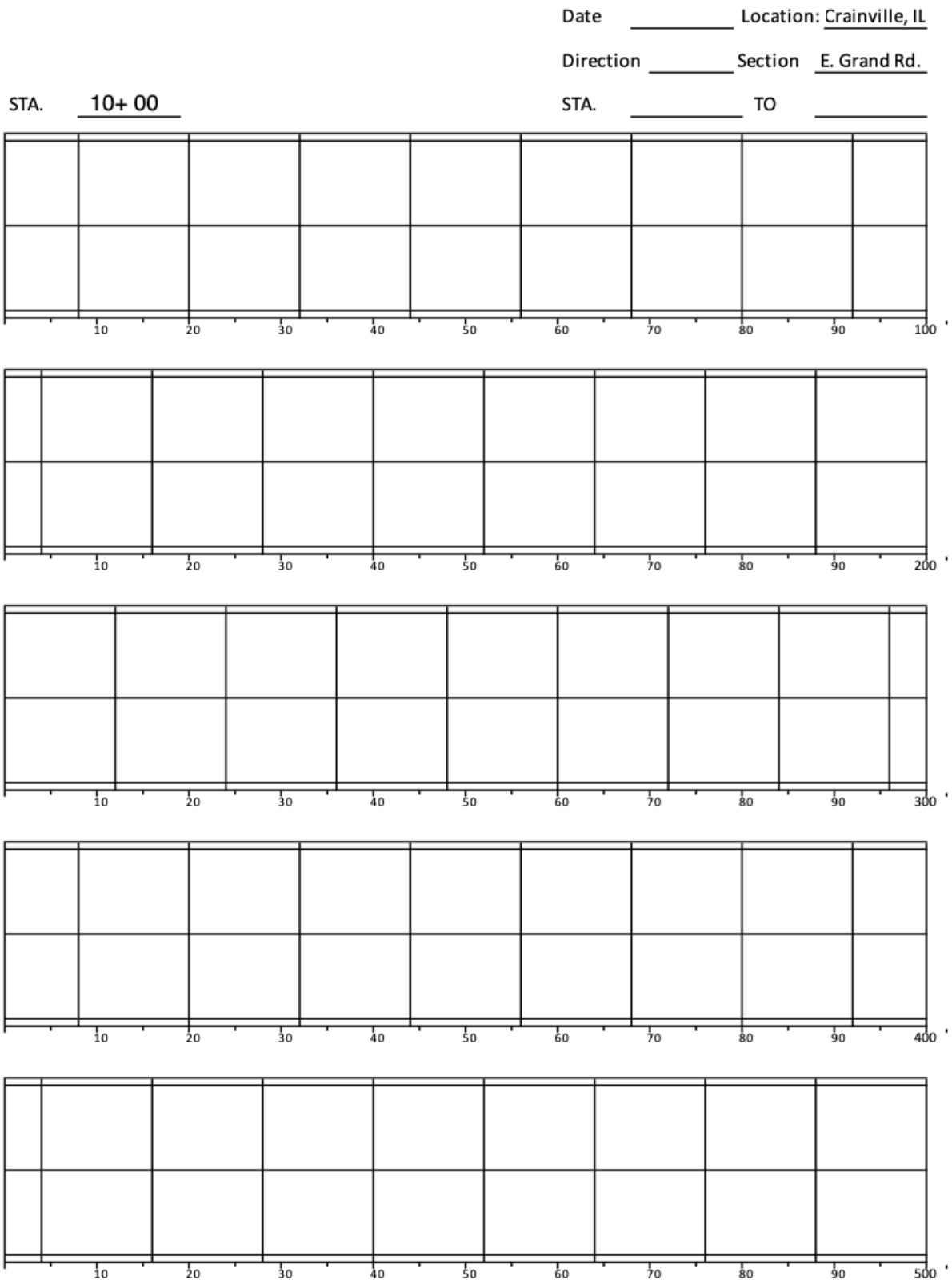

Figure 95. Illustration. Distress survey in East Grand Road at stations 10+00–15+00.

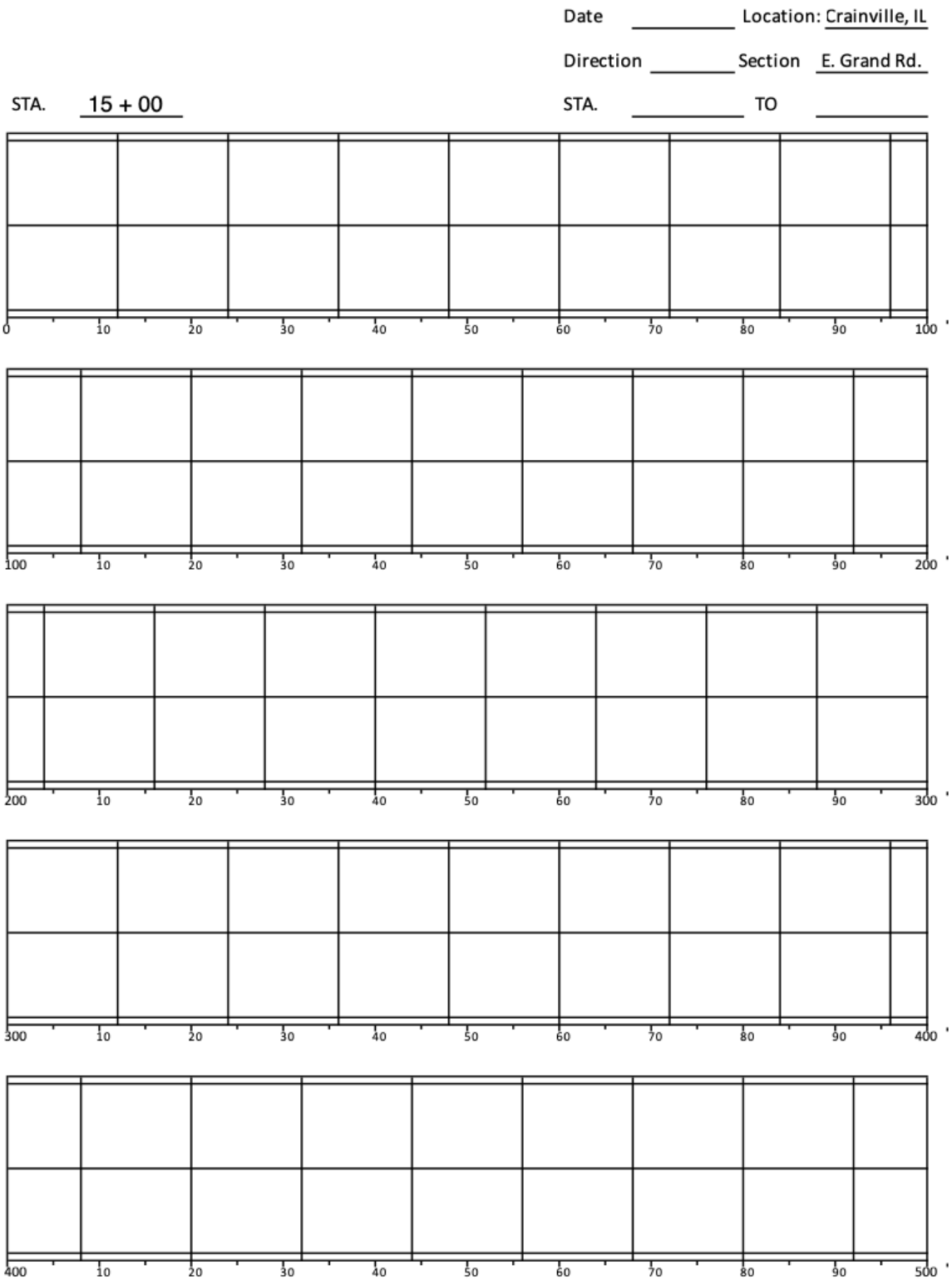

Figure 96. Illustration. Distress survey in East Grand Road at stations 15+00–20+00.

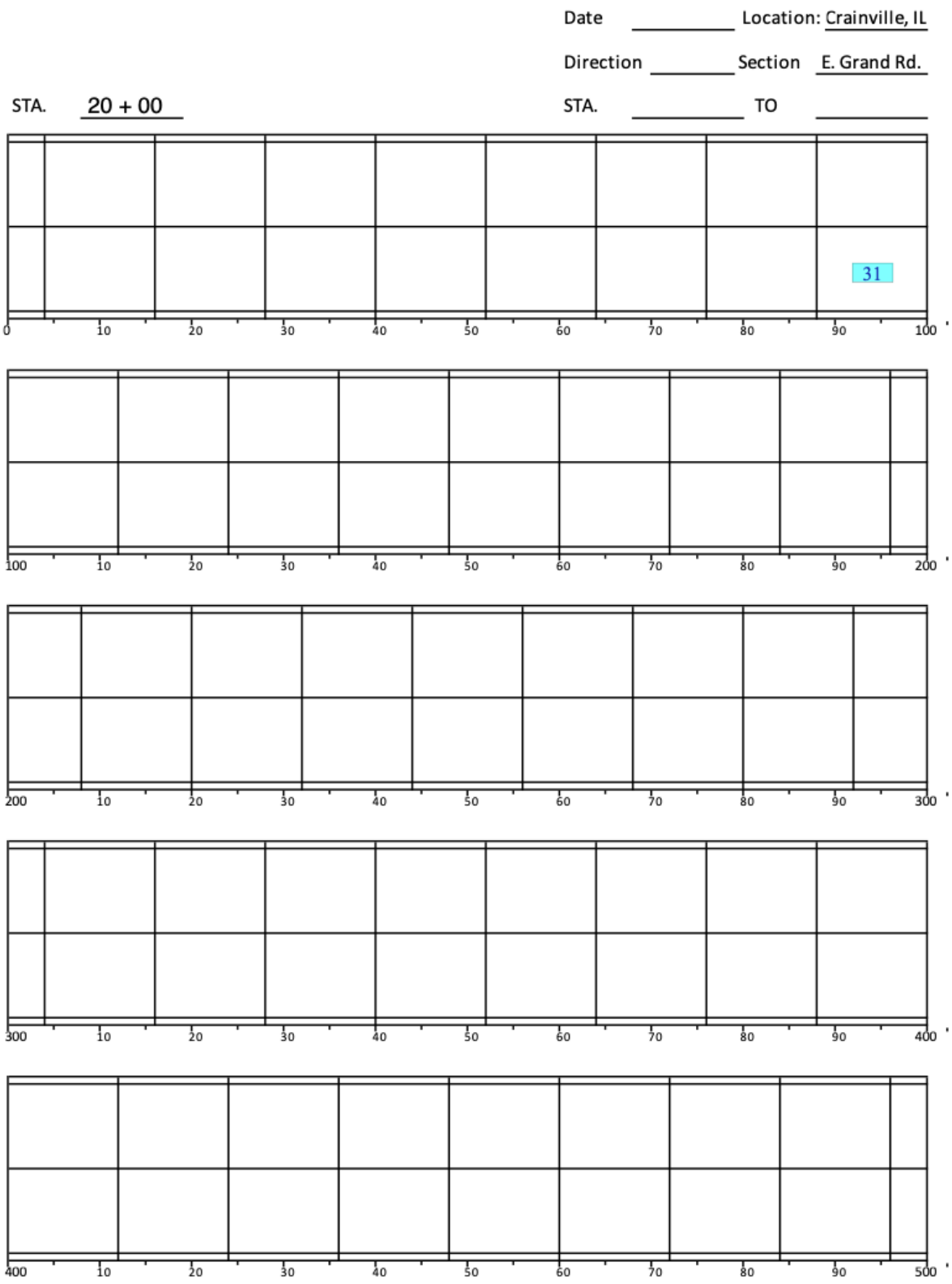

Figure 97. Illustration. Distress survey in East Grand Road at stations 20+00–25+00.

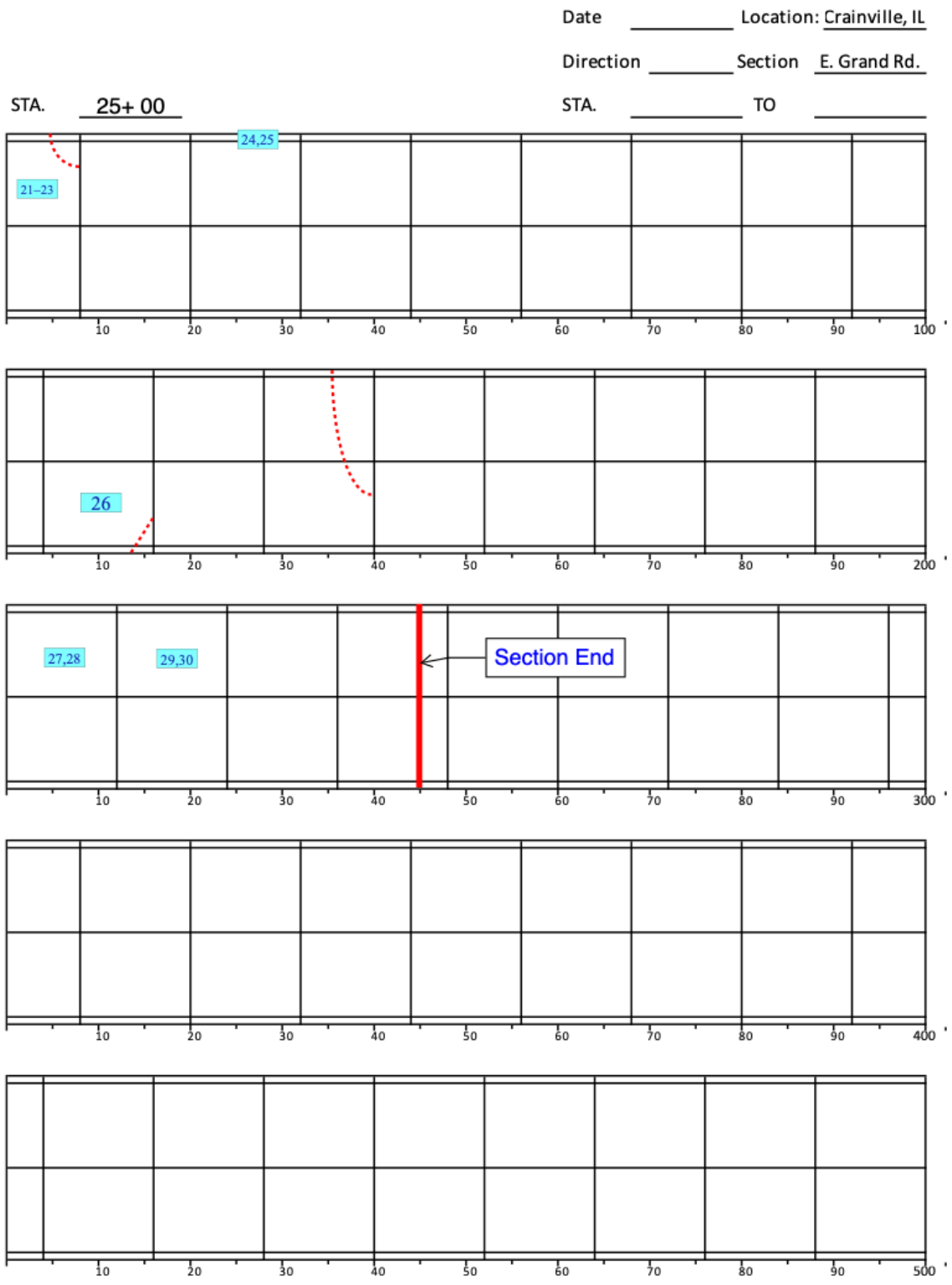

Figure 98. Illustration. Distress survey in East Grand Road at stations 25+00–30+00.

APPENDIX C: ASSESSMENT OF CORES EXTRACTED IN I-72

Table 31. Detailed Information from Cores Extracted in I-72 Eastbound Direction

Test No.	Station	Core ID	Overlay Thickness, in.	Diameter, in.	Comment	Interlayer thickness, in.
1	14+77	1.1 Center	6.49	3.70	Completely bonded to HMA. HMA looks intact	1.11
2	14+93	2-3 SH/DL	6.62	3.69	HMA completely unbonded but partially damaged.	1.00
3	15+04	1.3 TJWC	6.61	3.70	HMA completely unbonded but intact. Joint fully activated but still together. Long crack full depth	1.13
4	15+03	1.4 10"-TJWC	6.59	3.71	Completely bonded to HMA. HMA looks intact. Long crack is 32mm deep	1.05
5	15+16	1.5 TJWOC	6.64	3.70	HMA completely unbonded but intact. Joint fully activated but still together	1.25
6	82+61	2.1 SH/DL	6.17	3.67	Deteriorated HMA with only 11mm left. Complete separated and cracked	0.43
7	82+66	2.2 TJWOC	6.15	3.71	Completely bonded to HMA. HMA looks intact. Full-depth activated joint	1.55
8	144+43	3.1 SH/DL	6.11	3.64	Deterioration in the HMA. No HMA in shoulder side	0.31
9	144+55	3.2 SH/DL	6.03	3.61	Deterioration in the HMA. No HMA left on shoulder side	0.36
10	144+54	3.3 TJWOC	6.05	3.70	Completely bonded to HMA. HMA looks intact. Transverse joint crack activated full depth.	1.64
11	144+63	3.4 Center	5.97	3.70	Completed bonded to HMA. HMA looks intact. No cracks visible.	1.57
12	144+78	3.5 TJWC	6.07	3.69	Completely bonded to HMA. HMA looks intact. Long crack is only 2" deep. TJ not activated	1.43
13	144+72	3.6 TJWC	6.06	3.70	Completely bonded to HMA. HMA looks intact. Transverse joint crack activated full depth. Longitudinal Crack is ~2-3" deep	1.33
14	144+71	3.7 10in-TJWC	6.06	3.71	Completely bonded to HMA. HMA looks intact. Long crack is only ~ 1" deep	1.34

Table 32. Detailed Information from Cores Extracted in I-72 Westbound Direction

Test No.	Station	Core ID	Overlay Thickness, in.	Diameter, in.	Comment	Interlayer thickness, in.
1	150+68	2.1 SH/DL	6.19	3.69	Fabric unbonded. Fully activated joint. Split core	0.15
2	150+59	2.2 SH/DL	6.55	3.68	Fabric unbonded. Fully activated joint	0.11
3	150+82	2.3 Center	6.21	3.70	Bonded fabric	0.10
4	150+58	2.4 TJ	6.50	3.70	Full-depth activated joint. Split core. Unbonded fabric	0.13
5	109+78	3.1 Center	6.85	3.70	Fabric Bonded to overlay	0.09
6	109+66	3.2 TJ	6.85	3.71	Fully activated joint. Unbonded fabric. Split core	0.14
7	109+52	3.3 SH/DL	6.45	3.68	Fully activated joint. Unbonded fabric	0.12
8	109+43	3.4 SH/DL	7.11	3.66	Fully activated joint. Split core. Unbonded fabric	0.15

I-72 EB

Figure 99. Photo. Test No. 1: side and top views of core extracted from I-72 EB at station 14+77 at the slab center.

Figure 100. Photo. Test No. 2: side, top and bottom views of core extracted from I-72 EB at station 14+93 at the lane—shoulder joint.

Figure 101. Photo. Test No. 3: sides, top and bottom views of core extracted from I-72 EB at station 15+04 at the middle of a transverse joint with a longitudinal crack.

Figure 102. Photo. Test No. 4: side, bottom and top views of core extracted from I-72 EB at station 15+03 at 10” from a transverse joint with a longitudinal crack (on crack path).

Figure 103. Photo. Test No. 5: side, top and bottom views of core extracted from I-72 EB at station 15+16 at the middle of a transverse joint without a longitudinal crack.

Figure 104. Photo. Test No. 6: side, and bottom views of core extracted from I-72 EB at station 82+61 at the lane—shoulder joint.

Figure 105. Photo. Test No. 7: side, top and bottom views of core extracted from I-72 EB at station 82+66 at the middle of a transverse joint without a longitudinal crack.

Figure 106. Photo. Test No. 8: side, top and bottom views of core extracted from I-72 EB at station 144+43 at the lane—shoulder joint.

Figure 107. Photo. Test No. 9: sides and bottom views of core extracted from I-72 EB at station 144+55 at the lane—shoulder joint.

Figure 108. Photo. Test No. 10: side and top views of core extracted from I-72 EB at station 144+54 at the middle of a transverse joint without a longitudinal crack.

Figure 109. Photo. Test No. 11: side and top views of core extracted from I-72 EB at station 144+63 at the slab center.

Figure 110. Photo. Test No. 12: sides, and top views of core extracted from I-72 EB at station 144+78 at the middle of a transverse joint with a longitudinal crack.

Figure 111. Photo. Test No. 13: sides, and top views of core extracted from I-72 EB at station 144+72 at the middle of a transverse joint with a longitudinal crack.

Figure 112. Photo. Test No. 14: side, bottom and top views of core extracted from I-72 EB at station 144+71 at 10” from a transverse joint with a longitudinal crack (on crack path).

I-72 WB

Figure 113. Photo. Test No. 1: sides, top and bottom views of core extracted from I-72 WB at station 150+68 at the lane—shoulder joint.

Figure 114. Photo. Test No. 2: side and top views of core extracted from I-72 WB at station 150+59 at the lane—shoulder joint.

Figure 115. Photo. Test No. 3: side, top and bottom views of core extracted from I-72 WB at station 150+82 at the slab center.

Figure 116. Photo. Test No. 4: side, and top views of core extracted from I-72 WB at station 150+58 at the middle of a transverse joint.

Figure 117. Photo. Test No. 5: side, top and bottom views of core extracted from I-72 WB at station 109+78 at the slab center.

Figure 118. Photo. Test No. 6: side, and top views of core extracted from I-72 WB at station 109+66 at the middle of a transverse joint.

Figure 119. Photo. Test No. 7: side and top views of core extracted from I-72 WB at station 109+52 at the lane—shoulder joint.

Figure 120. Photo. Test No. 8: sides, top and NWGF views of core extracted from I-72 WB at station 109+43 at the lane—shoulder joint.


Illinois Department
of Transportation


ILLINOIS